

Femtosecond Laser Pulse Interaction with Tissue for Attachment of
Cells and Neurons, and Treatment of Retinoblastoma

by

Nir Katchinskiy

A thesis submitted in partial fulfillment of the requirements for the degree of

Doctor of Philosophy

in

Photonics and Plasmas

Department of Electrical and Computer Engineering
University of Alberta

Abstract

This thesis explores novel applications of femtosecond laser pulses in the medical and biomedical research area. It focuses on three main themes: 1. Treatment of Retinoblastoma using cancer targeting gold nanorods. 2. Selective attachment of cells. 3. Selective attachment of neurons. An introduction to the current understanding of femtosecond laser pulse interactions with nanoparticles is provided, where, the reasoning for using cancer targeting gold nanorods for cancer treatment applications is detailed, as well as, the reasons for using femtosecond laser pulses. Additionally, an introduction to the current understanding of femtosecond laser pulse interaction with biological matter is provided. The non-linear multiphoton absorption and cascade ionization processes are discussed, as well as ionized electron densities, shockwave and cavitation bubble formation.

The application of retinoblastoma targeting gold nanorods with femtosecond laser pulses towards treatment of retinoblastoma is presented. Retinoblastoma is a cancerous disease that affects the retina, and primarily affects young children. To date, the primary treatment goal of retinoblastoma is to save the child's life, while the preservation of the eye and its functionality are the secondary goals. Reoccurrence of tumors is mainly attributed to the persistence of cancer stem cells. EpCAM+ Y79 retinoblastoma cells behave like cancer stem cells and are recognized as cells that are resistant to treatment. Here, an effective technique to treat retinoblastoma cancer cells is presented, using femtosecond laser pulses and epithelial cell adhesion molecule (EpCAM) targeting gold nanorods (Au-NRs). Complete assessment of the optimal laser parameters required for the development of a translational retinoblastoma cancer treatment is

provided. Both an MTS cellular metabolism assay and a fluorescence viability assay demonstrate cellular viability drop, to $\approx 10\%$. Right after laser irradiation the cellular membrane ruptures. Calculations and field emission scanning electron microscopy (FESEM) imaging show that Au-NRs reach melting temperature after laser pulse exposure. This treatment methodology could be developed to treat chemotherapy resistant and radiation resistant cancers.

The application of laser-induced cell-cell surgical attachment using femtosecond laser pulses is also reported. Attachment of single cells using sub-10 femtosecond laser pulses, with 800nm central wavelength delivered from a Ti:Sapphire laser, is demonstrated. To check that the cells did not go through a cell-fusion process, a fluorescent dye Calcein AM was used to verify that the fluorescent dye did not migrate from a dyed cell to a non-dyed cell. The mechanical integrity of the attached joint was assessed using an optical tweezer. The attachment of cells was performed without the induction of cell-cell fusion, with attachment efficiency of 95%. Cell-cell attachment was achieved by delivery of one to two trains of femtosecond laser pulses lasting 15 ms each. Then, an insight into the mechanism of femtosecond laser nanosurgical attachment of cells is provided. It is demonstrated that during the attachment of two retinoblastoma cells the phospholipid molecules of both cells hemifuse and form one shared phospholipid bilayer, at the attachment location. In order to verify the hypothesis that hemifusion takes place, transmission electron microscope images of the cell membranes of retinoblastoma cells were taken. It is shown that at the attachment interface, the two cell membranes coalesce and form one single membrane shared by both cells. Thus, further evidence is provided to support the hypothesis that laser-induced ionization process led to an ultrafast reversible destabilization of the phospholipid layer of the cellular membrane, which resulted in crosslinking of the phospholipid molecules in each membrane. This process of hemifusion occurs throughout the entire penetration depth of the

femtosecond laser pulse train. Thus, the attachment between the cells takes place across a large surface area, which affirms our findings of strong physical attachment between the cells. The femtosecond laser pulse hemifusion technique can potentially provide a platform for precise molecular manipulation of cellular membranes.

Finally, the application of attachment of neurons using femtosecond laser pulses is presented. Neuronal axons are connected to neuronal soma. Neuronal injury may cause an irreversible damage to cellular, organ and organism function. While preventing neural injury is ideal, it is not always possible. There are multiple etiologies for neuronal injury including trauma, infection, inflammation, immune mediated disorders, toxins and hereditary conditions.

Preface

This thesis is an original work by Nir Katchinskiy, who conducted the research under the supervision of Professor A. Y. Elezzabi at the University of Alberta. This work is multidisciplinary in its nature and combines topics from engineering, physics, biology and oncology; therefore, a collaborative work with Professor. Roseline Godbout from the department of oncology was established.

Portions of chapter 3 have been published in: N. Katchinskiy, R. Godbout, A. Hatef, A. Y. Elezzabi, Anti-EpCAM Gold Nanorods and Femtosecond Laser Pulses for Targeted Lysis of Retinoblastoma. *Advanced Therapeutics*, 1(1): 1-10, 2018. N. Katchinskiy was responsible for the manuscript preparation, cell sample preparation, carrying out experiments, post experiment cell processing, cell imaging, and cell viability analysis. Prof. A. Hatef performed nanorods heating and electric field calculation. Prof. A.Y. Elezzabi supervised the project and contributed to the manuscript preparation. Prof. R. Godbout assisted with providing cells, and manuscript preparation.

Portions of chapter 4 have been published in: N. Katchinskiy, R. Godbout, H. R. Goetz, A. Y. Elezzabi. Femtosecond laser-induced cell-cell surgical attachment. *Lasers Surg Med* 2014 April 01;46(4):335-341. And N. Katchinskiy, R. Godbout, A. Y. Elezzabi Characterization of femtosecond-laser pulse induced cell membrane nanosurgical attachment. *Biomed Opt Express* 2016 June 22;7(7):2749-2758. N. Katchinskiy was responsible for the manuscript preparation, cell sample preparation, carrying out experiments, post experiment cell processing, cell imaging, and cell viability analysis. Prof. A.Y. Elezzabi supervised the project and contributed to the

manuscript preparation. Prof. R. Godbout assisted with providing cells, and manuscript preparation. Dr. H. R. Goetz assisted with manuscript preparation.

Portions of chapter 5 have been published in: N. Katchinskiy, H. R. Goetz, R. I. Dutta, Godbout, A. Y. Elezzabi, Novel method for neuronal nanosurgical connection. Sci. Rep. 2016 February 05;6:20529. N. Katchinskiy was responsible for the manuscript preparation, cell sample preparation, carrying out experiments, post experiment cell processing, cell imaging, and cell viability analysis. Prof. A.Y. Elezzabi supervised the project and contributed to the manuscript preparation. Prof. R. Godbout assisted with providing cells, and manuscript preparation. Dr. H. R. Goetz assisted with manuscript preparation. I. Dutta was responsible for providing Neuro2A cells.

The goal of work was to develop new tools to advance the current technology to attach nerves and to develop additional tools to treat various kinds of cancers, using femtosecond laser pulse technology. By combining concepts from engineering, physics, and biology, this thesis demonstrates the application of engineering tools to a wide range of scientific disciplines. Engineering tools, such as lasers, microscopes, and nanoparticles, are used to assist us in solving scientific problems with real world applications. In this thesis, in particular, engineering principles and tools, such as femtosecond laser pulses, various optical elements, and gold nanoparticles are used to advance the understanding of laser-matter interaction and its application to solve important biomedical problems.

At first, the direct interaction between femtosecond laser pulses with cells towards performing cell-cell attachment was investigated, and the optimum conditions for performing laser-induced cell attachment were methodically discovered. Then, a hypothesis regarding the physiological

changes in the cell membrane structure was developed by understanding both the physics of non-linear laser-matter interaction, and cell biology. The second step was to provide direct evidence that the hypothesis of hemifusion does indeed take place during laser-induced attachment. As a result, a technique to attach individual cells, and track them during the process of preparation for transmission electron microscopy (TEM) imaging was developed. Successfully executing this protocol enabled the imaging of the attached membranes and provided further support that the attachment process results in hemifusion of the cell membranes. The final step of this goal was the implementation of laser-induced cell attachment technique on neuronal cells, in order to demonstrate a proof of concept that such tool could be used in the future by scientists to further study neuronal function and communication, Wallerian degeneration, and neuronal interaction. The goal to attach neurons was achieved successfully on multiple types of neuronal cells.

The second objective of this thesis was to develop a technique to selectively target and treat retinoblastoma cancer using gold nanoparticles and femtosecond laser pulses. At first, the optimal size and dimensions of nanoparticles was designed by understanding both the physics behind laser – nanoparticle interaction, and the requirements for attachment or uptake to/by a cellular organism. Then, the ability to selectively target retinoblastoma cells was assessed using 2-photon microscopy tools, by comparing the uptake of the gold nanoparticles by retinoblastoma cells to fetal retinal cells. Finally, the optimal parameters for effective treatment were developed and assessed using fluorescence viability assay and MTS cell metabolism assay. Control groups were selected carefully to ensure that the treatment is due to the combination of cancer-targeting nanoparticles with femtosecond laser pulses, and not due to the laser alone or the nanoparticles alone.

To develop the laser-induced cell/neuron attachment technique and cancer treatment proof of concept, a microscope system was coupled to femtosecond laser pulses, and designed to accurately target the laser pulses onto the cells studies. The choice to use femtosecond laser pulses over other laser sources required an understanding of the laser-tissue / laser-nanoparticle interaction physics, including non-linear multiphoton absorption, cascade/impact ionization, an estimation of the electron density, and the focal temperature rise. Additionally, it was crucial to understand the destructive effects of cavitation bubble formation.

To my family and my wife, for their love and support

“The more you know, the more you know you don't know”

Aristotle

Acknowledgements

Special thanks to my supervisor, Prof. A. Y. Elezzabi, for tireless hours of work and support throughout six years of my life. The countless hours that Abdul has spent solving problems, editing and reviewing my papers have tremendously helped shaping me as a person and a scientist, and constructing the contents of this thesis. It has been my pleasure to work under your supervision, and I feel fortunate to have such a wonderful supervisor.

I have benefited greatly from excellent collaborations. I would like to express my sincere thanks to Prof. R. Godbout and her lab members for opening their lab facilities for me, and introducing me to cell biology work and analysis. Whenever I had a question or a problem, your door has been always open.

I would like to thank my committee members for their suggestions. Special thanks to Prof. Frank Wuest for opening his facilities to my research.

I would like to thank Dr. Christian Foerester for his assistance with nanoparticle preparation, Prof. Ali Hatef for assisting with nanoparticle simulations, and Dr. Xuejun Sun for assisting with cell imaging.

I would like to thank my lab colleagues, Shawn Grieg, Curtis Firby and Brett Carnio for their support, and friendship. Our fun coffee breaks, chats in the lab, and outside lunches during the summer, made the years enjoyable and fun.

I would like to say thank you to my family and friends. Without your love and support I would not be where I am today. There are not enough words to express my gratitude. You stood by me throughout this difficult and challenging endeavor. I would also like to say special thank

you to my dear friend David Sykes, for being there for me when I needed someone to talk to. Thanks for the daily conversations about life, science, business and philosophy.

Thank you to my dogs Coco and Tzippi for being such an amazing four-legged companions.

I am also so appreciative to my parents, Alex and Silviya, and my brothers Michael and Maor. Without your encouragement, companionship and love, this thesis would have not been possible. I am blessed to have such a wonderful family in my life.

Finally, I thank my beautiful, fun-loving and amazing wife, Carly. I am an incredibly fortunate person to share my life with such a fun, caring and loving person. Thanks for packing my lunches every day, and for tolerating all of my complaints.

Table of Contents

Abstract	ii
Preface.....	v
Acknowledgements.....	xi
List of Tables	xvi
List of Figures.....	xvi
List of Abbreviations	xxiv
List of Symbols.....	xxvi
Chapter 1	1
Motivation and Thesis Objectives	1
1.1 Motivation.....	2
1.2 Thesis Objectives	2
1.3 Thesis Organization.....	3
Chapter 2.....	5
Photothermal Therapy Using Gold Nanoparticles and Laser-Tissue Interaction	5
2.1 Laser-Nanoparticle Interaction - Background and Chapter Objectives	6
2.1.1 NP Surface Plasmon Generation	8
2.1.2 Effective Wavelength	13
2.1.3 E-field Enhancement	19
2.1.5 Pulsed laser – NP heat transfer for NP Immersed in Water	26
2.1.6 Bubble Formation.....	33
2.1.7 Surface Chemistry of Nanoparticles.....	35
2.1.8 Femtosecond Laser Pulses and Gold Nanorods for Cancer Treatment	36
2.2 Laser-Tissue Interaction - Background and Chapter Objectives	43
2.2.1 Multiphoton Ionization.....	47
2.2.2 Laser Pulse Ablation Profile.....	49
2.2.3 Laser Pulse Induced Heat Stress.....	51
2.2.4 Shockwave and Cavitation Bubble Formation.....	53
2.2.5 Different Femtosecond Laser Pulse Repetition Rates Effects on Laser Pulse Ablation	55
2.2.6 Critical Power for Self-Focusing and Plasma Formation.....	56

2.2.7 Cellular Membrane.....	58
2.2.8 Cellular Fusion and Hemifusion	60
Chapter 3.....	67
Treatment of Retinoblastoma.....	67
3.1 Introduction.....	68
3.2 Experimental Materials and Methodology.....	72
3.2.1 Cell Culture.....	72
3.2.2 Nanorods and Cancer Cell Targeting	73
3.2.3 Femtosecond Laser Pulse Delivery System.....	74
3.2.4 Viability Assay	76
3.2.5 Statistical Analysis	77
3.3 Results.....	78
3.3.1 Targeting.....	78
3.3.2 Femtosecond Laser Pulse Treatment of Retinoblastoma	81
3.4 Discussion and Conclusion	90
Chapter 4.....	94
Femtosecond Laser-Induced Cell-Cell Surgical Attachment.....	94
4.1 Introduction.....	95
4.2 Experimental Methodology.....	98
4.2.1 Cell Suspension	98
4.2.2 Setup Characteristics	99
4.2.3 Experimental Procedure	100
4.2.4 TEM Preparation	101
4.3 Results.....	102
4.4 Discussion	106
4.4.1 Cell-Cell Attachment Model	107
4.4.2 Cell-Cell Attachment Efficiency	111
4.5 Conclusion.....	111
4.6 Characterization of Hemifusion	112
4.6.1 Characterization Results.....	112
4.6.2 Characterization Discussion	120

4.6.3 Characterization Conclusion.....	121
Chapter 5.....	123
Novel Method for Neuronal Nanosurgical Connection.....	123
5.1 Introduction.....	124
5.2 Experimental Methodology.....	128
5.2.1 Cell Cultures.....	128
5.2.2 Experimental Procedure.....	128
5.3 Results.....	129
5.4 Conclusion.....	134
Chapter 6.....	135
Conclusion and Future Prospects.....	135
6.1 Conclusion.....	136
6.2 Future Prospects.....	138
Results.....	142
References.....	143
Appendix A.....	156
A.1 Calculation of Electric Field Enhancement Around Au-NR.....	157
A.2 Calculation of Temperature around Au-NR.....	158
Appendix B.....	161
B.1 Pulse Width Estimation Due to Dispersion.....	162
Appendix C.....	163

List of Tables

Table A.1: Material electromagnetic parameters.....	158
Table A.2: Material thermal and physical parameters.....	160

List of Figures

Figure 2.1: A. Various sizes of gold nanospheres. B. Gold nanorods. C. Gold nano-cages (Image taken from http://bit.bme.jhu.edu/Nanoparticles.html).....	7
Figure 2.2: Schematic of the localized surface plasmon resonance on gold nanorod. Upon illumination at resonant wavelengths, conduction band electrons on the gold nanoparticle surface are delocalized and undergo collective oscillation.....	9
Figure 2.3: Surface polarization of metallic rod having a length L and radius R , due to incoming EM wave with electric field E parallel to the nanorod's axis. k is the wave-number of the EM wave[9].....	14
Figure 2.4: Effective wavelength of gold nanorods vs/ incident light wavelength, for varying rod radius 5nm, 10nm, and 20nm [9].....	15
Figure 2.5: Surface charge polarization of gold nanorod ($L=200\text{nm}$, $R=40\text{nm}$) due to EM wave with different frequencies [22].....	16
Figure 2.6: Orientation of Nanorod with length L and radius R , interacting with EM wave with electric field E parallel to the nanorods axis. K represents the wave number of the EM wave.....	17
Figure 2.7: Effect of increasing nano ellipsoid length L on extinction cross-section [8]. Increased length L results in red-shift of extinction resonance, while reducing the extinction strength.....	18
Figure 2.8: The linear relationship between a single gold nanorod and nano-ellipsoid resonance wavelength vs. nanoparticle's length L [8]. Inset figure depicts relationship between single gold nanorod and nano-ellipsoid resonance wavelength divided by its length vs. the nanoparticle's length L	18

Figure 2.9: Gold nanorod resonance wavelength vs. rod radius [23]. Curves calculated for nanorods with varying lengths L_{rod} between 0nm and 600nm. Initial blue-shift in resonant wavelength, followed by red-shift with increasing radius.....20

Figure 2.10: Gold nanorod resonance wavelength vs. gold nanorod aspect ratio (L/R) [23]. Curves calculated for nanorods with varying nanorod radius R between 5nm and 100nm. Linear relationship between aspect ratio and resonance wavelength is shown.....20

Figure 2.11: Calculated electric field enhancement factors, η , of spherical metal nanoparticles of 11 metals immersed in a) air, b) water [24].....23

Figure 2.12: Normalized electric field distribution of gold nanorod antenna suspended in air with $L = 100$ nm, $R = 20$ nm at $\lambda = 600$ nm incidence. The incident plane wave is in z direction and the electric field is polarized in x direction [8]. On right is a 2D map of electric field (V/m) enhancement (E_{out}/E_{in}). [8].....24

Figure 2.13: Normalized electric field distribution of gold nano-ellipsoid antenna suspended in air with $L = 100$ nm at $\lambda = 600$ nm incidence. The incident plane wave is in z direction and the electric field is polarized in x direction [8]. On right is a 2D map of electric field (V/m) enhancement (E_{out}/E_{in}).....24

Figure 2.14: Electric field enhancement vs. incident wavelength. Calculations carried out for varying lengths L of nanorod / nanoellipsoid length, between 100nm-240nm [8]. Increase in length of gold nanoparticle leads to red-shift in resonance wavelength and increased E-field enhancement.....25

Figure 2.15: (a). Time evolution of temperature profiles of $48 \text{ nm} \times 14 \text{ nm}$ AuNR and its surrounding water at the surface following irradiation with a laser pulse of fluence, $F_{pulse} = 4.70 \text{ J m}^{-2}$. **(b)** Temperature profiles at different times after laser exposure as a function of radial distance at the mid-length of the nanorod [30].....27

Figure 2.16: Temperature distribution in water surrounding the $48 \times 14 \text{ nm}^2$ gold nanorod taken at 70 ps after irradiation by a 250 fs laser pulse with an average fluence of 4.70 Jm^{-2} [30]. Color map is temperature in Kelvin.....28

Figure 2.17: Time evolution of temperature profiles of $48 \times 14 \text{ nm}^2$ gold nanorod and its surrounding water at the surface during a $1\mu\text{s}$ time duration of multiple laser exposures at a repetition rate of 80MHz with $F_{pulse} = 4.70 \text{ Jm}^{-2}$ [30].....29

Figure 2.18: Estimated nanoparticle gold lattice temperature [K] as a function of the laser fluence [J cm^{-2}] [31]. Increased fluence leads to increased temperature. Melting and boiling temperatures are noted.....30

Figure 2.19: The near-field enhancement for A. transverse, B. diagonal, and C. longitudinal polarizations. The color legend on the right shows the magnitude of the field enhancement.....40

Figure 2.20: Time-dependent temperature evolution of electrons, T_e , lattice T_l and water T_w , at the $11\text{nm} \times 43\text{nm}$ AuNR-water interface, for a longitudinal incident 55 fs, $\lambda=800 \text{ nm}$ laser pulse of at a fluence of 40 mJ/cm^242

Figure 2.21: Schematic diagram of single photon absorption vs. multiphoton absorption. An electron is excited from its ground state to an excited state with either four 1.55eV photons (multiphoton absorption) or a single 6.2eV photon (single photon absorption).....46

Figure 2.22: Schematic diagram of photo-ionization and impact ionization [7]. Photo-ionization of ‘lucky’ electron leads to inverse bremsstrahlung absorption of incoming photons, which leads to impact and avalanche ionization.....48

Figure 2.23: Illustration of cell membrane. A cutaway side view of the human cell membrane. Transmembrane proteins, phospholipid molecule, hydrophilic head and hydrophobic tail are marked. Figure taken from Alfred Pasiaka/Science Photo Library.....60

Figure 2.24: Illustration of various mechanisms of cellular fusion [84].....62

Figure 2.25: Illustration of the mechanism of viral cellular fusion [84].....63

Figure 2.26: Illustration of the process of fusion-through-hemifusion [101].....65

Figure 3.1: Illustration of retina and its cell layers (figure taken from <https://www.allaboutvision.com/resources/retina.htm>).....69

Figure 3.2: Experimental setup. Ti:Sapphire femtosecond laser pulse amplifier emitting 35 femtosecond laser pulses with a center wavelength of 800nm and a pulse repetition rate of 1KHz. The pulses pass through a high speed shutter and are delivered to a 4× objective lens. The procedure was visualized with a CMOS camera.....75

Figure 3.3: A-B. 2-photon microscope images of Y79 retinoblastoma cell incubated with PEGylated anti-EpCAM Au-NRs. **C.** 3D confocal image of two Y79 retinoblastoma cells incubated with PEGylated anti-EpCAM Au-NRs.....79

Figure 3.4: A. 3D 2-photon image of FRCs incubated with anti-EPCAM Au-NRs. **B-C.** 2-photon microscope image of fetal retinal cells, incubated with anti-EPCAM Au-NRs.....79

Figure 3.5: TEM imaging of targeting of breast cancer cells (EMT-6) using anti-EpCAM Au-NRs. **A:** Uptaken particles inside the cells. **B:** Accumulation of particles on the cell surface....80

Figure 3.6: TEM imaging of targeting of human colon carcinoma (HCA-7) using anti-EpCAM Au-NRs. **A:** Accumulation particles on the cell surface. **B:** Uptaken particles inside the cells....80

Figure 3.7: A. Bright field image right before femtosecond laser pulse irradiation of retinoblastoma cells, not containing Au-NRs. **B.** Bright field image during femtosecond laser irradiation of cells **C.** Bright field image right after femtosecond laser irradiation of retinoblastoma cells. The area of laser irradiation is marked with the dotted circle. Laser scanning direction is marked with arrow. Laser beam diameter of 400µm spot size. At the focal spot, the laser pulse train average power, energy, and intensity were: 50 mW, 50 µJ/pulse, and 1.45 TW/cm², respectively.....82

Figure 3.8: A. Bright field image right before femtosecond laser pulse irradiation of retinoblastoma cells, containing Au-NRs. **B.** Bright field image during femtosecond laser irradiation of retinoblastoma cells **C.** Bright field image right after femtosecond laser irradiation of retinoblastoma cells. The area of laser irradiation is marked with the dotted circle. Laser scanning direction is marked with arrow. Laser beam diameter of 400µm spot size. At the focal spot, the laser pulse train average power, energy, and intensity were: 50 mW, 50 µJ/pulse, and 1.45 TW/cm², respectively.....83

Figure 3.9: A-E. Time lapse of 2-photon imaging of fs laser pulse irradiation of retinoblastoma cells that contain Au-NRs. At the focal spot, the laser pulse train average power, energy, and intensity were: 50 mW, 50 $\mu\text{J/pulse}$, and 1.45 TW/cm^2 , respectively.....85

Figure 3.10: FESEM image of Au-NRs before laser irradiation.....86

Figure 3.11: FESEM image of Au-NRs after laser irradiation. At the focal spot, the laser pulse train average power, energy, and intensity were: 50 mW, 50 $\mu\text{J/pulse}$, and 1.45 TW/cm^2 , respectively.....86

Figure 3.12: Fluorescence microscopy images. **A.** Retinoblastoma cells that do not contain Au-NRs exposed to laser pulses. The cells that appear green contain Calcein AM which indicate that the cells are viable. **B.** Retinoblastoma cells that contain Au-NRs and exposed to fs laser pulses. Most of the cells appear red in this case, which indicate that these cells are dead and contain propidium iodide (PI). Laser beam diameter of $400\mu\text{m}$ spot size. At the focal spot, the laser pulse train average power, energy, and intensity were: 50 mW, 50 $\mu\text{J/pulse}$, and 1.45 TW/cm^2 , respectively.....88

Figure 3.13: MTS metabolism assay of retinoblastoma cells. No significant difference between laser pulse, Au-NRs only, and control were found based on two tailed student t-test. Significant difference ($p < 0.01$) was found between Au-NRs + Fs laser and control group, based on two tailed student t-test ($n=4$). Error bars represent standard deviation of the normalized values within the group.....89

Figure 3.14: Cellular counting of fluorescence viability assay of retinoblastoma cells. No significant difference between laser pulse, Au-NRs only, and control were found based on two tailed student t-test. Significant difference ($p < 0.05$) was found between Au-NRs + Fs laser and control group, based on two tailed student t-test ($n=4$). Error bars represent standard deviation of the normalized values within the group.....90

Figure 3.15: FESEM samples of melted Au-NRs due to fs laser pulse irradiation. When the Au-NRs were irradiated with **A.** 5 pulses **B.** 10 pulses **C.** 15 pulses and **D.** 25 pulses. Laser beam diameter of $400\mu\text{m}$ spot size. At the focal spot, the laser pulse train average power, energy, and intensity were: 50 mW, 50 $\mu\text{J/pulse}$, and 1.45 TW/cm^2 , respectively.....91

Figure 3.16: Temperature distribution calculations on Au-NR with a size of 11nm×43nm, irradiated with fs laser pulse of $\lambda_{\text{center}}=800\text{nm}$ and $1.45\text{TW}/\text{cm}^2$ for three incident fs laser pulse polarizations. **A.** Longitudinal polarization. **B.** Diagonal polarization. **C.** Transverse polarization. The arrow points at the direction of the polarization of the incident electric field E_092

Figure 4.1: **A.** A fluorescent cell (i) and a non-fluorescent cell (ii) are identified. The fluorescent cell is identified through its fluorescence due to multi-photon absorption of the laser pulse as shown by the bright green light emission spot. **B.** Cells are brought into contact using an optical tweezer, and femtosecond laser pulse is delivered to the contact location. The dark spot at the boundary between the two cells is due to the formation of a cavitation bubble. **C.** cells (i and ii) observed post-attachment. **D.** Fluorescence imaging of the two cells. Only cell (i) is fluorescing. **E.** Verification of cell membrane physical attachment where the cells are oriented $\sim 45^\circ$ relative to original orientation.....103

Figure 4.2: **A.** A fluorescent cell (i) is identified. **B.** The fluorescent and two non-fluorescent cells (ii and iii) are identified under bright field view. **C.** Femtosecond laser pulse is delivered to the contact location. The dark spot at the boundary between the two cells is due to the formation of a cavitation bubble. **D.** Under fluorescence imaging, it is identified that the cytoplasm of the dyed cell did not transfer to the attached cell. **E.** under bright field imaging, cells are identified as physically attached. The cells are intact, and in close proximity to each other. **F.** Physical attachment was verified: the cells were pulled in a circular path. The cells are captured while being oriented at 180° relative to their original position.....104

Figure 4.3: **A.** A fluorescent cell (i) is identified. **B.** Fluorescent cell (i) is pre-attached to a non-fluorescent cell (ii). Two non-fluorescent cells (iii and iv) are located below cell (i). **C.** Fluorescent cell (i) is attached to the non-fluorescent cell (iii). The bright spot at the boundary between the two cells is the reflected light emitted from the femtosecond laser pulse. **D.** The non-fluorescent cell (iii) is attached to the non-fluorescent cell (iv). **E.** The non-fluorescent cell (ii) is attached to the non-fluorescent cell (v). **F.** Under bright field imaging, cells are identified as physically attached. The cells are intact, and in close proximity to each other. **G.** Under fluorescence imaging, it is identified that the cytoplasm of the dyed cell did not transfer to the

attached cell. **H.** Physical attachment was verified: the cells were pulled in a circular path. The cells are captured while being rotated relative to their original position.....106

Figure 4.4: **A.** A femtosecond laser pulse is delivered to the target point between the cell membranes. **B.** The high laser pulse intensity at the focal point causes a reversible breakdown or a precise ablation of the outer phospholipid layer. **C.** Energetic ions and electrons cross the center nonpolar region and break additional bonds between the fatty acid tails. **D.** The relaxation process results in the formation of new stable bonds and formation of singular cell membrane only at the connection point.....110

Figure 4.5: TEM images of cellular membranes of a group of retinoblastoma cells that were left to naturally attach, in order of increasing magnification from **A-D.** A small gap of 10 to 20 nm separates between the two phospholipid cell membranes throughout the entire attachment region.....113

Figure 4.6: Bright field microscope image of four retinoblastoma cells after performing the laser-induced hemifusion procedure on cell (i) and cell (ii). Cell (ii) is allowed to attach naturally to cell (iii). The out of focus cell (iv) is located underneath the rest of cells and is not attached to any of the cells.....114

Figure 4.7: **A.** TEM z-slice of the three cells depicted in figure 3. Here, the middle cell (ii) is naturally attached to one cell (iii) and laser hemifused to the other cell (i). **B, C.** The region of naturally attached cells is depicted. The individual membranes are clearly identifiable, with a gap of 10-20 nm between the membranes. The green dashed line indicates the location of the naturally attached membranes. **D,E,F.** The region of femtosecond laser pulse induced hemifusion is shown, where the individual cell membranes cannot be distinguished. The yellow dashed line indicates the location of membrane hemifusion.....117

Figure 4.8: **A.** TEM z-slice of three retinoblastoma cells under low magnification. Here, the middle cell is naturally attached to one cell (left) and laser hemifused to the other cell (right). **B,C,D.** In order of increasing magnification from B-D, the laser-hemifused membranes are depicted. The two membranes merge to form a single phospholipid layer shared by both cells.119

Figure 5.1: Illustration of neuron and its structures (soma, dendrite, and axon). Image is taken from <https://www.medicalnewstoday.com/articles/320289.php>.....124

Figure 5.2: **A.** An illustration of how a femtosecond laser pulse is delivered to the target point between an axon and a neuronal soma. **B.** An illustration of the phospholipid bilayers of the neuron soma and axon. Note that the attachment region, where the phospholipid layers are attaching, is designated with a circular spot. This does not represent the laser focal spot. **C.** The laser pulse high intensity causes a reversible destabilization of both phospholipid layers. A depiction of the femtosecond laser pulse induced axon-soma attachment. Here, the generated free ions (shown in red) and free electrons (shown in orange) cross the center nonpolar region and break bonds between the fatty acid hydrophobic tails. **D.** The relaxation process results in the formation of new stable bonds and formation.....131

Figure 5.3: The arrows point to the location of neuron connection using femtosecond laser pulses. **A.** A single Neuro2A's (i) axon is connected to the soma of Neuro2A (ii). **B.** Two axons of Neuron2A (i) are connected using to the soma of Neuro2A cells (ii) and (iii). **C.** Overlap image of the original Neuro2A cells (i), (ii), and (iii) compared to Neuro2A cells (i), (ii*), and (iii*) after being rotated and moved by an optical tweezers to examine the integrity of the axons' connectivity. **D.** Two groups of four P19 neurons are identified. **E.** The axon of P19 (i) is brought into contact with the soma of P19 (ii), and are connected as shown by the arrow tip. Note that there is another unconnected axon nearby which was left detached **F.** The two groups of P19 cells are rotated and moved by optical tweezers to examine the integrity of the axons' connectivity.....133

List of Abbreviations

AuNR	Gold nanorod
CNS	Central nervous system
CTAB	Hexadecyl-trimethyl-ammonium bromide
CW	Continuous wave
DMEM	Dulbecco's modified Eagle medium
DPBS	Dulbecco's phosphate-buffered saline
EBR	External beam radiotherapy
EGFR	Epidermal growth factor receptor
EM	Electro Magnetic
EpCAM	Epithelial cell adhesion molecule
FESEM	Field-emission scanning electron microscopy
FRC	Fetal retinal cells
FWHM	Full Width Half Max
HCS	High-content screening
LSPR	Localized Surface Plasmon Resonance
MNP	Metallic nanoparticle
MTS	3-(4,5-dimethylthiazol-2-yl)-5-(3-carboxymethoxyphenyl)-2-(4-sulfophenyl)-2H-tetrazolium)
NA	Numerical aperture
NC	Nanocage
NIR	Near Infrared Radiation
NR	Nanorod
NS	Nanosphere
NSH	Nanoshell

PEG	Polyethylene glycol
PI	Propidium iodide
PNS	Peripheral nervous system
PPTT	Plasmonic photothermal therapy
RF	Radio Frequency
SEM	Scanning electron microscopy
SH	Sulfhydryl
SPR	Surface Plasmon Resonance
TEM	Transmission electron microscopy
YAG	Yttrium aluminum garnet

List of Symbols

Δ	Ionization potential
μm	Micrometer
A_{abs}	Absorption cross-sectional area
A_{surface}	Surface area of nanoparticle
Au	Gold
C	Celsius
C_{abs}	Absorption cross-section for gold nanorod
C_e	Electron thermal capacity
C_l	Lattice thermal capacity
cm	Centimeter
E	Electric Field
e	Electron charge
E_{abs}	Absorbed laser energy
eV	Electron volt
F_{pulse}	Laser pulse fluence
fs	Femtosecond
G	Thermal conductance
g	Grams
H	Magnetic field strength
Hz	Hertz
I	Laser intensity
J	Joules
K	Kalvin
$k(\omega)$	Imaginary part of index of refraction
kg	Kilogram
L	Liter
m	Meters
MHz	Megahertz
N	Number of particles per unit volume
n	Complex index of refraction

$n(\omega)$	Real part of index of refraction
Nd	Neodymium
nm	Nanometer
ns	Nanosecond
Pa	Pascal
ps	Picosecond
Q'_w	Rate of heat loss from the particle to the surroundings
T_e	Electron temperature
Ti	Titanium
T_l	Lattice temperature
TW	Terawatt
$T_{w,s}$	Water temperature
V_p	Particle volume
ω	Oscillation frequency
W	Watt
α	Absorption length of material
ε	Complex dielectric function
$\varepsilon_1(\omega)$	Real part of the dielectric function
$\varepsilon_2(\omega)$	Imaginary part of the dielectric function
ε_m	Dielectric constant of the surrounding medium
η	Electric field enhancement
λ	Wavelength
λ_{eff}	Effective wavelength
λ_{max}	Resonance wavelength
λ_p	Plasma wavelength
σ	Surface tension
τ	Pulse duration

Chapter 1

Motivation and Thesis Objectives

1.1 Motivation

Ultrafast laser pulses are extremely short light pulses in between picosecond and femtosecond timescales. In recent years, the applications of such lasers have been growing rapidly and are found in many fields. Of particular interest is the use of femtosecond laser pulses in the life sciences applications. A femtosecond is one millionth of one billionth of a second time duration. Due to the high peak power of the laser pulses, laser-tissue interaction is substantially different compared to longer laser pulse lengths or continuous wave (CW) laser-tissue interaction. When high intensity laser pulse interacts with biological tissue, a process of non-linear absorption (i.e. when two or more photons are simultaneously absorbed) can take place which can strip electrons and ionize the material; thus, changing the chemical composition of the material. Since non-linear absorption process is intensity dependent, the interaction can be localized to a volume smaller than the diffraction limit [1-7]. For gaussian laser beam profile, the non-linear interaction occurs at the peak of the laser spot which is smaller than the actual full width half max (FWHM) of the focused laser beam. Additionally, since the laser-tissue interaction time is much shorter (<100fs) than the thermal relaxation time of the material (~1ps), the method of tissue modification / ablation is non-thermal in its nature, and thus leads to minimal heat dissipation, cavitation bubble, and shockwave formation [1-7]. These laser-tissue interaction qualities of femtosecond laser pulses has made them an increasingly important tool in the biomedical field, for developing new therapeutic and diagnostic medical devices.

1.2 Thesis Objectives

In this thesis, three main applications using femtosecond laser pulses are studied and developed:

1. A novel technique for precise cellular and neuronal attachment using femtosecond laser pulses. This technology will be used as a tool by scientists to develop new experiments and technologies related to tissue engineering and neuronal repair.

2. A technique to characterize the cellular membrane of cells that has gone through femtosecond laser induced attachment. This was used to demonstrate that the attachment takes place on the molecular level of the cellular membrane (through hemifusion) have been developed.

3. A new treatment for retinoblastoma cancer using gold nanorods and femtosecond laser pulses. For the treatment of retinoblastoma cancer, femtosecond laser pulses are combined with retinoblastoma targeting gold nanorods to induce highly localized cellular hyperthermia. Currently, the treatment of retinoblastoma cancer is mainly focused on the preservation of the child's life. In most cases, the children would lose their vision since the current modalities of treatment are extremely harsh. However, the method developed could provide another treatment modality for retinoblastoma where the children's vision could also be preserved. The combination of femtosecond laser pulse and gold nanorods results in an extremely robust treatment that require a small concentration of gold nanorods inside the cancer cells, to induce an effective treatment. Therefore, with additional future development, this proof of concept could potentially be translated into a clinical application.

1.3 Thesis Organization

This thesis is comprised of six chapters that detail the experimental and theoretical work performed. Chapter 2 introduces the underlying physics involved in light interaction with metallic nanoparticles. Chapter 2 also unifies the theoretical understanding of ultrashort laser and biological matter interaction. Some discussion on the cellular membrane and the process of

membrane fusion and hemifusion is also provided. In chapter 3, a proof of concept for the application of femtosecond laser pulses in combination with cancer targeting gold nanorods towards treatment of retinoblastoma is demonstrated. In chapters 4-5, novel applications of femtosecond laser pulse interaction with biological tissue are presented. In chapter 4, nanosurgical attachment of individual cells is presented. Also provided in chapter 4, a unique method for visualizing hemifusion is presented, which allows an in-depth analysis of the mechanism underlying femtosecond laser-induced surgical attachment is presented. In chapter 5, a novel method for selective and precise attachment of single neurons using femtosecond laser pulses is presented. Finally, in chapter 6, future prospects are provided.

Chapter 2

Photothermal Therapy Using Gold Nanoparticles¹ and Laser-Tissue Interaction

¹ Portions of this chapter have been published in: Katchinskiy *et al.* Anti-EpCAM Gold Nanorods and Femtosecond Laser Pulses for Targeted Lysis of Retinoblastoma. *Advanced Therapeutics*, 1(1): 1-10, **2018**.

2.1 Laser-Nanoparticle Interaction - Background and Chapter Objectives

Materials that are made into extremely small particles behave drastically differently than their bulk composition, as such investigation of nanoparticles have been rapidly increasing in recent years. In this chapter, light and metallic nanoparticle interaction is reviewed, primarily focusing on gold nanorods, and their application for selected cancer therapy. Under the excitation of optical field from light wave, metallic nanoparticles can enhance electric fields tens of times stronger than the incident field [8] while confining the enhanced field into a volume smaller than the diffraction limit [8]. When nanoparticles are exposed to the electric field from electromagnetic radiation (EM), the EM radiation can penetrate metal surface and stimulate oscillations of the free-electrons inside the metal within distance inversely proportional to the absorption length ($\frac{1}{\alpha}nm$, where α is the absorption length, and is dependent of the material, wavelength, and temperature)[9]. This EM response is coupled to a collective electron oscillations characteristic of coupled plasma. This phenomenon is called localized surface plasmons. Some examples of nanoparticles, such as nanorods (NR), nanospheres (NS), nanoshells (NSH), and nanocages (NC), are depicted in figure 2.1 below. When these structures are irradiated with light at their surface plasmon resonance, light absorption is enhanced, which leads to enhancement of the electric field, and increased temperature around the nanoparticles. Due to these properties, nanoparticles are used nowadays in many areas such as: (i) biomedical engineering, for cancer therapy and photodynamic therapy, (ii) solar cell industry, to enhance light absorption inside the solar cell material [10], (iii) spectroscopy applications [11], (iv) scanning near field microscopy [12], (v) imaging of chemical and biological components [12], (vi) photo-detection, (vii) sensing, etc.

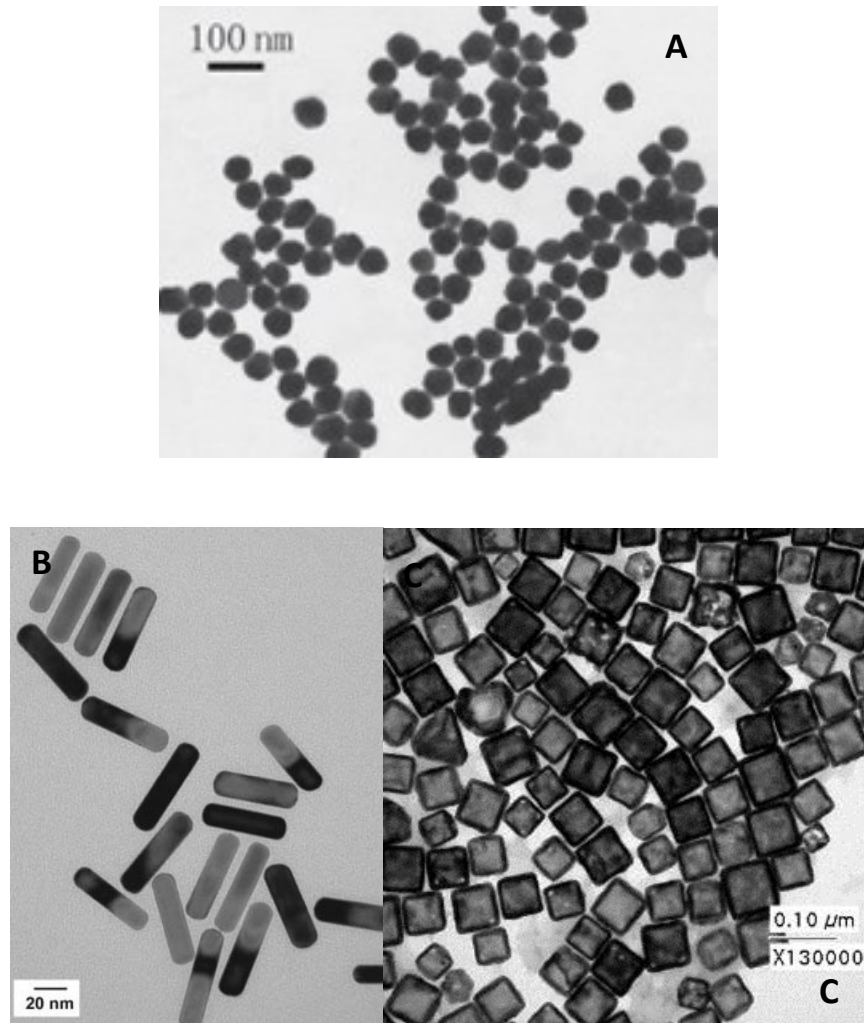


Figure 2.1: A. Various sizes of gold nanospheres [13]. B. Gold nanorods. C. Gold nano-cages (Image taken from <http://bit.bme.jhu.edu/Nanoparticles.html>).

2.1.1 NP Surface Plasmon Generation

Metals are conducting materials because the electrons in metals are free to move and not confined, since there is no separation between the conduction band and the valence band [14]. When light photons interact with a metallic surface, the conduction band electrons react to the light EM field, and if the incident light frequency is resonant with the frequency of the surface plasmons (coherent oscillation of the free electrons on the surface of the particle), the electrons move coherently under the influence of the external field. When ~10–200 nm gold nanoparticles are illuminated with light at their surface plasmon resonance, localized surface plasmon resonances (LSPRs) can be excited. As shown in figure 2.2, the electrons oscillate on the surface of the nanoparticles, giving rise to a net charge difference at the nanoparticle boundaries. This charge accumulation results in strong electron confinement that leads to the generation of strong electromagnetic fields at the metallic surface. The LSPR wavelength (λ_{max}) and extinction cross-section of gold nanoparticles are size and shape-dependent [14-16]. It is also highly sensitive to the capping agents and surrounding dielectric environment (i.e. permittivity) [14-16]. Generally, absorption and scattering processes are the causes of energy loss of electromagnetic wave (total light extinction) passing through material. Light absorption takes place when a photon energy is dissipated due to inelastic processes, and light scattering occurs when a photon energy causes electron oscillations in the matter which emit photons in the form of scattered light either at the same frequency as the incident light (Rayleigh scattering) or at a shifted frequency (Raman scattering). In Raman scattering, the frequency shift of the emitted photon corresponds to the energy difference required for molecular motion within the matter (molecular bond rotations, stretching or vibrations). Due to the SPR oscillation, the processes of light scattering and absorption are enhanced [14-16].

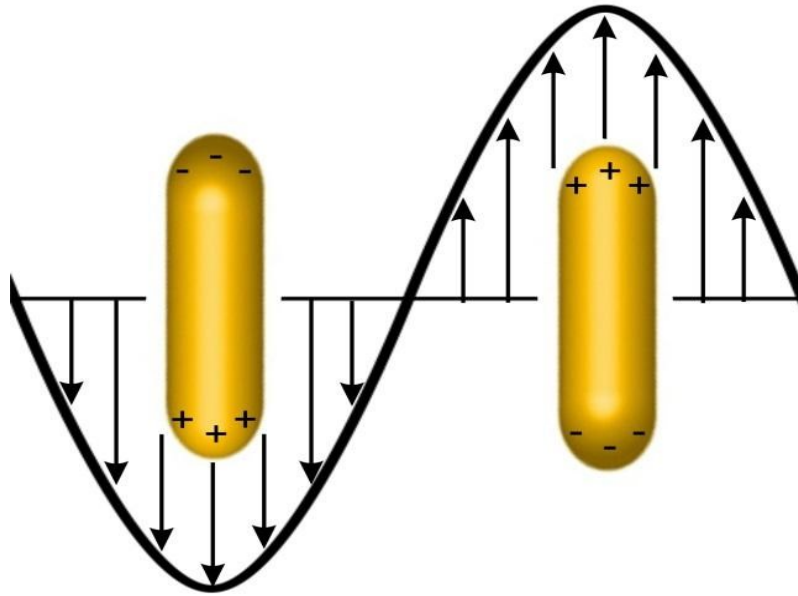


Figure 2.2: Schematic of the localized surface plasmon resonance on gold nanorod. Upon illumination at resonant wavelengths, conduction band electrons on the gold nanoparticle surface are delocalized and undergo collective oscillation.

For some biomedical applications, such as cancer treatment, it is advantageous to use nanoparticles that are as small as possible; for reasons that will be explained in Chapter 3. Gold NRs, in particular, can be made much smaller compared to other nanoparticle shapes (e.g. nanospheres) to absorb near-infrared (NIR) laser irradiation. For example, LSPR of 800nm can be achieved using 10nmx40nm gold NRs, compared to 400nm gold NS. When gold nanostructures are made in a rod-like shape (i.e. NRs), the LSPR is split into two frequencies: a strong extinction in the NIR region, corresponding to the electron oscillations along the long axis (longitudinal band), and a weak extinction in the visible region, corresponding to the short axis (transverse band). LSPR intensity and wavelength depends on the intrinsic properties of the nanoparticle, such as the metal type, particle size, shape, and structure, as theoretically described by Mie theory [17]. For gold NRs, according to Gan theory, the extinction coefficient γ can be expressed as [18]:

$$\gamma = \frac{2\pi NV \varepsilon_m^{\frac{3}{2}}}{3\lambda} \sum_j \frac{\frac{1}{P_j^2} \varepsilon_2}{\left(\varepsilon_1 + \frac{1 - P_j}{P_j} \varepsilon_m\right)^2 + \varepsilon_2^2} \quad (2.1)$$

where N is the number of particles per unit volume, V is the volume of each particle, λ is the wavelength of the incident light, ε is the complex dielectric constant of the metal given by $\varepsilon = \varepsilon_1(\omega) + i\varepsilon_2(\omega)$, $\varepsilon_1(\omega)$ is the real part and $\varepsilon_2(\omega)$ is the imaginary part of the dielectric constant of the metal, respectively, ε_m is the dielectric constant of the surrounding medium. P_j is defined as

$$P_A = \frac{1 - e^2}{e^2} \left[\frac{1}{2e} \ln \left(\frac{1 + e}{1 - e} \right) - 1 \right] \quad (2.2)$$

$$P_B = P_C = \frac{1 - P_A}{2} \quad (2.3)$$

$$e = \sqrt{1 - \left(\frac{B}{A}\right)^2} \quad (2.4)$$

where A, B and C are the three axes of the rods with $A > B = C$. The $R = A/B$ is the aspect ratio.

The plasmon resonance occurs when

$$\varepsilon_1 = -\frac{(1-P_A)\varepsilon_m}{P_A} \quad (2.5)$$

where P_A is the longitudinal polarization P_B, P_C are for transverse polarizations.

The complex index of refraction is defined as, $n = n(\omega) + ik(\omega)$, where n is related to the velocity of the electromagnetic wave and k , the extinction coefficient is related to the electromagnetic decay, or damping of the oscillation amplitude of the incident electric field. The complex dielectric constant of a material is related to its index of refraction as follows:

$$\varepsilon(\omega) = \varepsilon_1(\omega) + i\varepsilon_2(\omega) = (n + ik)^2 \quad (2.6)$$

$$\varepsilon_2 = 2nk \quad (2.7)$$

$$\varepsilon_1 = n^2 - k^2 \quad (2.8)$$

The Beer Lambert's law of absorption states that the absorption coefficient is defined as:

$$\alpha = \frac{4\pi}{\lambda} k \quad (2.9)$$

The Beer Lambert law states that the radiation is absorbed to an extent that depends on the wavelength of the radiation and the thickness and nature of the medium. The absorption coefficient is therefore described as the reciprocal of the penetration depth of radiation into a bulk solid, i.e., it is equal to the depth at which the energy of the radiation has decreased by the factor of $e^{-\alpha x}$.

Therefore, we can rewrite the imaginary part of the dielectric constant in terms of absorption:

$$\varepsilon_2 = \frac{n\lambda}{2\pi} \alpha \quad (2.10)$$

Thus, we can see that the imaginary part of the dielectric constant is directly proportional to the material absorption.

Now, replacing ε_2 in equation 2.1 in terms of equation 2.10, we can rewrite the total extinction coefficient for nanorods as:

$$\gamma \sim \sum_j \frac{\frac{1}{P_j^2} \frac{n\lambda\alpha}{2\pi}}{\left(\varepsilon_1 + \frac{1-P_j}{P_j} \varepsilon_m\right)^2 + \left(\frac{n\lambda\alpha}{2\pi}\right)^2} \sim \sum \frac{1}{\alpha} \quad (2.11)$$

Using this approximation, we can conclude that the extinction cross section of more lossy metals results in smaller extinction values, which will in turn result in lower absorption cross section (i.e. since the absorption cross section is the dominant process for particles that are smaller than 50nm [19]). For example, the absorption cross section of a 60 nm diameter silver is on the order of $2e^{-14}$ [20], a 60 nm diameter gold nanospheres is on the order of $1e^{-14}$, and a 60 nm diameter platinum nanospheres is on the order of $3e^{-15}$ [21].

At wavelengths between 500 and 850 nm the resonance is found to be nearly linear according to the following relation:

$$\varepsilon_1(\lambda) = 34.66 - 0.07\lambda \quad (2.12)$$

In the aqueous solution, the linear proportional relationship between the longitudinal SPR absorption maximum and the aspect ratio of the nanorods for wavelength between 500-850nm can be expressed as [14]:

$$\lambda_{max} = 95R + 420 \quad (2.13)$$

where $R = A/B$ is the gold NR aspect ratio.

2.1.2 Effective Wavelength

In radio-frequency (RF) antenna theory the ideal half-wave dipole antenna is made of thin rod of length $L = \frac{1}{2}\lambda_{eff}$ [9]. However, in the optical frequency regime the EM waves are not perfectly reflected from the surface of the metal, but penetrate the metal with decay scale that depends on the type of metal and the EM frequency [9]. The EM field inside the metal stimulates oscillations of the free-electron gas inside the conductor. Thus, the optical antenna no longer responds to the external excitation wavelength but to a shorter effective wavelength that depends on the frequency of the EM wave and the material properties [9]. An effective wavelength is derived by taking the complex surface impedance of the metal into account; however, when the length of the antenna is comparable to the skin depth, the concept of surface impedance breaks down [9]. In this case, the EM response is dictated by the collective electron oscillations characteristic of a strongly coupled plasma [9]. Novotny [9] derived a linear scaling law for the effective wavelength in the form of:

$$\lambda_{eff} = n_1 + n_2 \left[\frac{\lambda}{\lambda_p} \right] \quad (2.14)$$

where λ_p is the plasma wavelength, and n_1, n_2 are coefficients with dimensions of length that depend on the antenna's geometry and static dielectric properties. This approximation applies for antennas with radius $R \ll \lambda$.

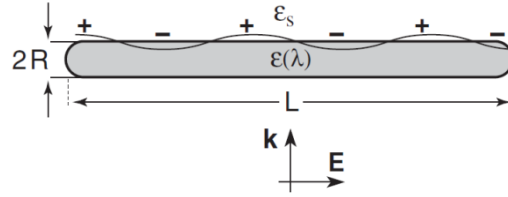


Figure 2.3: Surface polarization of metallic rod having a length L and radius R , due to incoming EM wave with electric field E parallel to the nanorod's axis. k is the wave-number of the EM wave[9].

Figure 2.3 depicts the effect of EM wave incident on a metallic nanorod, where the incident light polarizes the surface of the nanorod. It is noticeable that only for specific wavelengths the ends of the rod are polarized such that they give rise to a standing surface charge. Novotny [9] calculated the effective wavelength of nanoparticle and evaluated the effective wavelength while changing the nanorod's radius. The results are plotted vs. the incident light wavelength and shown in figure 2.4. Clearly, as seen in figure 2.4, for the nanorod structures, much shorter effective wavelength can be achieved compared to incident wavelength.

Another useful depiction of the effects of incident EM wave on a metallic structure is shown in figure 2.5, where the surface polarization of the particle is shown for varying frequencies of EM waves. We note that for even modes (i.e. 0, 2, 4,...) the surface of the nanorod is polarized at same charge polarity at its ends, whereas for odd modes (i.e. 1, 3, 5,...) the surface of the nanorod is polarized with its ends being polarized with opposite charges, leading to standing surface charge. Viewing this figure helps us more intuitively understand the effect of EM fields on metallic structures, and what are the causes for E-field confinement, and resonance. For each structure there are multiple resonance modes, which depend on the incident wavelength.

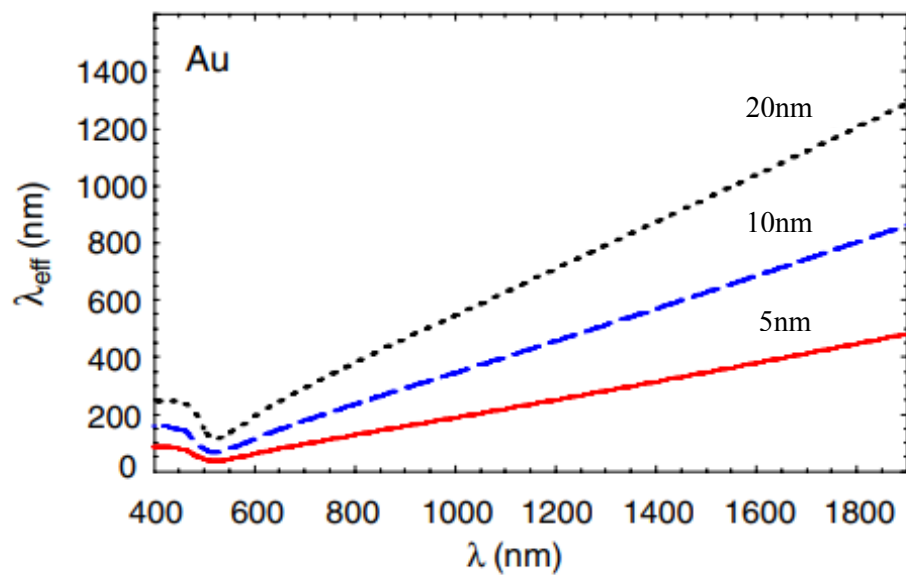


Figure 2.4: Effective wavelength of gold nanorods vs/ incident light wavelength, for varying rod radius 5nm, 10nm, and 20nm [9].

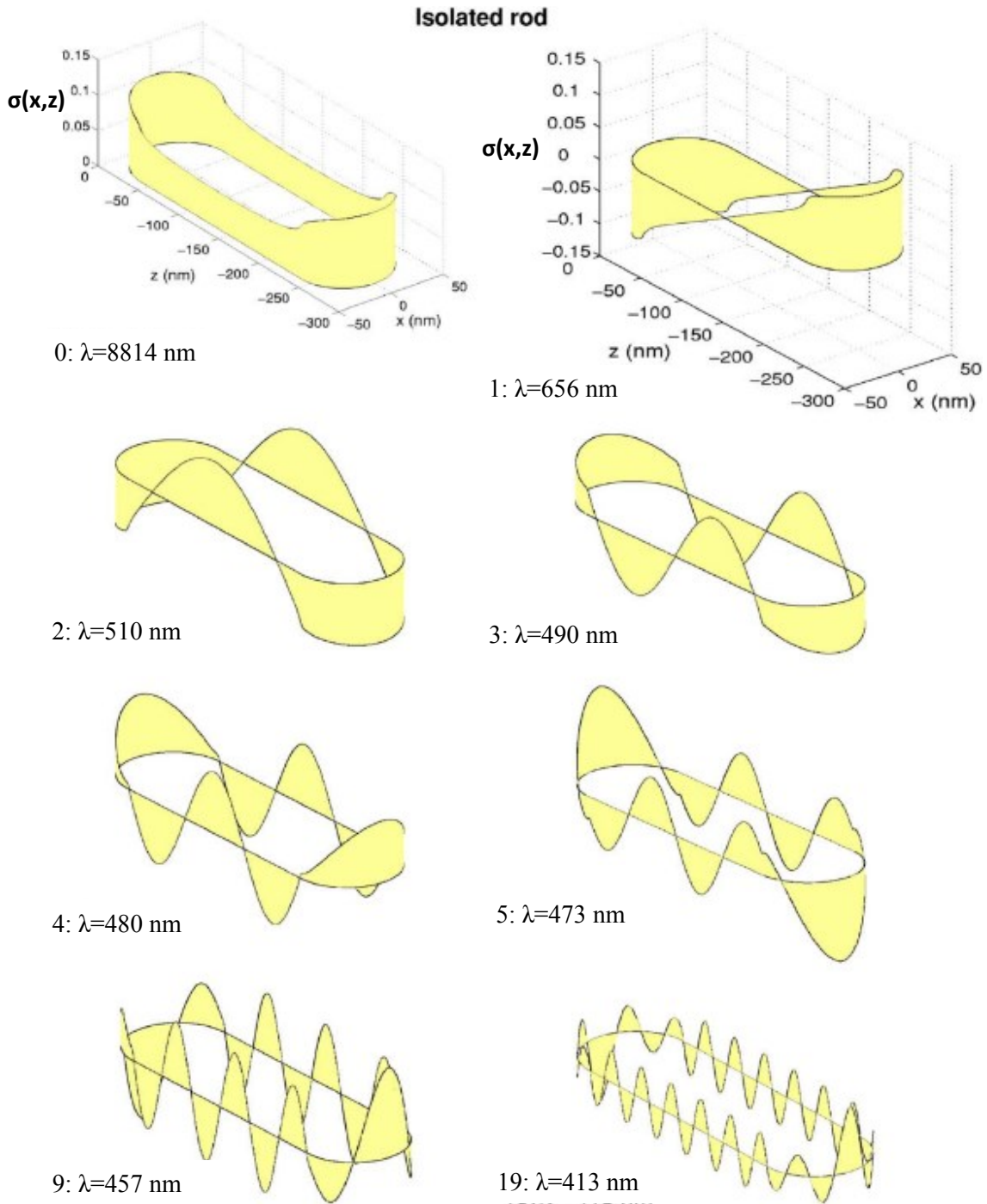


Figure 2.5: Surface charge polarization of gold nanorod ($L=200\text{nm}$, $R=40\text{nm}$) due to EM wave with different frequencies [22].

Shown in figure 2.6 is gold nanorod having length L , and radius R . The Au nanorod is illuminated by EM wave with electric field E , parallel to the nanorod's length axis.

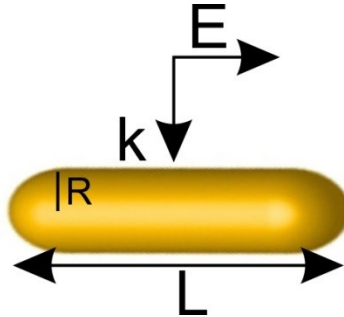


Figure 2.6: Orientation of Nanorod with length L and radius R , interacting with EM wave with electric field E parallel to the nanorods axis. K represents the wave number of the EM wave.

When L was slowly increased, its extinction cross-section and resonance frequency were measured, and plotted in figures 2.7 and 2.8, respectively, it is seen that this results in a red-shift of its resonance wavelength. This red-shift in resonance is attributed to an increasing separation between the dipole charges, which in turn, reduces the restoring force that determines the oscillation frequency [22]. In addition, increasing the rod length results in a decrease of total extinction strength.

It is seen from figures 2.9, and 2.10 that an increase in nanorod radius results in blue shifting of the resonance wavelength for a small range of nanorod radius. Whereas, beyond a certain nanorod radius size the resonance wavelength experienced a red-shift for increasing radius size. According to G. W. Bryant et al., “at small R , the resonance varies inversely with R , blue-shifting with increasing R , as would be expected for the quasi-static limit where the resonance depends only on the aspect ratio. For larger R the resonance increases monotonically at fixed rod length, red-shifting for increasing R as for spherical particles” [23]. Beyond a certain radius, the

NR resembles a spherical object, as such, the total size of the particle dictates the resonant wavelength; therefore, larger particle will exhibit a longer resonant wavelength.

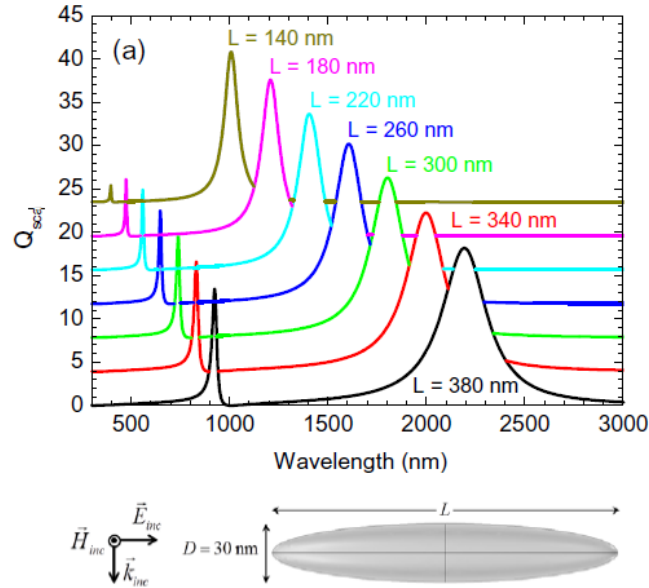


Figure 2.7: Effect of increasing nano ellipsoid length L on extinction cross-section [8]. Increased length L results in red-shift of extinction resonance, while reducing the extinction strength.

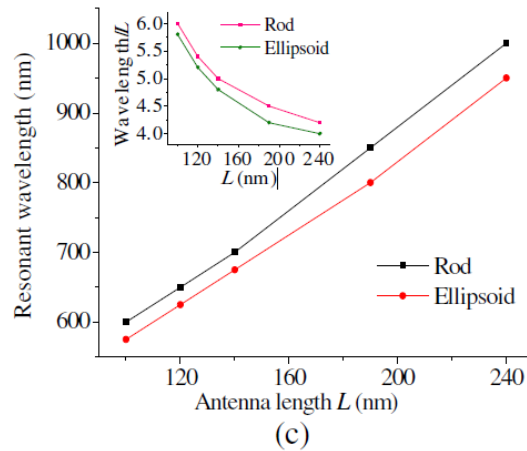


Figure 2.8: The linear relationship between a single gold nanorod and nano-ellipsoid resonance wavelength vs. nanoparticle’s length L [8]. Inset figure depicts relationship between single gold nanorod and nano-ellipsoid resonance wavelength divided by its length vs. the nanoparticle’s length L .

Figure 2.10 shows that a linear relationship was found between the resonance wavelength and the rod aspect ratio ($L_{tot}/2R$); this indicates that the dimension of each element (radius and length) by itself will not linearly affect the resonance of the particle, and may steer the resonance in opposite directions. However, the ratio between the rod length and its radius is important and will determine the LSPR. The ratio between the length and the radius can be thought of as how sharp the tip is compared to the overall size of the nanoparticle. That is, if the rod is extremely short, only an extremely small radius will make it appear sharp, whereas, an extremely long rod will appear sharp for a wider range of radii. Sharper ‘looking’ rods may stimulate lightning rod effects, and stronger E-field enhancement, which will increase the strength of the extinction, and will determine the resonance wavelength.

2.1.3 E-field Enhancement

It is important to examine the ability of gold nanorods to enhance the interacting electric field. Metals are materials that possess a negative real and small positive imaginary dielectric constant, thus, can support a surface plasmon resonance (SPR). This resonance is a coherent oscillation of the surface conduction electrons excited by electromagnetic (EM) radiation. For the case of localized surface plasmons, light interacts with subwavelength size particles. This leads to a plasmon that oscillates locally around the nanoparticle with a frequency known as the LSPR (seen in figure 2.2). The LSPR is sensitive to changes in the local dielectric environment.

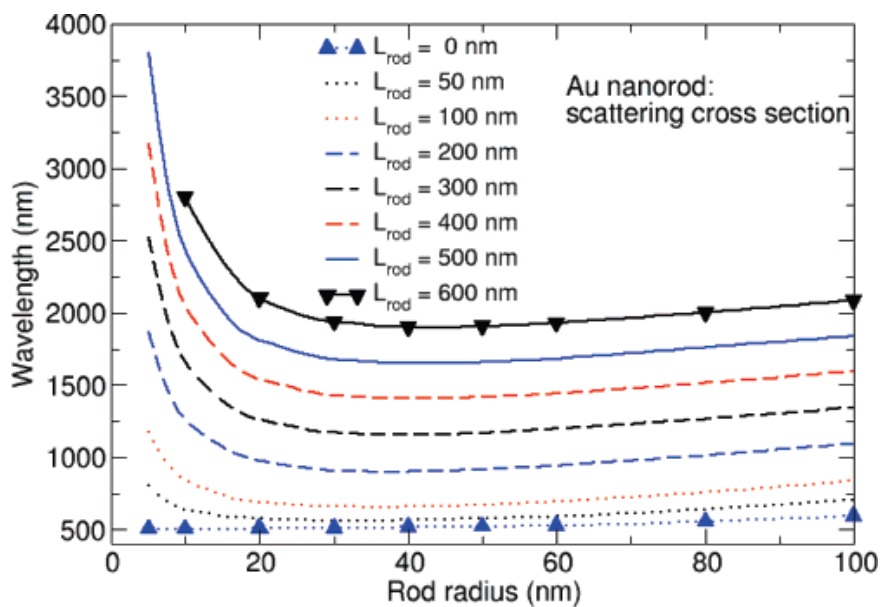


Figure 2.9: Gold nanorod resonance wavelength vs. rod radius [23]. Curves calculated for nanorods with varying lengths L_{rod} between 0nm and 600nm. Initial blue-shift in resonant wavelength, followed by red-shift with increasing radius.

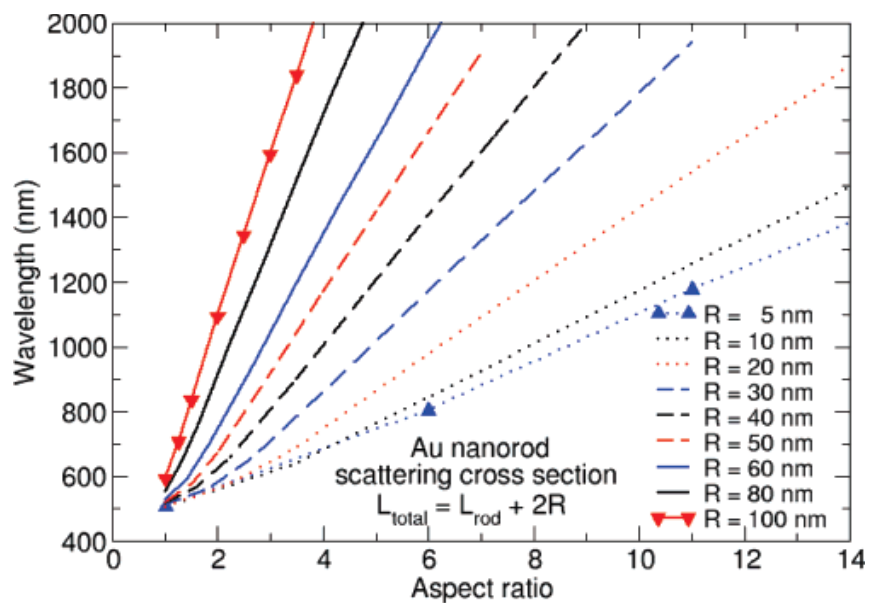


Figure 2.10: Gold nanorod resonance wavelength vs. gold nanorod aspect ratio (L/R) [23]. Curves calculated for nanorods with varying nanorod radius R between 5nm and 100nm. Linear relationship between aspect ratio and resonance wavelength is shown.

Consider a z-polarized wave electromagnetic field oscillating at frequency ω and propagating along the x-direction, and:

$$E_z = E_0 \hat{z} \cos(kx - \omega t) \quad (2.15)$$

Since the particle is much smaller than the wavelength, the long wavelength approximation, $kx \ll \omega t$, can be made, and the electric field can be rewritten as:

$$E_z = E_0 \hat{z} \cos(\omega t) \quad (2.16)$$

Additionally, as the particle experiences an external applied field E_z^0 which approximately constant in time, the Maxwell's equations governing the electric and magnetic field of the nanoparticle reduce to the equations for electrostatics and magnetostatics.

$$\nabla \cdot E = \frac{\rho}{\epsilon_0}, \quad \nabla_{\times} E = 0, \quad \nabla_{\times} H = \frac{j}{\mu_0 \epsilon_0 c^2}, \quad \nabla \cdot H = 0 \quad (2.17)$$

Solving Maxwell's equation results in a solution for the electric field at distance r outside a spherical particle with radius a :

$$E_{out}(x, y, z) = E_0 \hat{z} - \left[\frac{\epsilon_{in} - \epsilon_{out}}{\epsilon_{in} + 2\epsilon_{out}} \right] a^3 E_0 \left[\frac{\hat{z}}{r^3} - \frac{3z}{r^5} (x\hat{x} + y\hat{y} + z\hat{z}) \right] \quad (2.18)$$

where, ϵ_{in} is the complex dielectric constant of the metal nanoparticle, and ϵ_{out} is the dielectric constant of the external environment. Because ϵ_{in} is strongly dependent on wavelength, the first term in the square brackets determines the dielectric resonance condition for the particle. When the dielectric constant of the metal is roughly equal to $-2\epsilon_{out}$, the EM field is **enhanced** relative to the incident field.

According to K. Tanabe [24], the electric field enhancement factor can be calculated from electric field equation and is defined as $\eta = \left| 1 + 2 \frac{a^3}{r^3} \frac{\epsilon_{in} - \epsilon_{out}}{\epsilon_{in} + 2\epsilon_{out}} \right|^2$. Based on the E-field

enhancement equation and simulation of the electric field enhancement of various metallic nanoparticles, K. Tanabe [24] concluded that materials with smaller values of imaginary part of dielectric function at the resonant wavelength for the metals lead to higher peaks of the field enhancement factor for metal nanoparticles. Dielectric materials with smaller real and imaginary dielectric function values, i.e. higher optical transparency, are more favorable to enhance fields. In other words, metals that are considered less lossy will enhance the electric field more. The calculated E-field enhancement factor for various metals in water and air, and his results are presented in figure 2.11.

As expected, the electric field enhancement at the tips of the rod was found to be a few orders of magnitude larger in structures with sharper tips. However, the space volume at which the E-field enhancement occurs is drastically smaller for sharper tipped objects. The normalized electric field distribution of gold nanorod and nano-ellipsoid antennas effects can be seen by comparing figures 2.12 and 2.13. The figures depict nanoparticles suspended in air with $L = 100$ nm, $R = 20$ nm at $\lambda = 600$ nm incidence. The incident plane wave is in z-direction and the electric field is polarized in x-direction. The electric field enhancement of Au nano-ellipsoid is 363 V/m compared to only 99.2 V/m for Au NR. Similarly, increasing of the rod length increases the E-field enhancement. Sharper object will experience an additional enhancement with increasing rod length, as seen in figure 2.14.

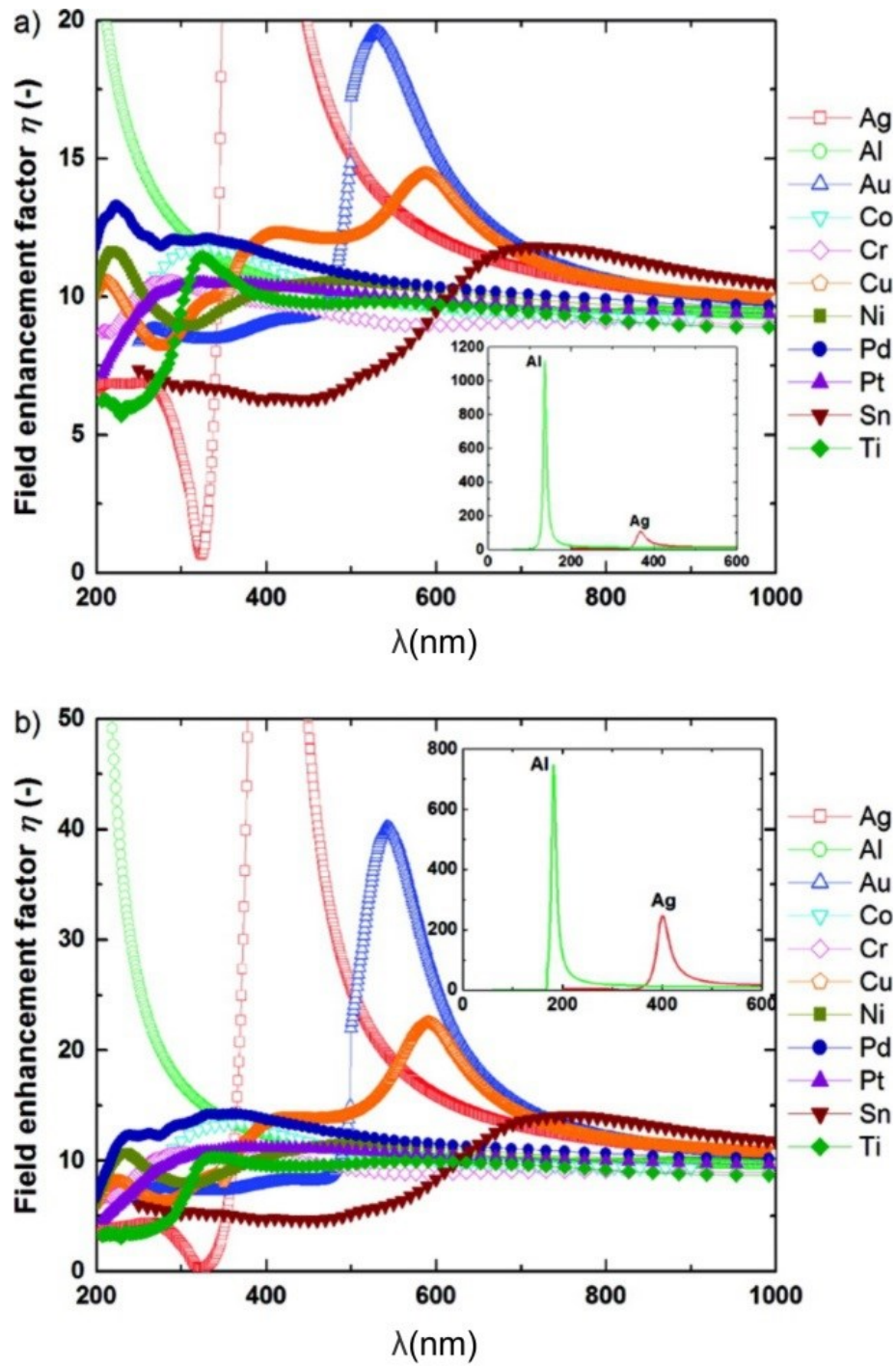


Figure 2.11: Calculated electric field enhancement factors, η , of spherical metal nanoparticles of 11 metals immersed in a) air, b) water [24].

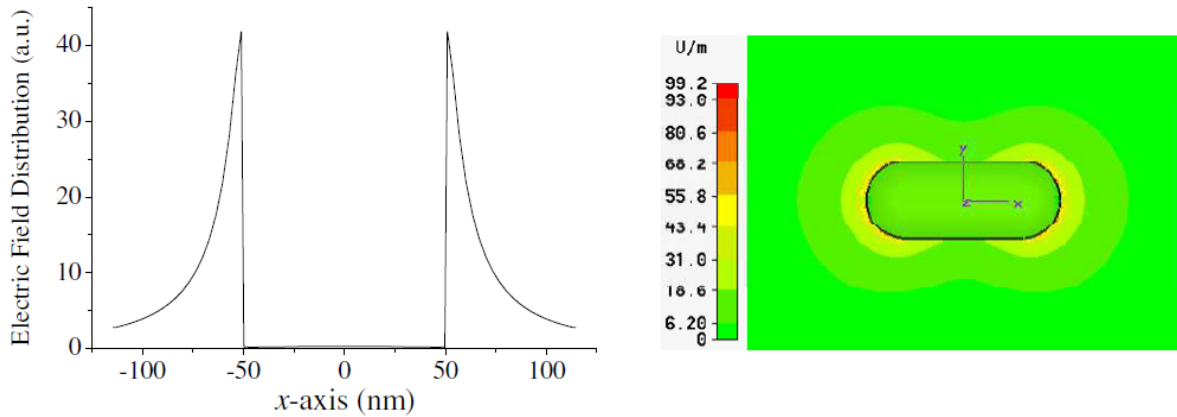


Figure 2.12: Normalized electric field distribution of gold nanorod antenna suspended in air with $L = 100$ nm, $R = 20$ nm at $\lambda = 600$ nm incidence. The incident plane wave is in z direction and the electric field is polarized in x direction [8]. On right is a 2D map of electric field (V/m) enhancement (E_{out}/E_{in}).

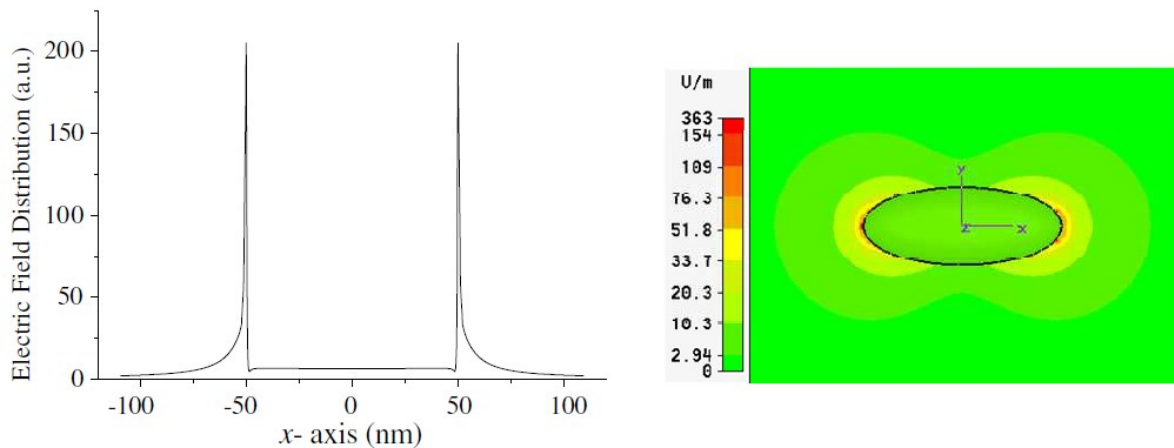


Figure 2.13: Normalized electric field distribution of gold nano-ellipsoid antenna suspended in air with $L = 100$ nm at $\lambda = 600$ nm incidence. The incident plane wave is in z direction and the electric field is polarized in x direction [8]. On right is a 2D map of electric field (V/m) enhancement (E_{out}/E_{in}).

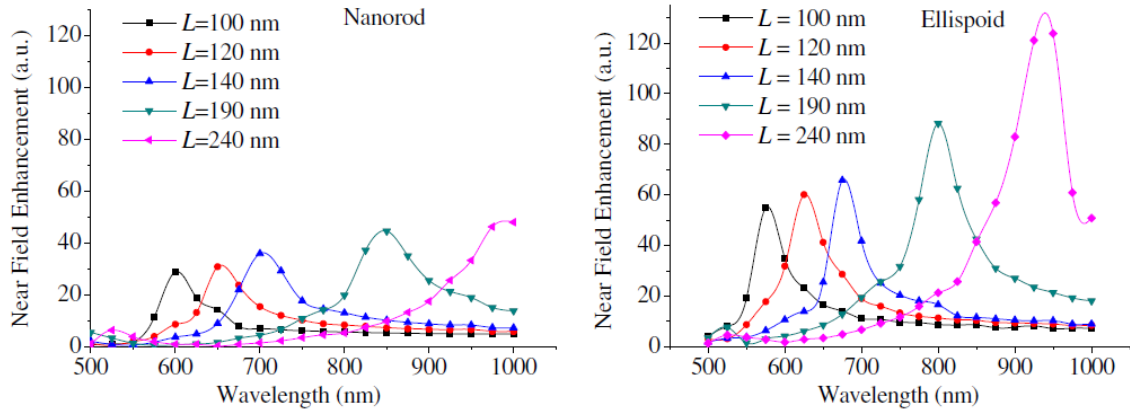


Figure 2.14: Electric field enhancement vs. incident wavelength. Calculations carried out for varying lengths L of nanorod / nanoellipsoid length, between 100nm-240nm [8]. Increase in length of gold nanoparticle leads to red-shift in resonance wavelength and increased E-field enhancement.

2.1.4 Nonradiative Properties of Gold

The dissipation of LSPR excitation into heat via a series of non-radiative processes has been extensively studied [25-27]. Upon excitation of the metallic nanoparticle (NP) with an ultrashort laser pulse, conduction band electrons absorb the photon via free carrier absorption. This process is followed by a fast phase-loss of the coherently excited electrons (within <50fs) resulting in thermalization of the electrons due to electron-electron scattering, with Fermi-Dirac energy distributions at a common electron temperature T_e . Approximately, 1 ps later, electron-phonon interactions transfers the electron energy to the lattice, resulting in a hot lattice [25]. This relaxation process is independent of size, shape, transverse or longitudinal surface plasmon modes. Since the thermal capacity of electrons, C_e , is much lower than the thermal capacity of the lattice, C_l , high electronic temperature, $T_e=10^5\text{K}$ can be reached within the first 100fs in the NP while the lattice temperature T_l increases by only 100K. Next, three processes can take place:

- (1) If the excitation optical intensity is high, this can lead to fragmentation and ablation of the

NPs. (2) At a moderate optical excitation intensity, T_l can reach the melting temperature of the NPs [28,29]. (3) The nanoparticles cool off by transferring their heat to the surrounding medium via phonon–phonon relaxation within ~ 100 ps. This process leads to heating-up of the surrounding medium by hundreds of degrees.

2.1.5 Pulsed laser – NP heat transfer for NP Immersed in Water

The electron and the lattice temperatures of the nanoparticles can be described mathematically using the two-temperature model

$$C_e(T_e) \frac{\partial T_e}{\partial t} = -g(T_e - T_l) + \frac{E_{\text{abs}}}{V_p \cdot \tau_p} \quad (2.19)$$

$$C_l \frac{\partial T_l}{\partial t} = g(T_e - T_l) - \frac{Q'_w}{V_p} \quad (2.20)$$

where C_e and C_l are the electronic and lattice heat capacities; V_p is the volume of the NP, τ_p is the laser pulse width, E_{abs} is the laser pulse energy absorbed by the particle, T_e is the electron temperature; T_l is the lattice temperature; g is the electron–phonon coupling constant (2×10^{16} $\text{Wm}^{-3}\text{K}^{-1}$), Q'_w is the rate of heat loss from the particle to the surroundings [30]. The laser energy absorbed by the particle is

$$E_{\text{abs}} = A_{\text{abs}} \cdot F_{\text{pulse}} \quad (2.21)$$

where F_{pulse} is the laser fluence and A_{abs} (3771 nm^2 for $14\text{nm} \times 48\text{nm}$ Au NR [30]) is the absorption cross-sectional area of the NR.

The rate of heat loss from the particle to the surrounding material is

$$Q'_w = A_{\text{surface}} \cdot G \cdot (T_l - T_{w,s}) \quad (2.22)$$

where $T_{w,s}$ is the water temperature at the surface of the particle, G ($105 \times 10^6 \text{ W/m}^2\text{K}$) is the thermal conductance at the particle/fluid interface, and A_{surface} is the surface area of the particle.

Ekici et al. [30] have calculated the temperature of gold nanorod (AuNR) in water medium that was irradiated with $\lambda=760\text{nm}$, 250fs long laser pulse at, fluence of 4.7 J/m^2 , and a peak irradiance of 2 GW/cm^2 . They simulated the temperature of electrons, gold lattice and of the water of $48\times 14\text{nm}$ gold nanorod surrounded by water. The results are shown in figures 2.15 and 2.16.

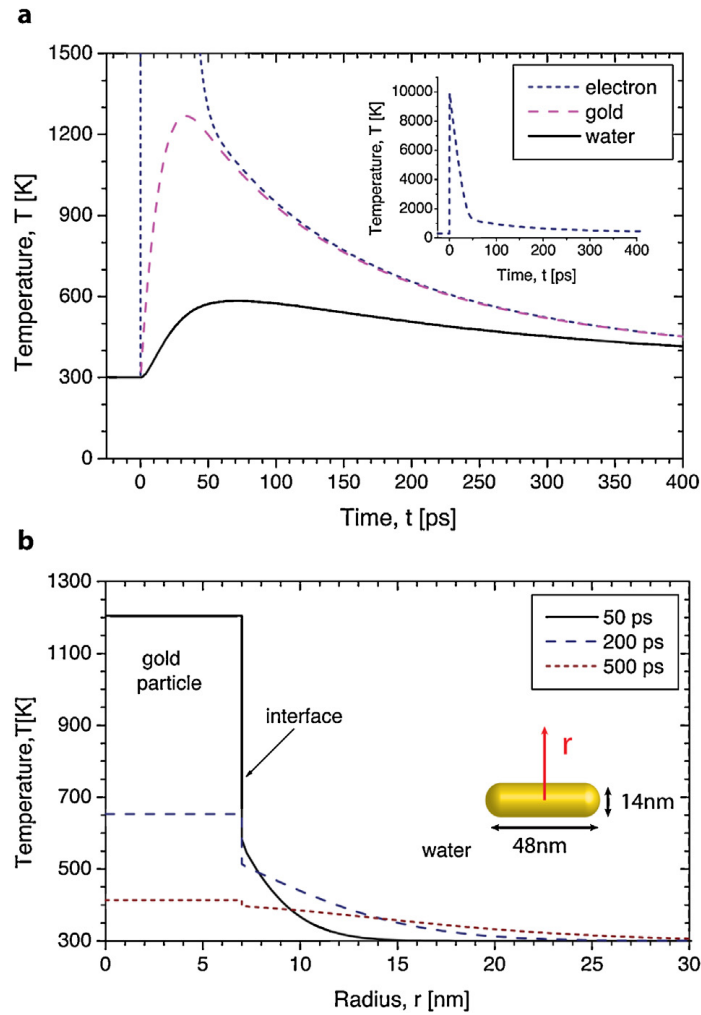


Figure 2.15: (a). Time evolution of temperature [K] profiles of $48\text{ nm} \times 14\text{ nm}$ AuNR and its surrounding water at the surface following irradiation with a laser pulse of fluence, $F_{\text{pulse}} = 4.70\text{ J m}^{-2}$. (b) Temperature profiles at different times after laser exposure as a function of radial distance at the mid-length of the nanorod [30].

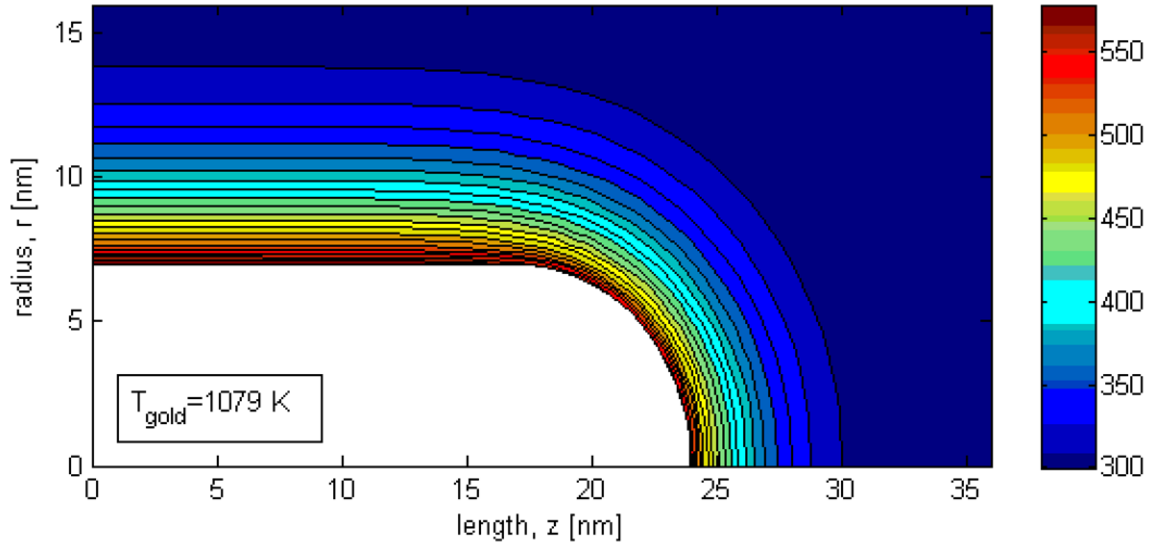


Figure 2.16: Temperature distribution in water surrounding the $48 \times 14 \text{ nm}^2$ gold nanorod taken at 70 ps after irradiation by a 250 fs laser pulse with an average fluence of 4.70 Jm^{-2} [30]. Color map is temperature in Kelvin.

After 50ps, the water temperature at the metal interface reaches 580K and quickly decreases as moved away from the particle in any direction where the temperature drops to 300 K (defined as the thermal penetration) in approximately 7nm. As time passes, the temperature at the interfaces drops to 500K (after 200ps) and 400K (after 500ps), while the thermal penetration increases to 15nm (after 200ps), and 20nm (after 500ps).

The effects of multiple laser shots on the temperatures of the gold nanorod and its surrounding water was also simulated. Figure 2.17 presents the temperature profile of the water and the surface of the gold nanorods for a duration of 1 μs . The nanorods are excited by 80 laser pulses arriving at 12.5 ns time intervals from an 80 MHz repetition rate laser system. It was found that the temperatures of the electron and lattice of the particle and the temperature of water at the particle surface equilibrate before the arrival of the next pulse. It was also found that an overall

temperature rise of only 3 K is calculated during the first few pulses and thereafter no significant temperature increase is observed.

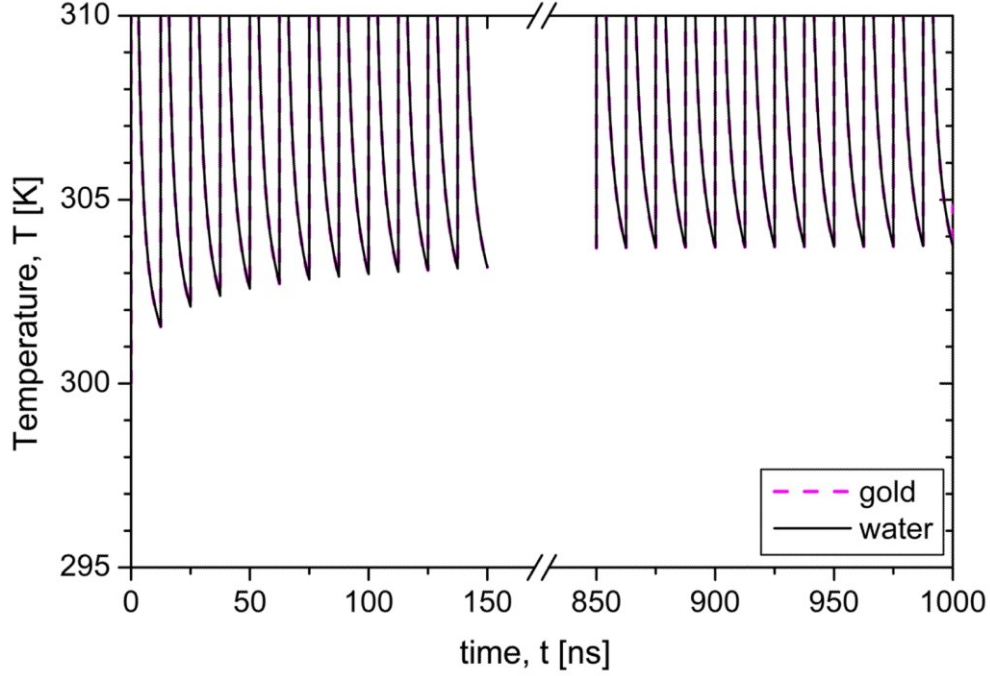


Figure 2.17: Time evolution of temperature profiles of $48 \times 14 \text{ nm}^2$ gold nanorod and its surrounding water at the surface during a $1 \mu\text{s}$ time duration of multiple laser exposures at a repetition rate of 80MHz with $F_{pulse} = 4.70 \text{ Jm}^{-2}$ [30].

According to S. Link et al. [31], the temperature of the gold nanorods after excitation with femtosecond pulses as a function of the laser fluence can be calculated using equations 2.23-2.25.

$$T = \frac{E_{abs}}{mc_p} + 293 \quad (2.23)$$

$$T = \frac{E_{abs} - \Delta H_{melt}}{mc_p} + 293 \quad (2.24)$$

$$T = \frac{E_{abs} - \Delta H_{melt} - \Delta H_{vap}}{mc_p} + 293 \quad (2.25)$$

where ΔH_{melt} and ΔH_{vap} are the heat of melting and vaporization of gold, respectively. c_p is the specific heat capacity of gold (0.129 J/g°C) and m the mass of the nanoparticle ($\sim 10^{-20}$ kg). Equation 2.23 holds for temperatures below the melting point, while equations 2.24 and 2.25 are used when the temperatures have reached values above the melting and boiling point, respectively.

Figure 2.18 shows the temperature of the gold nanorods after excitation with 100 femtosecond laser pulses as a function of the laser fluence. The two horizontal lines indicate the bulk melting and boiling temperatures of gold at 1337 and 2929 K, respectively. The calculations were carried out assuming an overall nanorod concentration of about 5.7×10^{-10} mol/L. E_{abs} is the photon energy absorbed by each nanorod, and obtained from the optical density of the nanorod sample. Furthermore, it was assumed that all the absorbed laser energy is transferred into the lattice.

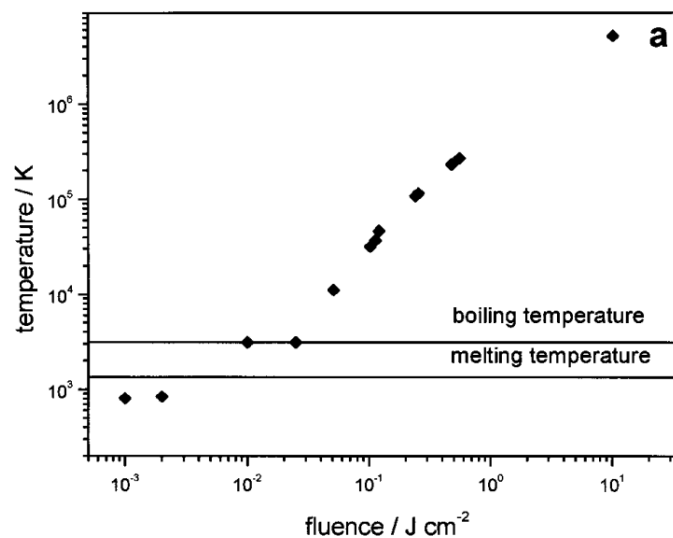


Figure 2.18: Estimated nanoparticle gold lattice temperature [K] as a function of the laser fluence [J cm⁻²] [31]. Increased fluence leads to increased temperature. Melting and boiling temperatures are noted.

S. Link et al. [31] and Y. Li et al. [32] reported that at laser fluences above $\sim 1 \text{ Jcm}^{-2}$, gold nanorods result in melting and the lattice temperature surpass 1400K.

It is important to note that pulses with pulse duration longer than 1ps, have a pulse length that is longer than the electron–phonon equilibrium time of about 1–3 ps. As such, the energy transfer from a 1ps or longer laser pulses to a plasmonic nanoparticle embedded in water, heats both the electron and phonon subsystems simultaneously to become in thermodynamic equilibrium with one another.

2.1.5.1 Heat Transport Between Gold Nanorod and Water

The rate of heat loss from, Q' , a nanorod to its surrounding water is calculated based on the interfacial conductance and is given by:

$$Q' = G(T_g - T_w) \quad (2.26)$$

where G is the interfacial conductance across the nanorod-water interface ($1.05 \times 10^8 \text{ W/m}^2\text{K}$ for Au), T_g is the temperature of gold and T_w is the temperature of water. The thermal conductance relates the temperature drop at an interface to the heat flux crossing the interface. The heat loss Q' is proportional to the transient temperature response of the water adjacent to a heated gold nanorod, and is given by:

$$Q' = \rho_p R C_p \frac{dT_w}{dt} \quad (2.27)$$

where $C_p = 0.129 \text{ kJ/kg K}$ (specific heat capacity of gold), ρ_p is the density of gold (19.32 g/cm^3), and R is the radius of the nanoparticle.

Assuming negligible losses from heat radiation and convection, from Eqs. 2.26 and 2.27 we get [33]:

$$\rho_p R C_p \frac{dT_p}{dt} = G(T_g - T_w) \quad (2.28a)$$

Solving equation 2.28a,

$$\frac{1}{T_g - T_w} \frac{dT_p}{dt} = \frac{G}{\rho_p R C_p} \quad (2.28b)$$

$$\int_{300}^T \frac{dT_p}{(T_g - T_w)} = \frac{G}{\rho_p R C_p} \int_0^t dt \quad (2.28c)$$

results in:

$$\frac{T - T_g}{300 - T_g} = \exp\left(-\frac{Gt}{\rho_p R C_p}\right) \quad (2.28d)$$

From equation 2.28d, the temperature of the water surrounding gold nanoparticle can be calculated. Assuming a nanoparticle with radius $R=10\text{nm}$, and starting temperature of 1500K , after 100ps , the water temperature reaches 714K .

$$T = 1500 - 1200 \exp\left(-\frac{Gt}{\rho_p R C_p}\right)$$

$$T = 1500 - 1200 \exp\left(-4.23 * 10^9 \left[\frac{1}{s}\right] * 100 * 10^{-12}[s]\right) = 714K$$

A rough estimate of the change in temperature of a **continuous-wave** laser-irradiated nanoparticle solution can be made using [34]:

$$Q = mc\Delta T \quad (2.29)$$

where Q is energy, m is mass, and c is the specific heat capacity of water ($4.8 \text{ J/g}^\circ\text{C}$).

For example, a 100 mW (mJs^{-1}), 785 nm laser irradiating a 1ml solution of water for 10 mins (600s) will deposit 60J of energy. For a typically used AuNR solution with absorption of $A=1$ at 785 nm , the light transmittance is 10% , and 90% of that light would be absorbed/scattered by the particles. This can be calculated using the beer's law:

$$A = 2 - \log(\%T) \quad (2.30)$$

where A is absorbance, and $\%T$ is percent transmittance.

Given that most of the extinction is due to absorbance, 54J would be absorbed by the solution. Then the change in temperature of the water would increase by ~ 11 °C, given 100% photothermal efficiency.

2.1.6 Bubble Formation

Bubble is a high temperature water vapor that forms around the NP, which expands in size and eventually collapses. Heat transfer from the particle's surface to the water may cause phase change and bubble formation in the surrounding liquid [35]. The formation of bubbles in a liquid in contact with a short or ultrashort laser pulse heated surface is hence usually associated to the phenomenon of phase explosion. The relaxation from the low pressure and high temperature unstable state to the equilibrium state involves a significant pressure increase, hence the name phase explosion.

Once a bubble is created, it expands and collapses in a ~ 100 ps to ~ 1 μ s, depending on the laser pulse duration and energy [35]. The bubble shields the surrounding water from conducting the heat from the particle due to the low thermal conductivity of the water vapor. The vapor bubble creates a region of modified refractive index around the particle that modifies its interaction with the electromagnetic field. Furthermore, a bubble scatters a significant proportion of the incoming electromagnetic energy. Therefore, if the energy deposition into the NPs is much faster than the bubble formation time, such as in the case of femtosecond laser pulses, the majority of the pulse energy is absorbed before the bubble nucleation onsets. After nucleation, the bubble's expansion is dictated by the vapor pressure and temperature which are initially high. The pressure and temperature decreases as the bubble expands due to heat conduction with the surrounding

medium. The pressure from the liquid surrounding the bubble and its surface tension limit the bubble growth, which eventually reaches a maximum radius, and collapses. The duration of the collapse stage is similar to the duration of growth. Shock-wave generation and plasma formation are usually associated with the collapse of cavitation bubbles [36,37].

The dynamics of a spherical bubble in an infinite body of liquid, known as the Rayleigh-Plesset equation [35]:

$$\rho_L \left(RR'' + \frac{3}{2} R'^2 \right) = p_0 \left(\frac{R_0}{R} \right)^{3\kappa} - p_w - \frac{2\sigma}{R} - \frac{4\mu R'}{R} \quad (2.31)$$

where R is the bubble radius, R' and R'' are the first and second time derivatives of R , R_0 is the initial radius, ρ_L is the liquid density (incompressible), p_0 is the initial pressure, p_{ext} is the pressure of the surrounding liquid, σ is the surface tension and μ is the viscosity. κ is an exponent characterizing the expansion/compression.

Note that, this equation assumes incompressible fluid and applies when heat conduction from the bubble to the surrounding liquid and mass transport across the bubble boundary (from evaporation or condensation) are neglected. [38].

By setting an initial radius and viscosity, equation 2.31 can be solved for R . R_0 , p_0 and κ are usually varied to fit experimental data. From equation 2.31, the relation between the bubble lifetime (τ_{bubble}) to its diameter d^{max} [38] can be written as.

$$\tau_{bubble} \sim 0.915 \sqrt{\frac{\rho_L}{p_{ext} - p_{sat}(T_w)} d^{max}} \quad (2.32)$$

T_w is the temperature of the surrounding water and p_{sat} is the saturation pressure (i.e. the maximum pressure possible by water vapor at a given temperature). Considering $T_w=293\text{K}$, $p_{ext} = 101 \text{ kPa}$, $\rho_L = 998 \text{ kg m}^{-3}$ and $p_{sat} = 2.3 \text{ kPa}$.

$$\tau_{\text{bubble}} \approx 0.092 d^{\text{max}} \quad (2.33)$$

The maximal radius of a bubble may also be estimated from the energy (E), absorbed in the system [39]:

$$R_{\text{max}} \sim \left(\frac{3 E}{4\pi p_w} \right)^{1/3} \quad (2.34)$$

where E is the absorbed energy by nanoparticle, and p_w is the ambient pressure. $E = \pi R^2 I_0 C_{\text{abs}} \tau_p$ is the total energy absorbed [39]. R is the nanoparticle radius, I_0 is the laser pulse intensity, C_{abs} is the absorption cross section of the nanoparticle, and τ_p is the pulse duration.

For example, 100fs pulse with $I_0 = 1.25 \frac{\text{TW}}{\text{cm}^2}$.

For a particle with $R=20\text{nm}$, $\lambda=800\text{nm}$, $C_{\text{abs}} \sim 10^{-2}$ [39]. Therefore, $E = 2.5 * 10^{-14}$.

$$R_{\text{max}} \sim 0.5 \mu\text{m}$$

$$\tau_{\text{bubble}} \approx 100\text{ns}$$

2.1.7 Surface Chemistry of Nanoparticles

When choosing NPs for biomedical applications that do not induce the body's immune response, it is critical to select a metal that is inert and biocompatible. The use of specific cell targeting strategies to deliver the NPs to the diseased cells and tissue is required in order to prevent damage to healthy cells. As such, it is also important to be able to chemically bind various molecules to the NP in order to functionalize it for targeting cancer cells. Gold NPs, in particular, allow facile biofunctionalization, thus making them promising for integration with cancer targeting vectors. The strong covalent bond between gold and sulfur provides a robust platform for linking between gold and sulfur-containing organic molecules [40-42]. Sulfhydryl (SH)

functional groups in thiols (RSH) have been widely used in site-specific bioconjugate labelling [43], since the strength of thiolate–gold (RS–Au) bond is comparable to that of gold–gold bond. Although gold is inert in its bulk form, its nanometer-scale ligand chemistry is well developed for biological and medical applications. Biocompatible metallic nanorods that are used for cancer treatment can be made to specifically target cancer cells by coating their surface with biological molecules (e.g. antibodies, aptamers, or peptides) that recognize tumor-associated structures [14,44-46]. Due to their small size, nanorods can effectively reach tumor cells by passing through the tumor's' leaky blood vessels. In that manner, they are able to reach a large number of cancer cell, resulting in an effective cancer treatment. Nanorods can be made small enough to allow cellular uptake, which in combination with cancer targeting vectors allows for a highly accurate cancer therapy.

2.1.8 Femtosecond Laser Pulses and Gold Nanorods for Cancer Treatment

A novel cancer treatment approach currently under investigation is the induction of tissue hyperthermia mediated via metallic nanoparticles (MNPs) irradiated with laser light. To date, nanoparticles and laser radiation have been used for the application of drug delivery, cell fusion, photodynamic therapy, and photothermal therapy. The application of lasers and nanoparticles for cancer therapy has been explored using continuous wave (CW) low-power laser radiation. Dickerson et al. [47] demonstrated a plasmonic photothermal therapy (PPTT) where laser light energy was absorbed by polyethylene glycol (PEG)-coated gold nanorods (Au-NRs) and converted into heat sufficient to induce cellular hyperthermia. Using a near infrared (NIR) laser operating at 800nm to irradiate the tissue for 10 min at 0.9–1.1 W/cm², they showed a decrease in size of squamous cell carcinoma xenografts in nu/nu mice. Huang et al. [48] targeted ENT cancer cells with anti-EGFR antibody conjugated Au nanorods. A CW Ti:Sapphire laser operating at 800 nm, was used for irradiating the Au nanorod containing cells. Under laser

radiation exposure of 4 min, they found that the cancer cells required half the laser energy (10 W/cm^2) to be photothermally damaged compared to a nonmalignant epithelial cell line (HaCat) which were damaged at 20 W/cm^2 . They concluded that this was due to the selective targeting of the over-expressed EGFR on the cancer cell surface by the anti-EGFR conjugated Au-NRs, while the non-malignant cells were not affected. O'Neal et al. [44] demonstrated a treatment of murine colon carcinoma (CT26.WT) tumors grown in immune-competent mice. PEG-coated nanoshells were intravenously injected to the mice and allowed to circulate for 6 hours. The tumors were irradiated with a diode laser beam (808 nm , 4 W/cm^2) for 3 min. All the treated tumors cleared, and the mice appeared healthy and tumor free for over 90 days after the treatment.

Several researchers have been investigating the use of pulsed lasers for cancer treatment. Pitsillides et al. [49] employed laser pulses and Au nanospheres for selective and highly localized photothermolysis of targeted lymphocytes cells. Lymphocytes were incubated with NPs conjugated to antibodies and then exposed to 20 nanosecond laser pulses (Q-switched frequency doubled Nd:YAG laser, $532/560 \text{ nm}$ wavelength). Cell death after irradiating with 100 laser pulses at an energy density of 0.5 J/cm^2 was demonstrated. Interestingly, adjacent cells, without nanoparticles, just a few micrometers away remained viable. Numerical heat transport simulations showed that at a fluence of 0.5 J/cm^2 , the peak temperature of the nanospheres, under a single pulse, exceeded 2000K . The cell death is attributed mainly to the cavitation damage induced by the micro-scale bubbles generated around the nanospheres. Using a single near-infrared and visible pulse of 10ns duration, Hleb et al. [50] induced intracellular photothermal microbubbles in C225-positive squamous carcinoma cells containing C225 tumor-specific monoclonal antibodies conjugated nanoparticles. The laser energy fluence threshold required for

bubble generation was 100-times less in cells containing nanoparticles. Cell damage had a mechanical origin and single cell selectivity. Disruption of the cellular membrane of epidermoid carcinoma and Burkitt lymphoma cells loaded with Anti-EGFR-coated gold nanospheres was realized by Minai et al [51], by employing 50fs laser pulses with 550nm central wavelength. The main advantages of their approach are low toxicity, high specificity, and high flexibility in the regulation of cell damage.

While previously reported works utilized nanoparticles and femtosecond laser pulses, translational issues remain. In order to have an effective cancer treatment with this methodology, it is crucial to be able to deliver the laser pulses to the treatment site, especially for non-superficial cancers, while keeping the energy fluence below the damage threshold of the healthy cells. As such, a delicate balance must be realized between the laser-tissue interaction parameters: energy fluence, and penetration depth of the optical pulse, pulse train duration, and exposure/time. Notably, once the laser pulses are delivered to the tumor site, it is crucial that the laser intensity throughout the depth of the tumor is maintained above a certain threshold intensity to achieve an effective treatment throughout the entire cancerous area. For ultrashort laser pulses, linear/non-linear absorption and scattering limit laser power that can be delivered, and thus, hinders treatment of buried tumors. A central wavelength around 800nm is critical, since at this wavelength tissue have low absorption, allowing the laser light to reach deep inside the tissue with sufficient laser intensity for inducing an effective treatment.

When sub-wavelength metallic nanoparticles are illuminated with laser light at their surface plasmon resonance (coherent oscillation of the free electrons on the surface of the particle), localized surface plasmon (LSPRs) can be generated. The electrons oscillate on the surface of the nanoparticles in response to the incident photons, giving rise to a net charge difference at the

nanoparticle's boundary. This charge accumulation results in electron confinement that leads to the enhancement of electromagnetic fields at the metallic surface. The rapid oscillation of the electrons in the metallic nanoparticles results in electron-electron and electron-lattice collisions, which in turn results in rapid temperature rise of the nanoparticles.

The LSPR wavelength (λ_{max}) and extinction cross-section of metallic nanoparticles are size and shape dependent [14-16]. These parameters are highly sensitive to the chemical capping agents and surrounding dielectric environment (i.e. refractive index) [14-16]. Due to the LSPR oscillation, light absorption is enhanced [14-16]. When delivering laser light to tumors, one requires the energy to be absorbed preferentially by the nanoparticles and not by the tissue. The absorption of the laser electric field is enhanced when there are nanoparticles present in the cells, especially when excited at the LSPR. The tissue transparency window is at the NIR wavelengths; therefore higher penetration depth and minimal absorption by the tissue can be realized. Of particular interest are rod-like shaped nanoparticles (nanorods), since they can be made small (sub-100nm) to penetrate biological cells while maintaining a LSPR at the NIR region. LSPR intensity and wavelength depend on the intrinsic properties of the nanoparticle such as the metal type, particle size, shape, and structure, as theoretically described by Mie theory [17]. For nanorods (NR), the LSPR is split into two frequencies: a strong resonance corresponding to the electron oscillations along the long axis (longitudinal band), and a weak resonance corresponding to the short axis (transverse band). If the longitudinal resonance is in the NIR region, then the transverse resonance lies in the visible region. Electric field enhancement calculations (see Appendix A) were performed on Au-NR with size of 11nm×43nm, and are depicted in Figure 2.19 for three incident fs laser pulse polarizations at central wavelength of 800nm.

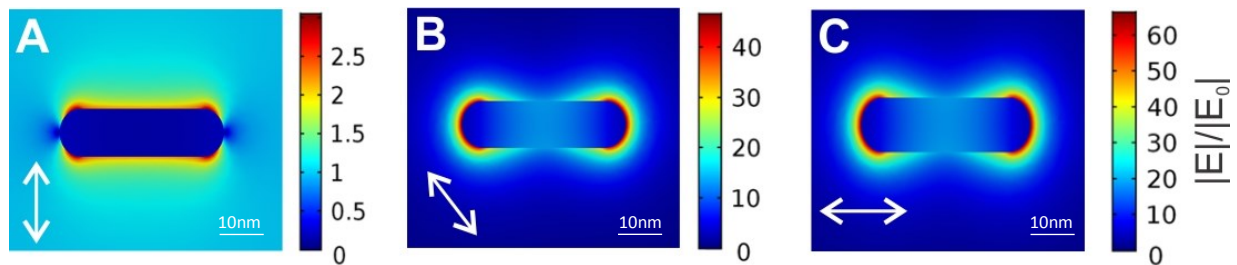


Figure 2.19: The near-field enhancement for A. transverse, B. diagonal, and C. longitudinal polarizations. The color legend on the right shows the magnitude of the field enhancement ($|E|/|E_0|$). The arrow points at the direction of the polarization of the incident electric field E_0 .

The weakest electric field enhancement of 3 occurs when transverse incident light polarization interacts with the Au-NR (figure 2.19A). For diagonal polarization, the electric field enhancement is at 46 (Figure 2.19B). The strongest electric field enhancement of 66.5 occurs at longitudinal incident light polarization (Figure 2.19C), which corresponds to the LSPR of the Au-NR. Clearly, for randomly oriented Au-NRs, it is ideal to use laser pulses having circular polarization.

The dissipation of LSPR excitation into heat takes place via a series of non-radiative processes (process is discussed in section 2.5 Nonradiative Properties of Gold). Using two-temperature model calculation (see Appendix A) of Au-NR electron temperature, Au-NR lattice temperature and its surrounding water temperature due to irradiation with a single $1.45\text{TW}/\text{cm}^2$ laser pulse is depicted in Figure 2.20. The temperature of the electron reaches $\sim 150,000\text{K}$ within 190fs, while the lattice temperature at that time is only $\sim 370\text{K}$ and the water temperature is 273K. The lattice reaches its peak temperature of 46,000K after 200ps, and the water reaches its peak temperature of 19,000K after 360ps.

The localized and intense increase in temperature of NPs due to irradiation with laser light is important for inducing damage to targeted cells in the application of this methodology in cancer treatment. It is also crucial to consider which light source to use: CW or ultrashort laser pulse. To date, most cancer treatment application that use this technology employ CW lasers. However, employing CW laser for treatment requires depositing significant amounts of energy onto the tissue and high concentration of NPs in order to increase the temperature of the NPs sufficiently to damage the cancer cells. Nonetheless, some of the energy is inadvertently absorbed by the healthy tissue and can result in unwanted cellular damage. Here, cell death occurs due to gradual increase in temperature of the cells that result in protein denaturation, coagulation and cell membrane destruction [35]. The destruction of cancer cells using CW lasers and NPs requires that high concentration of particles reach critical organelles inside the cells, in order to induce sufficient temperature increase that results in cellular damage. Therefore, treatment of cancer using hyperthermia induced by NPs is not easily reproducible in in vivo translational applications.

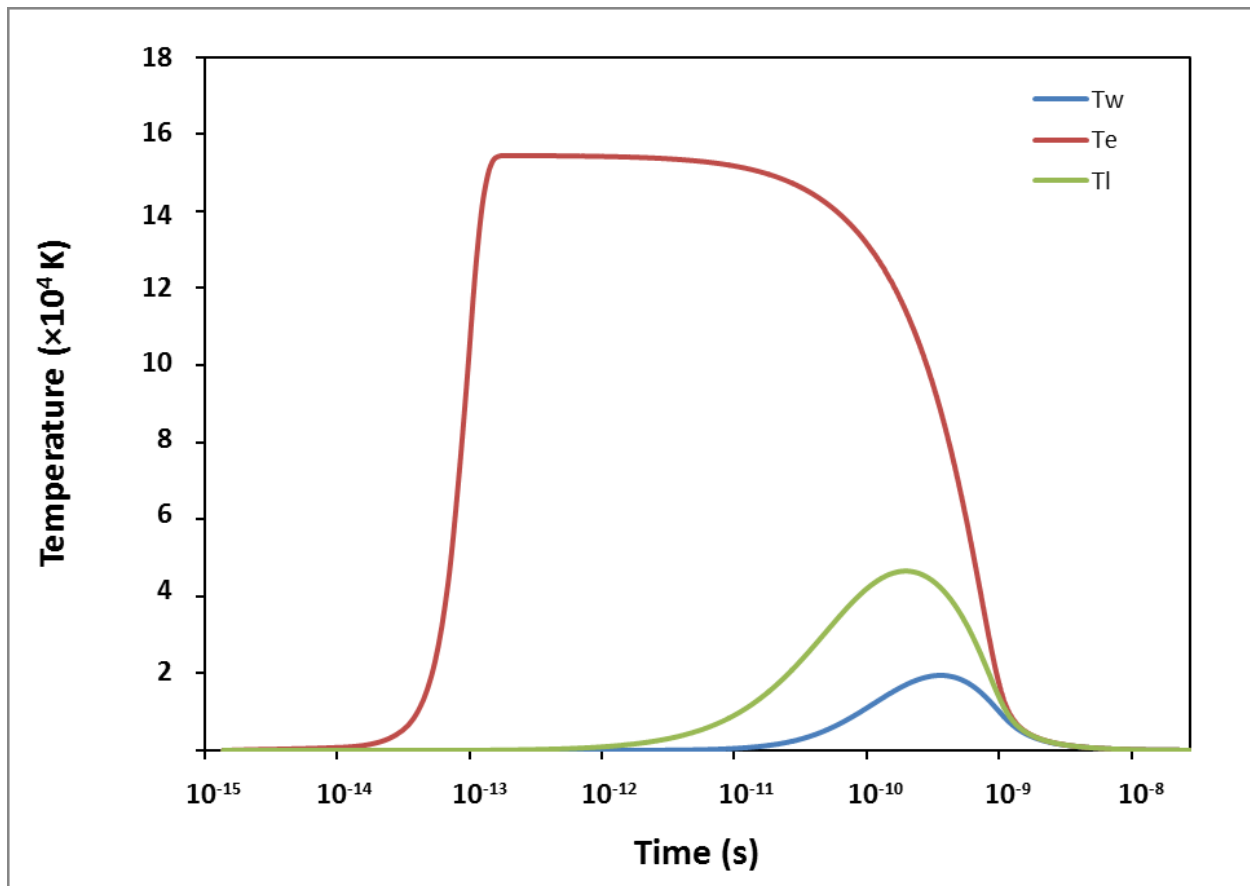


Figure 2.20: Time-dependent temperature evolution of electrons, T_e , lattice T_l and water T_w , at the $11 \text{ nm} \times 43 \text{ nm}$ AuNR-water interface, for a longitudinal incident 55 fs , $\lambda=800 \text{ nm}$ laser pulse of at a fluence of 40 mJ/cm^2 .

A more effective and translational approach for cancer therapy on a nanometer scale would be to take advantage of the high peak power and short pulse duration of femtosecond laser pulses to induce rapid temperature increase of the NPs. Such excitation process would result in vaporization and cavitation bubble formation of the material situated close to the NPs [35]. This, in turn, disrupts the physical structure of the cancer cells and leads to cell death through necrosis or apoptosis. By selectively targeting NPs to enter or attach to the cellular membrane of cancer cells, and reducing the pulse irradiance below the ionization threshold of the biomaterial and its

surroundings, a treatment that is localized to the cancer cells alone can be achieved. When metallic NPs interact with intense ultrashort laser pulses, the material that surrounds the NPs is affected by two main processes: (1) within a few picoseconds, the temperature of the environment rises due to heat diffusion from the high temperature NPs, and (2) acoustic shockwaves are formed as a result of thermal expansion and vaporization of water around the NPs. While electric field enhancement around the NPs would contribute to the generation of free electrons close to the surface of the NPs, via nonlinear processes (i.e. multiphoton absorption, avalanche breakdown, and tunnel ionization effect), these high-field interactions take place within a very small volume and are insignificant to the destruction of the cell. Unlike CW laser excitation, a key advantage of using high intensity ultrashort laser pulses is that the NPs can be heated to extremely high temperatures (e.g. beyond melting temperatures) using low-energy pulses.

Ultrashort laser pulses have been employed for the study and manipulation of cells and tissue. In particular, femtosecond laser pulses have become an invaluable tool for manipulation of structures as small as a few hundred nanometers in a non-invasive fashion. To date, this technology has been applied for precise neuronal attachment [3], and cell-cell attachment [1,2], cell nanosurgery [4], cell isolation [4], and embryo transfection [5,6].

2.2 Laser-Tissue Interaction - Background and Chapter Objectives

In recent years, the use of pulsed lasers to manipulate biological materials has increased, as such, understanding the laser-tissue interaction process is important. Tissue ablation and manipulation can take place through either linear and non-linear absorption. Understanding the conditions required for these two types of absorption processes, and its results is critical for better

development of biomedical tools. Our understanding of laser pulse tissue interaction is based on a combination of experimental and modeling work that describes the ionized electron density [7,52]. From the ion density, the temperature change in the focal volume, shockwave expansion and cavitation bubble formation in water can be estimated. The ultimate goal has been to try to match experimental work with theory.

Laser pulse duration is a parameter that influences the laser tissue interaction process. For femtosecond laser pulses, in particular, the time scale of the pulse is significantly shorter than the shockwave and cavitation bubble events taking place [7,52,53]. Due to the complexities underlying laser pulse ablation, our understanding of its mechanism and influence on biological materials, are currently incomplete, and laser-tissue interaction is still a highly active area of research. In the second part of chapter 2, an overview of the currently accepted understanding and physics in the field is provided. This work is based on a combination of theoretical simulations and experimental work. The second part of the thesis (chapters 4-5) focuses on the interaction of femtosecond laser pulses directly with tissue, and thus, it is important to provide the necessary knowledge required to understand the reasoning behind using such short pulses. Additionally, at the end of the chapter a summary of the cell membrane structure and the cell line used in the second portion of the thesis is provided, in order to understand the process that takes place during femtosecond laser-induced cell-cell attachment (namely cell membrane hemifusion).

Biological material is more transparent to near-infrared (NIR) wavelengths (e.g. 800 nm), compared to visible wavelengths [54,55]. At this wavelength the femtosecond laser pulses can penetrate water and blood with absorption coefficients of 10^{-2} cm^{-1} [56, 57] and 1 cm^{-1} [57], respectively. That is, for example at 1cm, for water 99% of the light is transmitted and for blood

37% of the light is transmitted. When working with high numerical aperture (NA) lenses on single cells, 800nm light passes through water mainly, and thus, only interact at its focused locations without disrupting cellular material above or below the laser focal spot. The biological material will be altered only at the femtosecond laser pulse focus, and will result in either dissection, excision or permeabilization, through a linear or nonlinear process that is described below. When laser irradiation is delivered onto biological material, the material absorbs the irradiation either through single photon absorption or nonlinear absorption, depending on the irradiation wavelength, intensity and the laser pulse duration [58].

Single photon absorption (i.e. linear absorption) takes place when an electron absorbs a single photon to make a transition to a higher energy level or becomes free. This process is depicted in Figure 2.21 where the energy of the absorbed photon is equal to or higher than the energy of the final transition state.

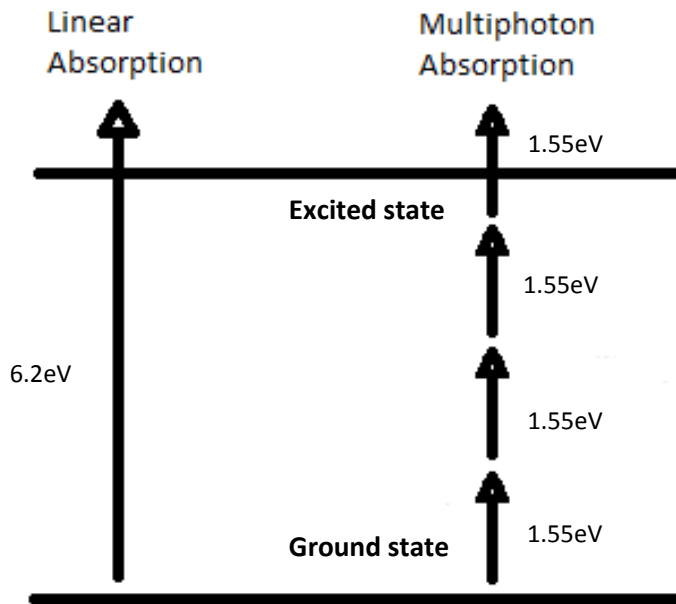


Figure 2.21: Schematic diagram of single photon absorption vs. multiphoton absorption. An electron is excited from its ground state to an excited state with either four 1.55eV photons (multiphoton absorption) or a single 6.2eV photon (single photon absorption).

If the energy of the laser photon is much less than the energy of the final transition state, linear absorption cannot occur. However, when a laser pulse duration is very short, the peak power of the pulse can be very high to initiate nonlinear absorption process (i.e. an electron coherently absorbs multiple photons to make a transition to a final state). This multiphoton absorption process occurs when the intensity of the short pulse reaches a certain threshold. Here, material ablation occurs via ionization and chemical decomposition (i.e. bond-breaking or dissection) of the biological material [7]. Figure 2.21 contrasts the multiphoton absorption and single photon absorption processes. In this figure, it is assumed that four photons with a photon energy of 1.55

eV (800 nm) are required to promote an electron from the lower energy state to the upper energy state for multiphoton absorption. While for single photon absorption, a single photon with an energy equal to the difference in the energy states, 6.2 eV (200 nm light) would be required to excite the electron.

The benefit of femtosecond laser pulses over longer pulse durations is due to the lower threshold energy required to induce tissue-ablation [7] and the ability to localize tissue-damage to the cellular level [7]. Since lower threshold is required to elicit tissue damage, a lower laser pulse energy is required, which means that less energy is available to be funneled into adverse side effects, such as shockwave and cavitation bubble formation, which are known to increase the spatial extent of tissue damage [7].

2.2.1 Multiphoton Ionization

Multiphoton absorption is a non-linear process that is the initiating process of ablation of biological material using ultrashort high intensity laser pulses. Simultaneous absorption of ‘ k ’ photons excites a valence electron to the conduction band (see Figure 2.21), leading to an ionized electron [58]. In order to determine if the laser-tissue interaction process takes place mainly through multiphoton absorption and ionization, the Keldysh parameter γ , is calculated [58].

$$\gamma = \frac{\omega}{e} \sqrt{\frac{cm_e \varepsilon_0 n \Delta}{I}} \quad (2.35)$$

where ω , e , c , m_e , ε_0 , n , Δ and I are the frequency of light, electron charge, speed of light, effective electron mass, permittivity of free space, index of refraction (1.33 for water), ionization potential of water (6.5 eV [59]) and the laser peak intensity, respectively. When $\gamma > 1$, the laser-tissue interaction process is primarily governed by multiphoton absorption and ionization, whereas, when $\gamma < 1$, laser-tissue interaction is governed by tunnel ionization [60]. Throughout

this thesis, γ is calculated to be greater than 1 based on the pulse energy and peak intensity used for each of the studies in chapters 2, 4-5.

In most computer modeling of biological tissue, water has been the model used to understand the laser-tissue interaction process with biological material [7]. Experimental work [59] suggests that the ionization potential of water is 6.5eV. For femtosecond laser pulse with a wavelength centered at 800 nm (1.55 eV), the ionization of a single electron requires the simultaneous absorption of 5 photons.

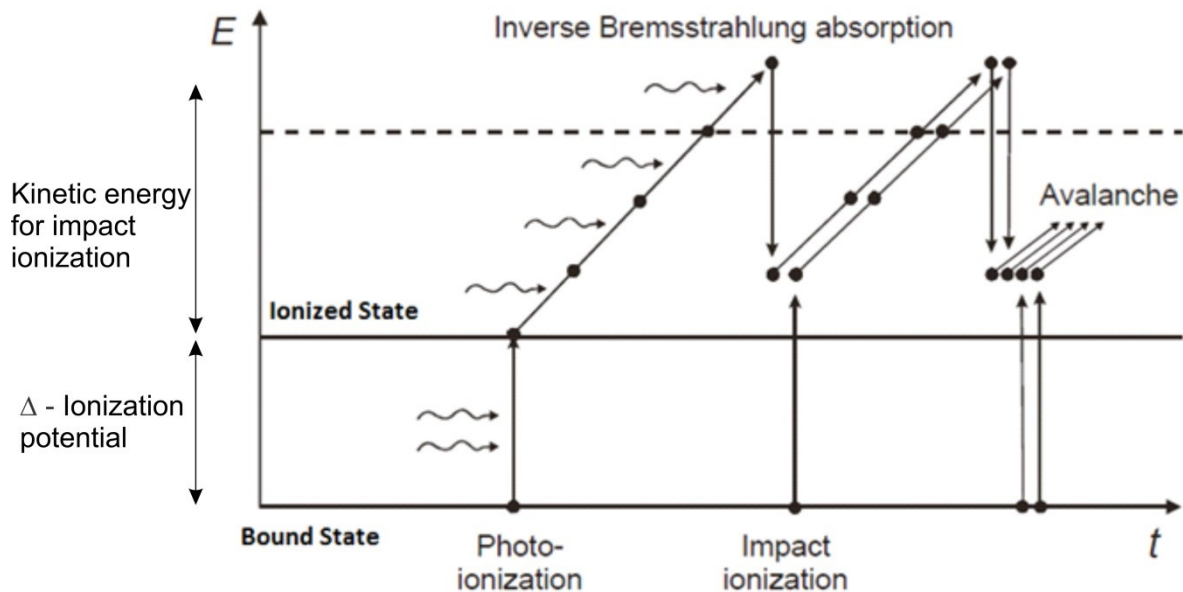


Figure 2.22: Schematic diagram of photo-ionization and impact ionization [7]. Photo-ionization of ‘lucky’ electron leads to inverse bremsstrahlung absorption of incoming photons, which leads to impact and avalanche ionization.

Once a single electron has reached an excited state, the ‘lucky electron’ provides the necessary initial seed electron for the generation of plasma (high density electron gas) mediated ablation process. As seen in figure 2.22, once the ‘lucky electron’ is ionized, it begins to absorb single

laser photons (through inverse Bremsstrahlung absorption, a process where an electron absorbs the energy of an incident photon) within the duration of the laser pulse [7,60]. Therefore, this seed electron increases its energy until it eventually absorbs enough energy to impact ionize an additional electron, promoting a new seed electron to an ionized state [7]. The new seed electrons continue to absorb single laser photons and participate in impact ionization after achieving critical energy. The collective process of energy gain and electron impact increases the electron density, and is defined as ‘avalanche/cascade ionization’. When a critical ionized electron density N_{crit} is reached, optical breakdown of the material starts to take place [53,60].

$$N_{crit} = \frac{\omega^2 m_e \epsilon_0}{e^2} \quad (2.36)$$

where ω , e , m_e , and ϵ_0 represent the frequency of light, electron charge, electron mass and permittivity of free space, respectively. The critical electron density when the plasma become strongly reflective for laser wavelength of 800nm is $N_{crit}=10^{21} \text{ cm}^{-3}$. The advantage of using ultrashort femtosecond laser pulses to longer pulse durations is that plasma mediated ablation is process that is easily reproducible and efficient. For longer pulse duration plasma mediated ablation process depends on production of seed electron due to thermionic emission of impurity electrons [53,60]. This dependence on impurity density makes this process statistically irreproducible for long laser pulse durations.

2.2.2 Laser Pulse Ablation Profile

A key advantage of using femtosecond laser pulses than longer pulse duration for biological tissue processing is its extremely small spatial extent of damage. Some examples include: subcellular dissection using femtosecond laser pulses [61], neuronal dissection [62], intra-tissue nanoprocessing in plans [63], optical-poration of single cells and embryos [5,6], cell-cell nanosurgical attachment [1], neuronal attachment [3], and many more.

The sub-diffraction limit spatial extent of the ablation originates from the nonlinear multiphoton absorption process that takes place within an interaction volume smaller than the focal spot of the laser pulse. The spatial resolution of the ablated region is dictated by the electron density profile and not by the irradiance profile [7]. Simulations of femtosecond laser pulse interaction with water show that the electron density profile is smaller than the irradiance profile by a factor of \sqrt{k} [7], where k is the number photons required to ionize the material. The diffraction limited spot size of radius r and the depth of focus, are:

$$r = \frac{1.22\lambda}{NA} \quad \text{and} \quad z = 2 \left(\frac{\pi w_0^2}{\lambda} \right), \text{ respectively} \quad (2.37)$$

An example relevant to the laser parameters used in this thesis is $NA=1$, $\lambda=800\text{nm}$, and $w_0=488\text{nm}$ are the numerical aperture, wavelength, and beam waist, respectively. In this case, the laser irradiance profile are: $r=976\text{nm}$, and $z=1870\text{nm}$. Assuming a laser having a wavelength of 800nm (1.55eV) interacting with water (ionization potential of 6.5eV), the electron density profile is smaller by a factor of $\sqrt{5}$, which results in ablation spatial extent of $r=436\text{nm}$ and $z=935\text{nm}$.

The factors that determine the extent of the ablated volume, and in most cases extend beyond the sub-diffraction dimensions mentioned above, are the shockwave and cavitation bubble formation. In the case of longer pulse durations, such as high energy nanosecond laser pulses, the process that initiates material ablation is due to heating and melting; therefore, the ablation spatial extent is not reduced by \sqrt{k} . Since the energy per pulse required to initiate material ablation with femtosecond pulses is much lower than for nanosecond pulses, the excess energy of longer pulse is ultimately funneled into shockwave and cavitation bubble formation; thus,

extending the spatial extent of material ablation beyond the diffraction limited laser irradiance profile [64,65].

2.2.3 Laser Pulse Induced Heat Stress

The estimation of temperature rise due to irradiation with femtosecond laser pulse is an active field of research. It has been shown that the temperature increase during material ablation due to femtosecond laser pulse is significantly smaller compared to nanosecond laser pulses [7]. Several groups have attempted to calculate the temperature increase by calculating the thermal stress due to ablation by studying the ablated solids and tissue using Scanning Electron Microscopy (SEM) [66,67]. These examinations revealed smooth crater walls, while noting the absence of cracks and surface melting [66]. These studies concluded that shortening the pulse duration results in smaller heating volume and that the threshold energy needed for ablation decreases as well. A direct temperature measurement was performed using an infrared camera [67], and it was found that the front surface of ablated dentin tissue irradiated with femtosecond laser pulses (350 femtoseconds at a repetition rate of 10 Hz) was 3.9 °C. Multiple reports [68-72] refer to femtosecond ablation of material as non-thermal ablation process. In these publications the authors refer to the structural change in material due to chemical bond-breaking as a result of electron impact or dissection through cavitation bubble formation. Vogel *et al.* [7] provided a relation to estimate the temperature rise due to application of a single 100 femtosecond laser pulse in water. Since, the time scale of energy transfer between an electron and its ion is on the order of 1 to 100 picoseconds [7,73], which is much slower than the laser excitation time, the temperature rise of water due to femtosecond laser pulse irradiation can be estimated from [7]:

$$\Delta T = \frac{\epsilon}{\rho_0 C_p} \quad (2.38)$$

where ϵ , ρ , and C_p are the volumetric energy density, the density of water (1 g/cm³) and the specific heat capacity of water (4.184 J/K·g), respectively. Equation 2.38 describes the temperature rise within the focal volume. The volumetric energy density is calculated using equation 2.39 [7]

$$\epsilon = \rho_{max} \left(\frac{9}{4} \right) \Delta \quad (2.39)$$

where Δ is the effective ionization potential, and ρ_{max} is the maximum ionized electron density. For example, for a single 100 femtosecond laser pulse with intensity of 1.7×10^{12} W/cm², the volumetric energy density is 0.02 J cm⁻³ (From vogel et al. [7], the irradiance threshold for 100fs pulse is $I_R = 8.5 \times 10^{12}$ Wcm⁻². Therefore, $I/I_R = 0.2$ and $\rho_{max} = 10^{16}$, which results in $\epsilon = 0.02 \frac{J}{cm^3}$). Thus, the temperature rise due to a single pulse is calculated $\Delta T = 0.01$ K above room temperature [7]. When successive femtosecond laser pulses interact with a material it is expected that the water temperature increase additively due to each laser pulse; however, each pulse in the pulse train interacts with the material after the electron-ion energy transfer time; requiring a more complex form of temperature evolution equations. Vogel et al. [7] calculated that for tightly focused irradiation of 100 femtosecond laser pulses with 80-MHz repetition rate, the temperature rise of water plateaus after about 10 μ s and reaches a maximum temperature increase of $\Delta T = 2$ K. This implies that only a moderate heat accumulation occurs during plasma-mediated cell surgery.

The spatial extent of heat is determined by the thermal diffusion length L_{diff} in the material, which is given by,

$$L_{diff} = \sqrt{D\tau} \quad (2.40)$$

where τ and D , are the laser pulse duration and heat diffusion coefficient, respectively.

For example, a 100-femtosecond laser pulse irradiation of water with heat diffusion coefficient $D = 1.38 \times 10^{-7} \text{ m}^2\text{s}^{-1}$, has a thermal diffusion length of 0.12nm. Clearly, for femtosecond laser pulse the combination of the multiphoton absorption process, the lower threshold energy required for optical breakdown, the lower temperature rise and the short thermal diffusion compared to longer pulse durations are the main factors that make the femtosecond laser an attractive tool for tissue ablation and manipulation.

2.2.4 Shockwave and Cavitation Bubble Formation

Shockwave and cavitation bubble are the two most important effects that take place during femtosecond laser ablation of material. Shockwaves that are induced due to laser originate from the diffusion of high density ionized electrons outside of the focal volume, resulting in plasma expansion [53]. Shockwaves first expand with supersonic velocity, and then slow down to the speed of sound in the medium ($\sim 1500 \text{ m/s}$ for water [53]). If the energy of the ionized electrons is sufficiently high, ions could follow escaping electrons, which may result in movement of material [53]. The dynamics of shockwave formation and propagation due to nanosecond, picosecond and femtosecond laser pulses in corneal tissue and in water have been previously studied [64,65,69,74,75]. The strength and extent of the shockwave and cavitation bubble depends on the deposited laser energy, where any excess of energy deposition beyond the threshold of material ionization funnels into shockwave propagation and cavitation formation [7,65]. Vogel *et al.* [65] compared the shockwave dynamics of picosecond and nanosecond laser pulses and revealed that the initial shock pressure for 50 μJ picosecond pulse was 17 kbar, while the pressure for 1 mJ nanosecond laser pulse was 21 kbar. Additionally, the pressure decay due to picosecond pulse was much faster compared to nanosecond pulse. The authors also found that for picosecond laser pulse, a final pressure of 1 kbar was found at a propagation distance of 50 μm , in comparison to 200 μm for nanosecond laser pulses. Therefore, they concluded that by

using shorter laser pulses for photo-disruption would result in smaller and more accurate ablation.

Shockwave experiments have been performed using femtosecond laser pulses [7,74]. Flashed photography was used to measure the bubble radius and estimate the bubble propagation speed and pressure. Theoretical estimates of the pressure at the plasma rim have been reported for 100 femtosecond laser pulses focused onto water with laser energy 10 times greater than the optical breakdown threshold [74]. The plasma expansion was observed 30 ps after breakdown and continued for 200 ps [74]. Calculations have shown that the pressure at the plasma rim for a deposited volumetric energy density of 1 Jcm^{-3} is 420 bar (42 MPa) [7]. This value is a few orders of magnitude lower compared to the pressure generated by picosecond and nanosecond laser pulses. It should be noted that, in order to obtain and analyze observational data, these experiments were performed using pulse energies higher than the material ablation threshold. However, the insight provided from these results is that the pressure and the spatial size of shockwave due to laser ablation decreases with shorter pulse duration. Since non-linear absorption takes effect due to irradiation with femtosecond laser pulses, the amount of energy per pulse require to elicit material ablation decreases, thus, less energy is available to be funneled to shockwave formation, resulting in lower plasma rim pressure. The lower pressure inherently results in faster decay time which inevitably decreases the spatial extent of the tissue disruption. An acoustic pressure wave follows the shockwave and is characterized by the formation of a cavitation bubble. The cavitation bubble formation takes place about 10ns following laser irradiation, and continues to expand for microseconds to seconds, depending on the energy deposited by the laser irradiation [74]. Due to the formation of gas and vapor during ionization of the media, the gas expands from the focal volume of the laser irradiation location outwards to the

surrounding tissue or media [53]. The maximal radius of cavitation due to a single 100 femtosecond laser pulse that is focused onto water with NA=1.3 was found to be 200nm [7]. Such small radius is attributed to the low energy deposition in the media required for plasma mediated ablation, and consequently, low energy conversion into cavitation bubble. Successive femtosecond laser pulse excitation results in larger cavitation bubbles [7]. For example, plasma mediated tissue ablation due to 100 femtosecond laser pulses with a repetition rate of 80MHz, results in excitation of the cavitation bubble before its collapse, depositing more and more energy into the bubble. Each bubble begins to expand after ~10ns, while each laser pulse arrives every 12.5 nanoseconds. Therefore, after 12.5 nanoseconds, the bubble continues to expand and accumulated additional energy for increased expansion, increasing its overall radius. With careful selection of the number of laser pulses, it is possible to control the maximum radius of cavitation bubble [52]. Once a bubble is formed, it expands outwards with pressures ranging in the MPas [7]; thus inducing stress on the surrounding media, and resulting in disruption of surrounding tissue [65]. For short pulse laser excitations, the spatial extent of tissue damage is determined by the spatial extent of the maximum cavitation bubble diameter [4]. The mechanical strength attributed to biological tissue, compared to pure water, can slow down the expanding cavitation bubble. The ‘resistance’, generally, results in smaller extent of damage in tissue compared to pure water [64,65].

2.2.5 Different Femtosecond Laser Pulse Repetition Rates Effects on Laser Pulse Ablation

Femtosecond laser pulses that are generated at a high repetition rate generally contain small amount of energy per pulse (e.g. in femtosecond laser oscillators, the energy per pulse for femtosecond laser pulses with repetition rate of 1-100 MHz ranges between 1nJ – 100nJ); whereas, low repetition rates pulses contain higher energy per pulse (e.g. energy per pulse for femtosecond laser pulses with repetition rate of 1-5KHz ranges between 100μJ – 5mJ). Such

large difference in energies per pulse lead to different mechanism of femtosecond laser pulse tissue ablation [7]. For high repetition rate (a few MHz) laser pulses, the laser intensity is below the threshold for optical breakdown. When absorbed by biological material, each pulse produces electron density that is below the critical density of material breakdown, as such, successive pulses lead to the formation of low density plasma [7]. For this case, it is understood that ablation results from free electron bond breaking, which leads to chemical decomposition of the biological material [7]. For low repetition rate pulses, with intensity higher than the threshold required to elicit ablation, high density plasma and cavitation bubble is formed. It is suggested that the fast expanding, and high-pressure gas bubble formed is resulting in biological material dissection [7].

2.2.6 Critical Power for Self-Focusing and Plasma Formation

Due to the high peak power of femtosecond laser pulses, unwanted non-linear laser interaction process can take place. For example, self-focusing, a phenomenon that causes the laser beam diameter to self-focus as it propagates through the medium. Self-focusing can take place due to the dependence of the index of refraction on the laser pulse intensity [76,77]. The index of refraction dependence on laser intensity is described as:

$$n(\omega) = n_1(\omega) + n_2(\omega)I \quad (2.41)$$

where $n(\omega)$, $n_1(\omega)$, $n_2(\omega)$ and I are the total refractive index, the index of refraction in the absence of self-focusing, the nonlinear index and the laser peak intensity, respectively. Once the laser peak intensity is sufficiently high, the contribution of n_2I increases the total index of refraction. An issue that arises due to self-focusing during femtosecond laser pulse ablation process, is that the location and size of ionized electron density and temperature rise is difficult

to define and predict. Therefore, to obtain consistent and reproducible results, it is important to avoid nonlinear self-focusing effects.

One method to avoid self-focusing is by using high NA microscope objectives, such as $NA \geq 0.9$.

As seen from eq 2.37, high NA microscope objectives produce smaller laser focal spot $r \propto \frac{1}{NA}$.

As such, using high NA objective, a certain peak laser intensity can be achieved with lower laser pulse peak power compared to using lower NA objective. For example, consider NA values of 0.5 and 1. The calculated diffraction limited spot sizes for 800nm laser pulse is calculated 1.95 μ m and 976nm, respectively. In order to achieve a peak intensity of 10^{12} W/cm², the peak power required is 30kW/pulse and 7.5kW/pulse, respectively. Since the intensity for self-focusing depends on peak power and critical peak power (see equation 2.42), high peak powers increase the likelihood of nonlinear self-focusing to take place [60,78]. The self-focusing intensity, and critical peak power for self-focusing are

$$I_{sf} = \frac{I}{1 - \frac{P}{P_{crit}}} \text{ and } P_{crit} = \frac{3.77\lambda^2}{8n_1n_2\pi} \quad (2.42)$$

where I , P , λ , n_1 and n_2 are the laser peak intensity, laser peak power, wavelength, linear and nonlinear refractive index, respectively. Hence, being able to use pulses with lower peak power is critical to avoid entering the regime of nonlinear self-focusing effects.

Numerical simulation show that plasmas formed with low NA objective lens (0.5 and 0.6 NA) are highly asymmetric [78]. High density plasma is formed before the predicted focal spot, with high density region surrounded by a lower density area [78]. The generation of plasma before the desired focal spot may distort the propagating pulse and cause a phenomena called plasma defocusing [78]. When using high NAs, plasma defocusing is weaker, and is accompanied by the formation of smaller and more symmetric plasmas.

In some applications, laser machining at low NA is necessary to results in large volume of material removed per pulse. Recent techniques to avoid nonlinear self-focusing while using low NAs include pulse shaping of femtosecond laser pulses [79], and the use of dual-beams [80].

2.2.7 Cellular Membrane

The cellular membrane is made of a phospholipid bilayer, which surrounds the cytoplasm of living cells, thereby holding the contents of the cell and physically separating the intracellular components from the extracellular environment [81]. The phospholipids make out most of the membrane and are characterized by having a hydrophilic end and hydrophobic end (see illustration in figure 2.23). The hydrophilic ends (heads) naturally align to face aqueous media, while the hydrophobic tails face away from the aqueous media. The membrane serves as the base for attachment for the cytoskeleton, and it helps support the cell to maintain its structure and shape. The cell membrane is primarily composed of proteins and lipids [81]. The lipids give the membrane its flexibility, while the proteins maintain and monitor the cellular chemistry, and assist with transfer of molecule across the membrane. Generally, the cellular membrane contains two types associated proteins: peripheral membrane proteins and integral proteins. Peripheral proteins are exterior to the membrane and interact with other proteins. Integral proteins pass through the membrane, where part of these transmembrane proteins are exposed on both sides of the membrane. Cell membrane proteins have different functions: structural proteins, receptor proteins, transport proteins, and glycoproteins. Receptor proteins communicate with the external environment, by using hormones, neuro-transmitters, and other signaling molecules. Transport proteins, transport molecules across the cell membrane. Glycoproteins, assist with cell-cell communications and molecular transport across the membrane. The cellular membrane is selectively permeable to material and acts as a “gateway” into and out of the cell [81]. It

regulates what material can enter and exit the cells, thus facilitating transport of substances essential for the cell's survival. Transport of material can be either passive, where the cell does not have to use-up energy for transport, or active, where the cell is required to spend energy for transport of material [81]. The cellular membrane maintains a membrane potential, allowing transport of materials with specific charges, thus acting as a filter. Physically, the cell membrane determines the shape of the cells by anchoring the cellular cytoskeleton [81]. It is also responsible for attachment of the cell to neighboring cells and to the extracellular matrix, thereby forming groups of cells which, in turn, form tissue and organs [81]. The cell membrane binds cellular structures such as the plasma (not to be confused with the ionized matter produced by the fs laser pulse) membrane proteins, lipids, carbohydrates, and complex structures such as cilia [81]. Membrane does not only exist on the exterior part of the cell, but also on cellular organelles such as the nucleus, endoplasmic reticulum, vacuoles, lysosomes, and the Golgi apparatus [81].

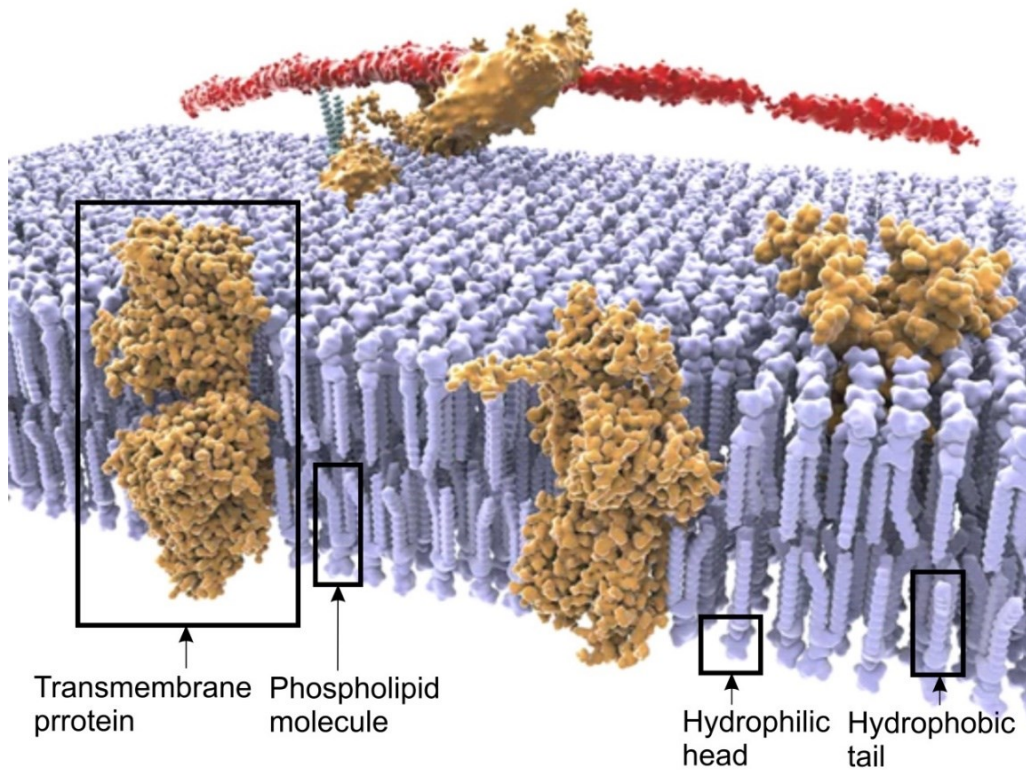


Figure 2.23: Illustration of cell membrane. A cutaway side view of the human cell membrane. Transmembrane proteins, phospholipid molecule, hydrophilic head and hydrophobic tail are marked. Figure taken from Alfred Pasieka/Science Photo Library.

2.2.8 Cellular Fusion and Hemifusion

The concept that cells are the building blocks of tissues in plants was proposed in 1838 by Schleiden [82], and in living organisms in 1839 by Schwann [82]. From these discoveries came the cell theory: cells are integral units of life. An extension of the theory explains how cells arise and how they change over time: cell reproduction, proliferation, differentiation and the development and maintenance of normal tissues. Schwann observed that when cells of the superficial dorsal muscle of pig embryos come in contact with each other, the walls of the cells

coalesce and blend, while the nuclei do not coalesce [83]. A substantial work by Schwann was microscopic observations of fusion of animal muscle, nerve and bone tissues.

Recent studies have shown that fusion of cells of different types does indeed occur. Heterokaryons cells were created by using the Sendai virus to induce fusion of HeLa cells and Ehrlich ascites tumor cells. These cells are formed by fusion, while the nuclei from each fusion partner remained separate and stable over time [85]. Synkaryons are cells that are formed by fusion and contain a single nucleus. A single nucleus requires nuclear fusion, followed by sorting and selective loss of chromosomes, while the cell remains viable. A single nucleus in Synkaryons can also be created by shedding one intact nucleus. Heterokaryon can serve as an intermediate step in the generation of Synkaryons [86]. In 1960, Barski *et al.* developed a cell culture system in which cells of two distinct lines were fused. The hybrid cells initially contained nuclei from both cell lines, but three months later, they formed a single nucleus with chromosomes from each fusion partner [87].

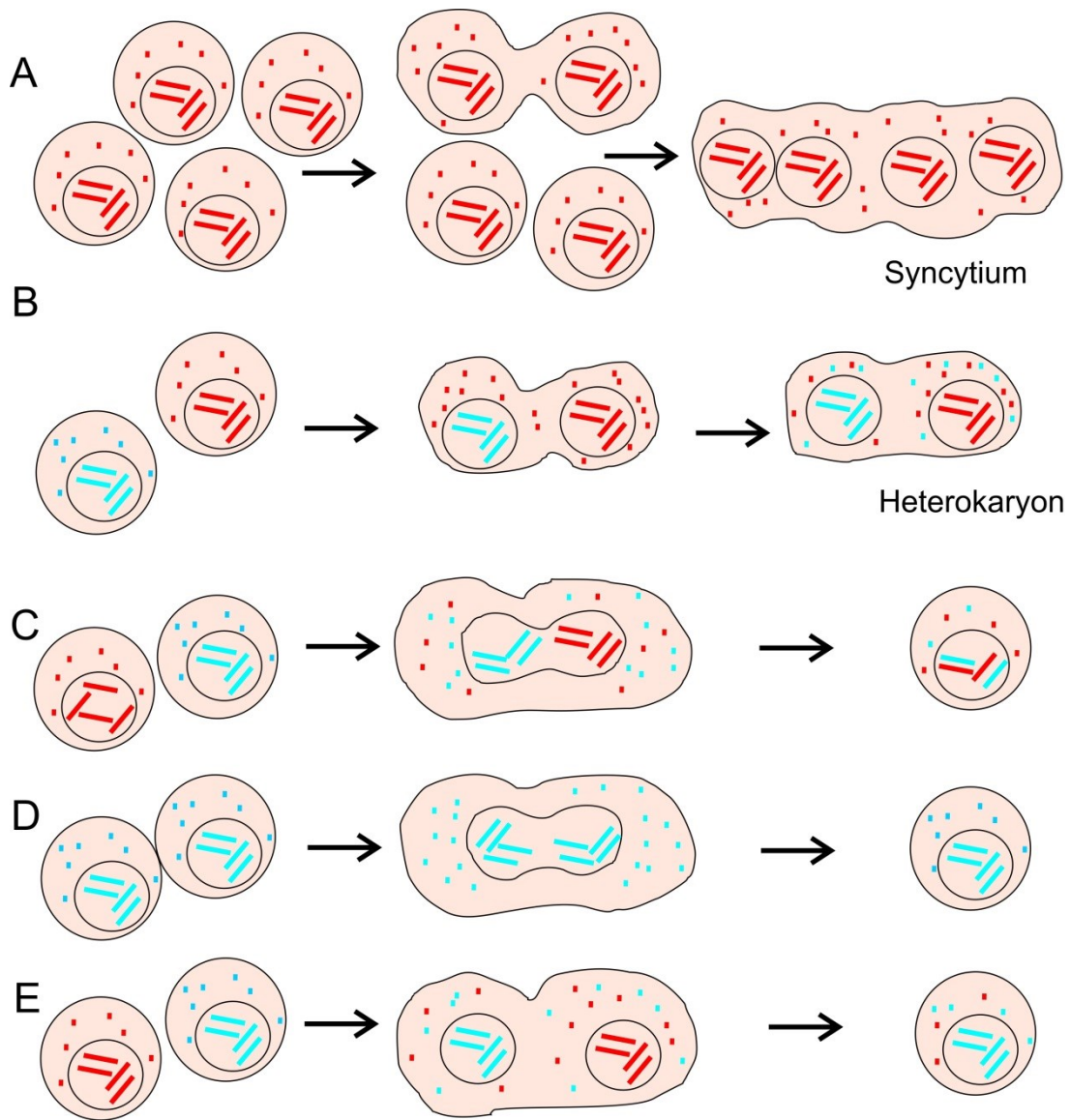


Figure 2.24: Illustration of various mechanisms of cellular fusion [84].

Although the first case of cell fusion was reported more than 150 years ago, the process of fusion is only now becoming apparent. In the model for viral fusion, the negative curvature of opposing membranes brings the outer leaflets into close contact, and an hourglass-shaped structure is generated with a stalk that opens to form a diaphragm. Tension in the extending diaphragm promotes fusion of the inner leaflets and the formation of a fusion pore. Viral

fusion takes place due to binding of a viral membrane glycoprotein to a receptor on the target cell. The process is depicted in figure 2.25 below.

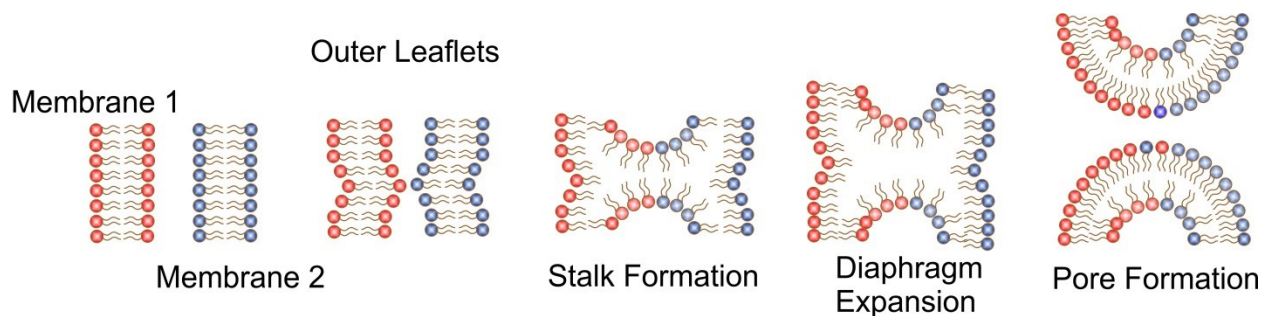


Figure 2.25: Illustration of the mechanism of viral cellular fusion [84].

Cell fusion is found to have an important role in multiple natural processes, such as morphogenesis, proliferation and for survival of the organism. The formation of hybrids between different cell types can reverse a cell to an earlier developmental stage. Cell fusion is essential in nano-scale processes such as synaptic transmission or viral infection [88]. On a larger scale, a number of important processes rely on cell–cell fusion; for example, the fusion between an oocyte and a sperm cell [89]. Cell fusion could also contribute to tissue regeneration [90], and it is well known that cell fusion contributes to the regeneration of liver tissue [89]. Selective cell fusion could be important, for example, for generating hybridoma cells for the production of monoclonal antibodies, and for the generation of autologous cancer vaccination by fusing cancer cells with dendritic cell [91-93].

A method for controlling membrane fusion has a great potential for genetic manipulation of cells. Introducing genetic material into cells allows for controlling cellular regulation, a necessary step for genetic therapies. Fusion of membranes, containing reconstituted proteins, can be used in studying membrane and protein biophysics [94] or to facilitate small-scale chemistry [95]. Additionally, creation of hybrid cells by controlled fusion allows investigation of novel

hybrid cells inheriting the properties of two different parental cell types, which has the potential to induce reprogramming of somatic cells by fusion to stem cells [96].

To date, cell fusion has been performed using laser pulses, nanoparticles, electrical cell fusion, and viral cell fusion. The most common method used to fuse cells is electrofusion, where cells are exposed to an AC electric field, followed by a DC pulse which causes cells fusion [97]. This technique; however, is non-specific where any membrane surrounded structure might fuse with another. Another cell fusion technique utilizes pulsed lasers with a well-defined wavelength, focal area and power. Laser light in the visible/NIR regime is absorbed by biological tissue and results in tissue ablation or scissoring of cells by irradiating a cell population in a medium with high power pulsed lasers [98]. Optical trapping of living cells is another technique that is proven useful for controlled fusion of selected cells. An optical trap consists of a tightly focused laser beam which pulls objects with a higher index of refraction than the surrounding media towards the focus. This technique is used to accurately position the cells in a fusion assay. Fusion of selected cells is also done by combining pulsed lasers with optical trapping. The trap is used to bring the cells of interest close together and then a pulsed laser is focused at the contact zone to mediate the fusion [99]. Another technique for cell fusion utilizes metallic nanoparticles that are trapped in the contact zone between the cells. Laser irradiation is applied on the region containing cells, resulting in absorption of the laser irradiation by the metallic nanoparticle. The nanoparticles generate heat, and thereby triggering a full fusion of the membrane structures [51,100].

Cell membrane fusion can take place via sequence of merging, where pairs of the membrane phospholipid molecules fuse to each other (see figure 2.26 1-3). First, the membrane molecules that face each other come into contact, while the molecules that has a gap remain separate at this

stage [101-103]. Membrane rearrangement called hemifusion allows phospholipid molecules from different cells to rearrange and bind to each other. Hemifusion allows for the exchange of lipids between the proximal membranes, whereas lipid exchange between the distant membranes and the exchange of aqueous content remain blocked (Figure 2.26, 3 and 4) [101-103]. The next step of fusion is the merging of the distant membrane molecules, leading to the formation of a fusion pore. Only at this stage content mixing takes place (Figure 2.26, 5). This pathway is referred to fusion-through-hemifusion [101-103]. Hemifusion is found as an intermediate step for synaptic vesicle cycle, membrane remodeling processes, viral membrane fusion and endocytotic membrane fission [102].

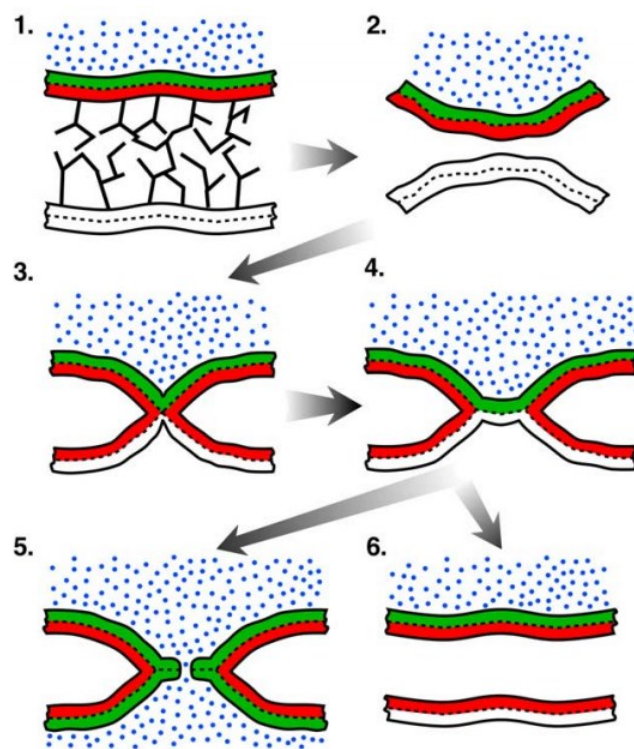


Figure 2.26: Illustration of the process of fusion-through-hemifusion [101].

Only recently researchers have been able to image the process of hemifusion using a custom-built fluorescence surface forces apparatus [104]. The group simultaneously measured the

interaction forces between supported lipid membranes and imaged lipid domains during hemifusion. Therefore, obtained real-time correlations between the interaction forces, membrane thickness and spatial and temporal domain rearrangements [104]. In chapter 4, a novel method to induce hemifusion using femtosecond laser pulses is introduced. As well as a transmission electron microscopy (TEM) technique to image cells that undergo femtosecond laser pulse induced hemifusion is illustrated. These techniques will enable scientists to study the processes of hemifusion in a more controlled environment; they will be able to choose the particular cells that they would like to hemifuse, and image those particular cells afterwards.

Chapter 3

Treatment of Retinoblastoma^{2,3}

²Portions of this chapter have been published in: Katchinskiy *et al.* Anti-EpCAM Gold Nanorods and Femtosecond Laser Pulses for Targeted Lysis of Retinoblastoma. *Advanced Therapeutics*, 1(1): 1-10, **2018**.

³ This work appears on the cover of the journal *Advanced Therapeutics*:
<https://onlinelibrary.wiley.com/doi/abs/10.1002/adtp.201870001>

3.1 Introduction

Retinoblastoma is a cancerous disease that affects the retina, and primarily affects young children, with reported incidences of 1 in 15,000 live births. Even though most children survive this cancer, they will most likely lose their vision in the affected eye [105-107].

The retina is the light-sensitive innermost layer of the eye. When light passes into the eye, it travels through the cornea and the lens and is focused on the retina. That light is then absorbed by the retinal cells, producing a cascade of chemical and electrical pulses, which, in turn, trigger optic nerve impulses. Those impulses then travel along the optic nerve to the visual centers of the brain, allowing the formation of a visual image. As shown in Fig. 3.1, the retina is composed of the following layers: photoreceptors, bipolar cells, ganglion cells, horizontal cells, and amacrine cells [108]. Damage to the retinal cell layers will result in irreversible changes to its intricate structure. As such, any surgical treatment (mechanical or laser-based) must be noninvasive. The ability of retinal cells to regenerate is extremely limited [108]. Therefore, when treating any condition affecting the retina, it is imperative to preserve as many healthy cells as possible in order to preserve the patient's' vision. To date, no treatment has been developed that targets only cancerous cells for patients suffering from ocular cancer (e.g. retinoblastoma). The first and most common sign of retinoblastoma is leukocoria, which is the abnormal appearance of the retina [105-107]. Symptoms include deterioration in vision, glaucoma, red and irritated eye, squint, and strabismus (cross-eyes). In some cases retinoblastoma is accompanied with visual-motor developmental delays [105-107]. The diagnosis of a child with suspected retinoblastoma includes a complete ophthalmic evaluation where a dilated fundus examination under anesthesia is required [105-107]. The ophthalmologist measures the intraocular pressure and examines the anterior segment for inflammation, neovascularization, pseudo-hypopyon (cells infiltrating the

anterior chamber of the eye resembling a hyphema), and hyphema (accumulation of blood inside the anterior chamber of the eye). A bilateral fundus examination with 360° scleral depression and direct visualization of the tumor are also crucial for diagnosis of retinoblastoma.

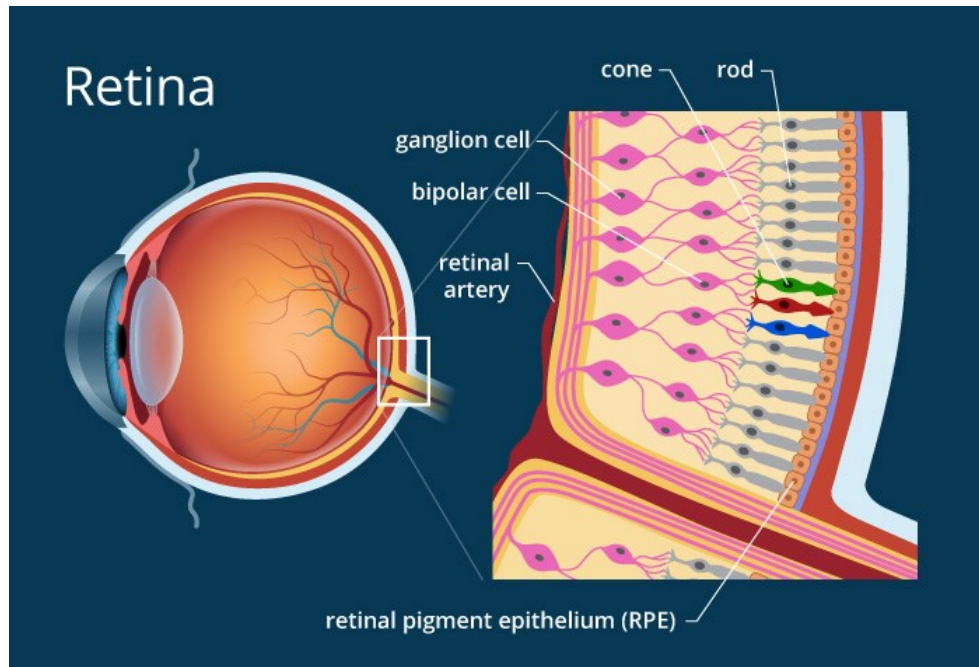


Figure 3.1: Illustration of retina and its cell layers (figure taken from <https://www.allaboutvision.com/resources/retina.htm>)

Retinoblastoma is the most common malignant eye tumor of childhood. Retinoblastoma cancer is unusual in several respects when compared with most other solid tumors and ocular and adrenal tumors: 1) It tends to be multifocal and often bilateral, 2) it occasionally spontaneously regresses, 3) there is a well-established hereditary relationship in a significant number of cases and, 4) it frequently occurs as a congenital tumor [105-107]. Retinoblastoma is a cancer that is effectively treated, however, treatment frequently entails removal of the eye or loss of visual function. To date, the primary goal of treatment of retinoblastoma is to save the child's life, while the preservation of the eye and its functionality are the secondary goals. Once diagnosed,

the treatment methodology is determined on a case by case basis, and includes one or more of the available treatment modalities. Those include: (a) Enucleation of the eye – Children who suffer from advanced retinoblastoma in only one of their eyes will undergo enucleation of the diseased eye. Children with retinoblastoma in both eyes, will first undergo other treatments, and only if all other treatments fail, will undergo enucleation. (b) Brachytherapy – is a treatment where a radioactive plaque is implanted on the sclera, near the tumor. (c) External beam radiotherapy (EBR) – is mainly used on children who suffer from retinoblastoma in both eyes. In this therapy, a beam of radiation is used to irradiate and kill the tumors. (d) Systemic or intra-arterial chemotherapy – is the use of medications to kill the tumor cells. Such medications kill the cancer cells; however, they have severe side effects as they also affect many other healthy cells in the body. Chemotherapy is used when the tumor is too large or too small to treat with more direct treatment approaches, such as EBR or brachytherapy. (e) Cryotherapy – is when the tissue is frozen quickly in order to induce damage to the blood vessels supplying the tumor cells. This therapy method can be used on small peripheral tumors. (f) Thermotherapy - is the application of direct heat on the tumor. The heating source usually used is infrared radiation. This treatment modality is used on small tumors. (g) Laser photocoagulation – is a treatment where a laser beam is used to coagulate all the blood supply to the tumor cells. Typical lasers that are used for this treatment are CW lasers; this method is normally used on small posterior tumors.

The main challenge in the treatment of retinoblastoma and many other cancer types is the formation of metastatic and secondary tumors that reduce lifespan and quality of life [105-107]. The common hypothesis for the reoccurrence of subsequent tumors is the persistence of cancer stem cells [109]. These cells are small subpopulations of cells that are primarily responsible for tumor evolution and are resistant to chemotherapy [110-112] and radiation treatments [110-112].

Notably, Cancer stem cells are reported to exist in breast cancer [111], prostate cancer [112], lung cancer [110], leukemia [113,114], and brain tumors [115]. Epithelial cell adhesion molecule (EpCAM) is a molecule which was identified as a marker for cancer stem cells of oval and liver cells [116,117]. Krishnakumar et al. showed that EpCAM is highly expressed in invasive retinoblastoma tumors compared to noninvasive tumors [118]. EpCAM was found to be also co-expressed with three other cancer stem-like cell markers: CD44, CD24 and ABCG2 [119]. Thus, it was concluded that EpCAM+ Y79 retinoblastoma cells behave like cancer stem cells and are recognized as cells that are resistant to treatment [119]. Developing a technique to treat cancer stem cells such as EpCAM+ Y79 retinoblastoma cells would be a valuable tool for the development of treatment for chemotherapy and radiation resistant cancer cell lines. It would significantly improve the prognosis and quality of life of patients suffering from aggressive and invasive tumors.

A novel cancer treatment approach currently under investigation is the induction of tissue hyperthermia mediated via MNPs irradiated with laser light. In order to have an effective cancer treatment with this methodology, it is crucial to be able to deliver the laser pulses to the treatment site, especially for non-superficial cancers, while keeping the energy fluence below the damage threshold of the healthy cells. As such, a delicate balance must be realized between the laser-tissue interaction parameters: energy fluence, and penetration depth of the optical pulse, pulse train duration, and exposure/time. In the case of retinoblastoma, which affects a thin layer within the eye, delivering the femtosecond laser pulses directly onto the retina through the cornea, anterior chamber, pupil, lens, and vitreous humor, without interacting with such compartments, makes this treatment ideal for this type of cancer. Notably, once the laser pulses are delivered to the tumor site, it is crucial that the laser intensity throughout the depth of the

tumor is maintained above a certain threshold intensity to achieve an effective treatment throughout the entire cancerous area. For ultrashort laser pulses, linear/non-linear absorption and scattering limit laser power that can be delivered, and thus, hinders treatment of buried tumors. A central wavelength around 800nm is critical, since at this wavelength all compartments of the eye have low absorption, allowing the laser light to reach the retina with sufficient laser intensity for inducing an effective treatment of early stage retinoblastoma. At that stage, the tumor is confined to the retina, and is only 1-3mm in thickness.

While multiple investigations to date have focused on studying the mechanism of laser light-nanoparticle interaction and nanoparticle-tissue interaction [30,51,120-122], here, we provide a complete assessment of the optimal laser parameters, cancer-targeting vector, and nanoparticle concentrations required for the development of a translational retinoblastoma cancer treatment. In the following chapter we demonstrate a highly effective treatment of retinoblastoma cancer cells using high intensity femtosecond laser pulses and retinoblastoma cell-targeting Au-NRs.

3.2 Experimental Materials and Methodology

3.2.1 Cell Culture

To confirm that treatment of retinoblastoma cancer is possible with Au-NRs and femtosecond laser pulses, Y79 retinoblastoma cells were grown in suspension. The cells were cultured in an incubator with 5% CO₂ at 37°C, in Dulbecco's modified Eagle medium (DMEM) supplemented with 100 U/ml penicillin, 100 µg/ml streptomycin, and 10% fetal bovine serum.

Y79 retinoblastoma was obtained by T. W. Reid et al. in 1971 [123], due to clinical findings in patient from whom cell line was established. The cell line was established from a tumor in the eye of a 2.5 year-old white girl. The patient had a strong maternal family history of

retinoblastoma. Three of the mother's siblings and a 1.5 year old sibling of the patient have been affected. The patient's right eye was enucleated on January 1971, and a portion of the globe was taken for tissue culture studies and electron microscopic examination. The child did well postoperatively, with no re-appearance of tumor in the right socket and no occurrence of retinoblastoma in the left eye [123].

Characteristics of Y79 in culture are that most explant of the tissue cultures show similar early growth patterns. Migration of cells was seen at the edges of some explants 24-96 hours after the tissue was put into culture. The explants are predominantly spindle-shaped and small epithelioid cells. Polygonal and neuronal cells can also appear. As the cells continue to grow in culture, the spindle-shaped configuration predominates [123]. Two to twelve weeks after initiation, smaller round cells developed on the spindle-cell matrix. These subsequently separate and grow as a suspension culture. The floating clumps of cells gradually increase in number and size. These clumps are maintained independently of the cells adhering to the wall of the flask, with doubling time of 52 hours. The predominant morphologic type of cell is small, round, undifferentiated cell with little cytoplasm and a large hyperchromatic nucleus [123].

3.2.2 Nanorods and Cancer Cell Targeting

Bare PEGylated and anti-EpCAM (Epithelial cell adhesion molecule) PEGylated 11nm×43nm Au-NRs with LSPR at 808nm were purchased from NANOPARTZ INC (USA). Fetal retinal cells (FRCs) were used as control cells to differentiate between cancer cells (Y79) and 'normal' acting cells (FRCs). The Y79 retinoblastoma cells and fetal retinal cells were incubated for 1 hour with either bare PEGylated Au-NR, or anti-EpCAM conjugated Au-NR. The cell cultures were then centrifuged to remove excess Au-NRs and re-suspended in Dulbecco's Modified Eagle Medium (DMEM). Two-photon microscopy was used to confirm the accumulation of Au-NRs in

Y79 retinoblastoma cells, to assess the ability of anti-EpCAM functionalized Au-NRs to target retinoblastoma cells while sparing ‘normal’ cells (FRCs).

Gold nanorods synthesis procedure is based on seeded-growth method. The preparation is divided into a seed nucleation and a growth step. The basic protocol is as follows, for the seed solution: a hexadecyl-trimethyl-ammonium bromide (CTAB) solution is mixed with Chloroauric acid (HAuCl₄) solution. The yellow solution is stirred with sodium borohydride solution, until it changed its color from blue-grey to amber. For the growth solution: CTAB and sodium oleate are dissolved in water at 50 °C. After the solution had cooled down to 30 °C, AgNO₃ solution is added. Subsequently, Au³⁺ solution is added and an orange-yellow mixture is stirred until it is colorless. To the colorless growth solution, HCl is added, and then ascorbic acid solution and seed solution are added [124].

In order to coat the gold nanorods with PEG (polyethylene glycol), a solution of gold nanorods containing CTAB is mixed with methoxy polyethylene glycol thiol (mPEG 5000-SH). The mixture is stirred for 24 hrs at room temperature, and then dialyzed for 3 days [45].

3.2.3 Femtosecond Laser Pulse Delivery System

The treatment of Y79 retinoblastoma cells was performed by using 35fs laser pulses at a central wavelength of 800 nm, that were delivered from a Ti:Sapphire laser pulse amplifier at a repetition rate of 1KHz. The laser pulses were delivered to an upright Nikon Eclipse 80i optical microscope and directed towards the Y79 retinoblastoma cells. A 4× microscope objective was used to image the cells using a CMOS camera, and to focus the laser beam diameter to a 400µm spot size (see Figure 3.2). At the focal spot, the laser pulse train average power, energy, and intensity were: 50 mW, 50 µJ/pulse, and 1.45 TW/cm², respectively. A glass bottom 8-well Cell Culture Slides (Mattek Corp) was used to contain the Y79 cells, which was mounted on a

motorized x-y-z nano-translation stage. During the scanning of the culture slides (1cm×1cm area), 20 laser pulses were delivered to each irradiated spot.

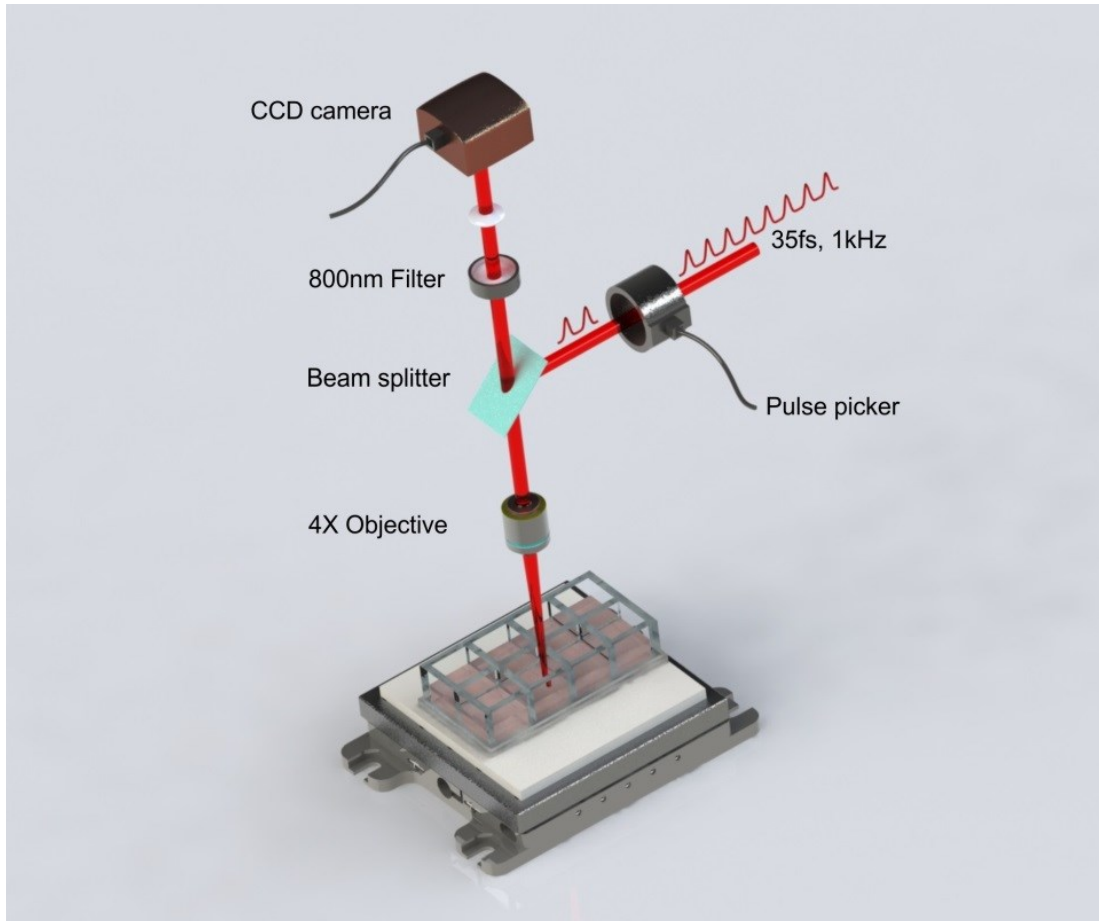


Figure 3.2: Experimental setup. Ti:Sapphire femtosecond laser pulse amplifier emitting 35 femtosecond laser pulses with a center wavelength of 800nm and a pulse repetition rate of 1KHz. The pulses pass through a high speed shutter and are delivered to a 4× objective lens. The procedure was visualized with a CMOS camera.

3.2.4 Viability Assay

To assess the ability to destroy retinoblastoma cells using femtosecond laser pulses and cancer targeting Au-NRs, retinoblastoma cells were plated in 24-well plates (1 mL/well) and treated as follows: (1) Retinoblastoma cells were incubated for an hour with targeting Au-NRs (PEGylated anti-EpCAM Au-NRs). The cells were centrifuged afterwards to remove excess Au-NRs and resuspended in DMEM, and scanned with femtosecond laser pulses (see *Femtosecond laser pulse delivery system*). (2) Retinoblastoma cells (without Au-NRs) were scanned with femtosecond laser pulses (see *Femtosecond laser pulse delivery system*). (3) Control retinoblastoma cells. (4) Control retinoblastoma cells incubated for an hour with the targeting Au-NRs (PEGylated anti-EpCAM Au-NR). The cells were centrifuged afterwards to remove excess Au-NRs, and resuspended in DMEM.

To evaluate the biocompatibility of the Au-NRs, cellular survival due to laser treatment alone, and laser treatment combined with Au-NRs, was quantified using fluorescence imaging and 3-(4,5-dimethylthiazol-2-yl)-5-(3-carboxymethoxyphenyl)-2-(4-sulfophenyl)-2H-tetrazolium (MTS) cellular metabolism assay. For fluorescence imaging viability assay post-treatment, Y79 retinoblastoma were centrifuged at 1300 rpm for 5 min to remove DMEM media. The cells were resuspended in 1 ml Dulbecco's phosphate-buffered saline (DPBS) solution. Cells in each well were incubated for 1 h with 1 μ l Calcein AM, 3 μ l propidium iodide, and 0.5 μ l Hoechst dye. The cells were centrifuged at 1300 rpm for 5 min to remove excess fluorescent dyes, and resuspended in DPBS solution. The cells were imaged using high-content screening (HCS) microscopy. Cell counting software MetaXpress (Molecular Devices) was used to determine the number of live and dead cells. For the MTS cell proliferation assay, Y79 retinoblastoma cells were centrifuged at 1300 rpm for 5 min to remove DMEM media. The cells were resuspended in

100 μ l of non-antibiotic containing DMEM media. Twenty μ l MTS reagent was added to each well. Cells were incubated in 5% CO₂ at 37°C for 4 h, and the absorbance (490 nm) was measured and analyzed using a microplate reader FLUOstar OPTIMA (BMG LABTECH).

3.2.5 Statistical Analysis

Normalization: All data has been normalized against the control sample. All values presented in this document were expressed as mean \pm standard deviation (s.d.). Statistical analyses were performed using Microsoft Excel. The viability assay data was obtained using high-content screening (HCS) microscopy. Cell scoring was performed using MetaXpress (Molecular Devices), and the data was used to determine the number of live and dead cells. For the laser parameters and Au-NR concentration reported in this thesis, two experiments, spaced a week apart, were performed. Each experiment included 2 sets of: AuNRs & femtosecond (fs) laser pulses, Laser pulses only, Untreated (control), and Au-NRs only (totaling 8 sets).

For metabolism assay MTS assay was performed. The absorbance (@ 490 nm) was measured and recorded using a microplate reader FLUOstar OPTIMA (BMG LABTECH). For the laser parameters and Au-NR concentration reported in this thesis, two experiments spaced a week apart (these independent experiments were performed a week after the viability assay experiments were done). Each experiment included 2 sets of: AuNRs & fs laser pulses, Laser pulses only, Untreated (control), and Au-NRs only (totaling 8 sets).

A student t-test was performed, to estimate the significance of difference between the control group and all three other groups (AuNRs & fs laser pulses, Laser pulses only, and Au-NRs only).

3.3 Results

3.3.1 Targeting

Figure 3.3 shows 2-photon microscopy images of the PEGylated Au-NRs conjugated with anti-EpCAM accumulation in Y79 retinoblastoma cells. Figure 3.2A depicts partial accumulation of Au-NRs in a Y79 cell, while higher concentration of Au-NRs accumulating in a Y79 cell can be seen in Figure 3.3B (the red parts represent accumulation of Au-NRs). A 3D confocal scan in Figure 3.3C illustrates that most of the Au-NRs accumulate on the surface of the Y79 cells. This is evident since EpCAM is an antigen that is expressed on the surface of the cell, thereby supporting the findings of accumulation of Au-NRs on the cell surface. Nonetheless, some of the Au-NRs may enter the cell as well. Notably, bare Au-NRs did not accumulate in retinoblastoma cells (results are not shown in here). These findings indicate that it is necessary to conjugate the Au-NRs with a cancer targeting vector in order to induce accumulation at the cellular sites.

Selective binding of anti-EpCAM to retinoblastoma cells was assessed by comparing its accumulation in FRCs. FRCs were also incubated with bare PEGylated and PEGylated anti-EpCAM Au-NRs. Figure 3.4A is a 3D confocal image of FRCs, where it can be seen that no Au-NRs are accumulated throughout these cells (red color represents Au-NR accumulation, which is not observed here). Figures 3.4B and 3.4C are 2-photon images of different sites along FRC. Again, no accumulation of Au-NRs is observed. These results indicate that anti-EpCAM can be used as a specific targeting vector for Y79 retinoblastoma cells.

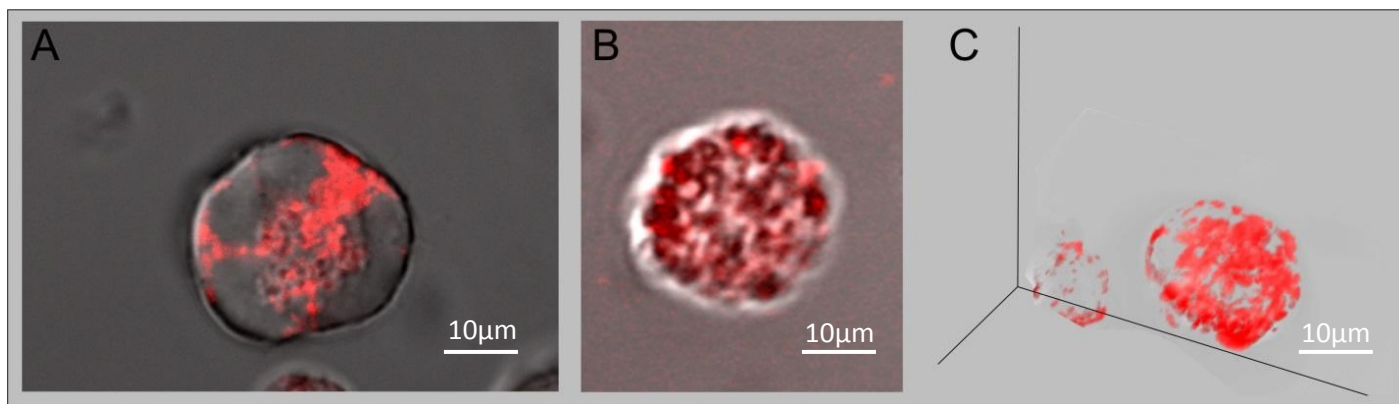


Figure 3.3: A-B. 2-photon microscope images of Y79 retinoblastoma cell incubated with PEGylated anti-EpCAM Au-NRs. C. 3D confocal image of two Y79 retinoblastoma cells incubated with PEGylated anti-EpCAM Au-NRs.

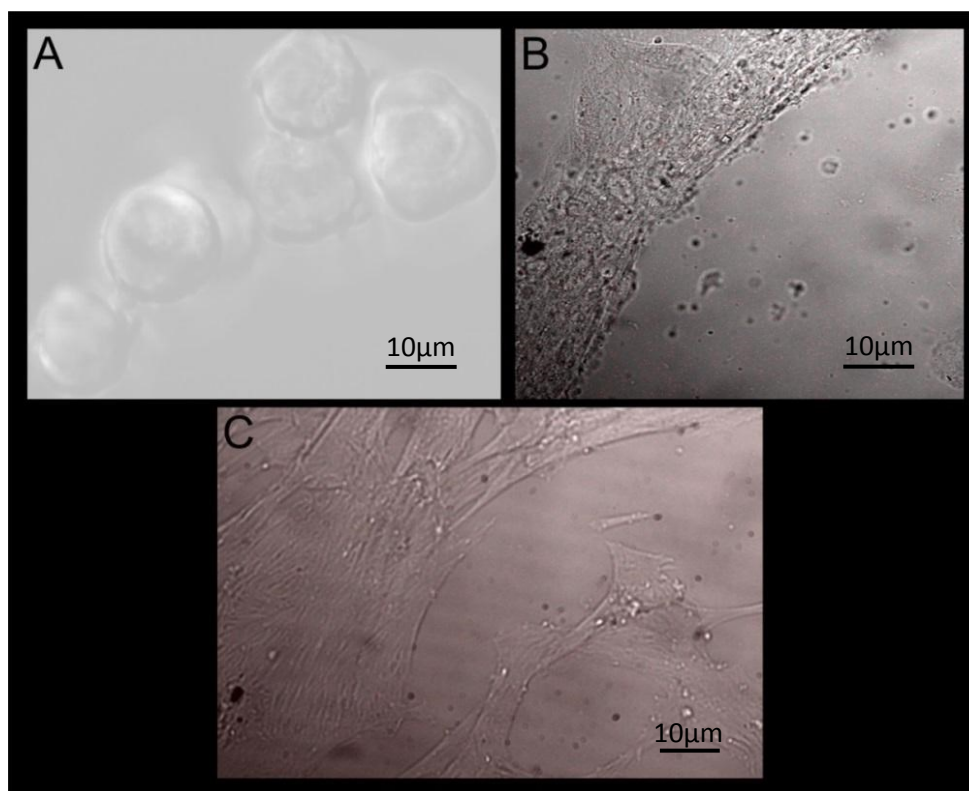


Figure 3.4: A. 3D 2-photon image of FRCs incubated with anti-EPCAM Au-NRs. B-C. 2-photon microscope image of fetal retinal cells, incubated with anti-EPCAM Au-NRs.

Similar targeting experiments were performed on breast cancer cells (EMT-6) and human colon carcinoma (HCA-7). The cells were incubated with targeting Au-NRs, then washed and imaged using transmission electron microscope (TEM). As seen in figures 3.5 and 3.6, most of the Au-NRs accumulate on the surface of the cells, while some are uptaken by the cells.

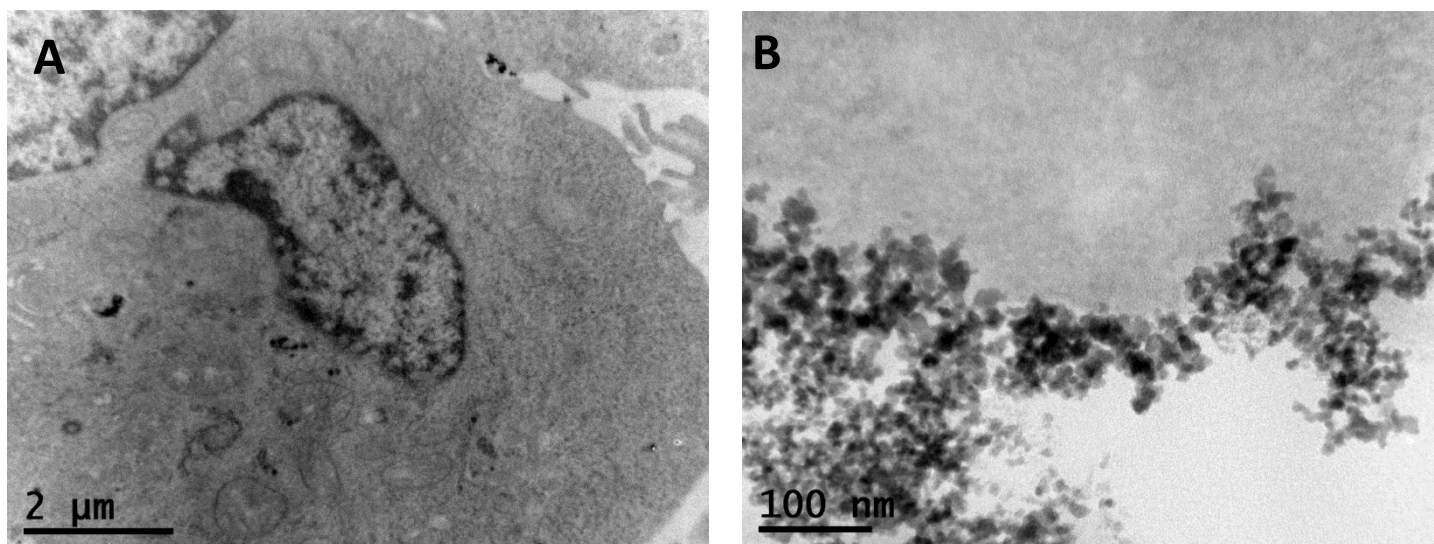


Figure 3.5: TEM imaging of targeting of breast cancer cells (EMT-6) using anti-EpCAM Au-NRs. A: Uptaken particles inside the cells. B: Accumulation of particles on the cell surface.

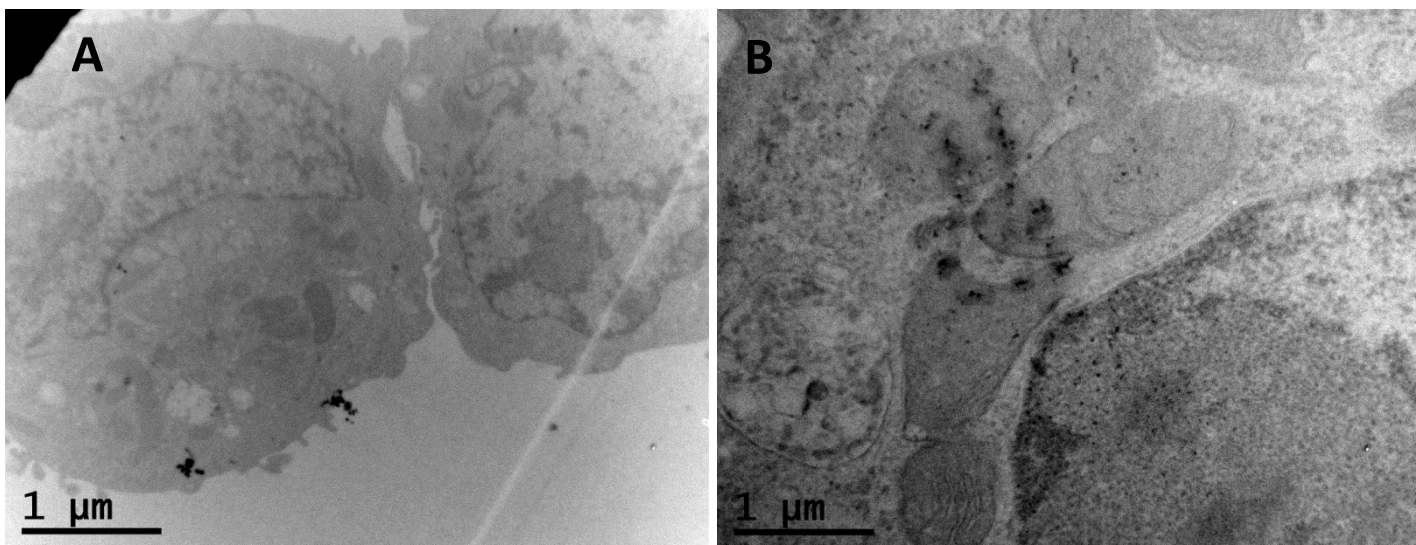


Figure 3.6: TEM imaging of targeting of human colon carcinoma (HCA-7) using anti-EpCAM Au-NRs. A: Accumulation of particles on the cell surface. B: Uptaken particles inside the cells.

3.3.2 Femtosecond Laser Pulse Treatment of Retinoblastoma

The irradiation of retinoblastoma cells with femtosecond laser pulses was visually assessed during the treatment by live recording. Representative bright field images are shown in Figures 3.7 and 3.8. Each spot was irradiated with 20 laser pulses of $400\mu\text{m}$ in diameter, as the $1\text{cm} \times 1\text{cm}$ well was translated. To assess the effect of the laser beam alone on retinoblastoma cells, we exposed the cells to laser irradiation. As shown in Figure 3.7, the irradiated cells show no sign of damage. Based on the visual observation, this indicates that the laser irradiation intensity of $1.45\text{TW}/\text{cm}^2$ does not ablate the cells.

However, the situation is different when Au-NRs are introduced to the retinoblastoma cells, and exposed to the same laser irradiation intensity, where an immediate cell ablation is observed. Figure 3.8 depicts a representative brightfield images before, during and after laser irradiation. In figure 3.8A, the dotted circle marks the region of cells to be exposed to the laser pulses. In figure 3.8B, the laser pulses exposure is shown and confined inside the dotted circle. The cell ablation is noticeable immediately after laser irradiation, followed by the cells dissolving into the surrounding media, as visualized in Figure 3.8C inside the dotted circle.

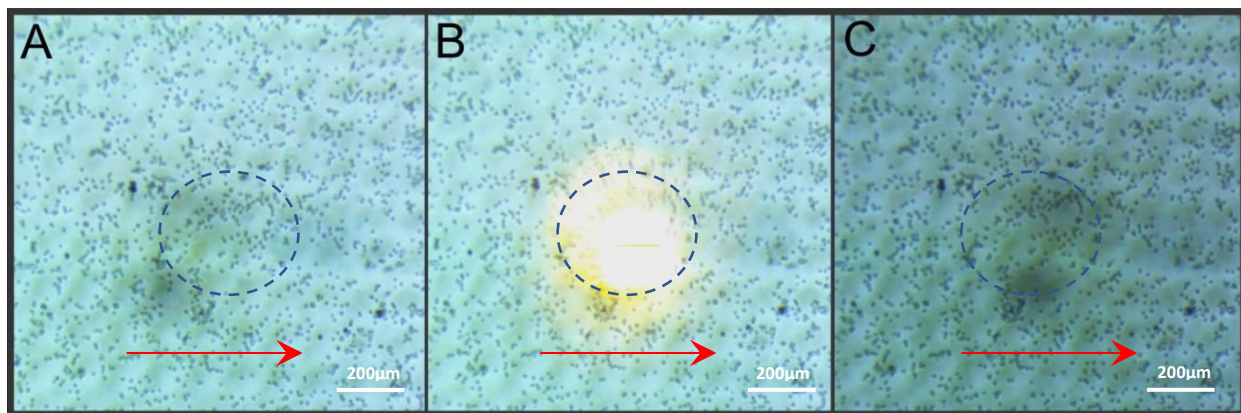


Figure 3.7: **A.** Bright field image right before femtosecond laser pulse irradiation of retinoblastoma cells, not containing Au-NRs. **B.** Bright field image during femtosecond laser irradiation of cells **C.** Bright field image right after femtosecond laser irradiation of retinoblastoma cells. The area of laser irradiation is marked with the dotted circle. Laser scanning direction is marked with arrow. Laser beam diameter of 400µm spot size. At the focal spot, the laser pulse train average power, energy, and intensity were: 50 mW, 50 µJ/pulse, and 1.45 TW/cm², respectively.

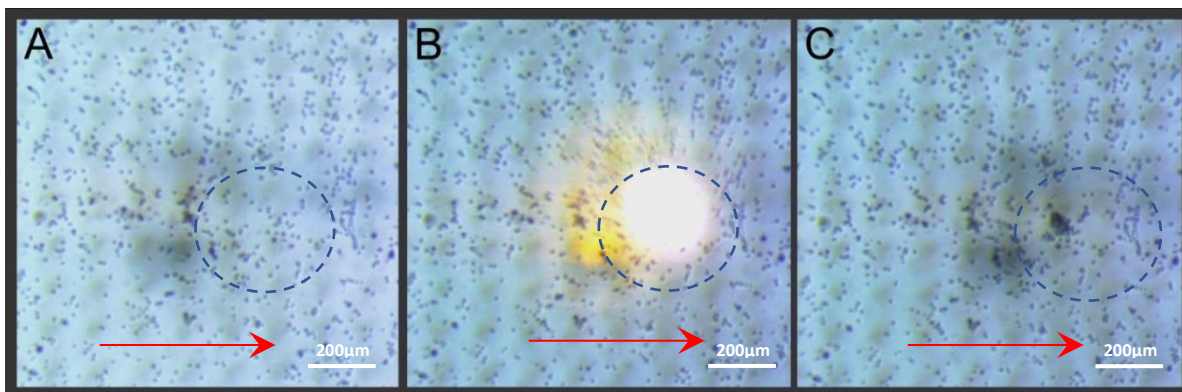


Figure 3.8: **A.** Bright field image right before femtosecond laser pulse irradiation of retinoblastoma cells, containing Au-NRs. **B.** Bright field image during femtosecond laser irradiation of retinoblastoma cells. **C.** Bright field image right after femtosecond laser irradiation of retinoblastoma cells. The area of laser irradiation is marked with the dotted circle. Laser scanning direction is marked with arrow. Laser beam diameter of 400µm spot size. At the focal spot, the laser pulse train average power, energy, and intensity were: 50 mW, 50 µJ/pulse, and 1.45 TW/cm², respectively.

While the above-mentioned cell destruction has been observed for retinoblastoma cells containing Au-NRs, it is not evident that the ablation took place at the membrane where the Au-NRs have accumulated. As such, high magnification imaging is necessary to visualize the process that takes place during laser irradiation of Au-NRs containing cells to support the claim that the Au-NRs facilitate the destruction of the cells. Figure 3.9 depicts sequential 2-photon images, taken 5 seconds apart, of four Au-NRs containing retinoblastoma cells that were exposed to fs laser pulses. Figure 3.9A shows the cells right before laser irradiation begins. Figure 3.9B, right after laser irradiation cell (i) membrane begin to rupture, possibly due to the formation of cavitation bubbles. In Figure 3.9C, the damage to cell (i) extends while cell (ii) begins to rupture as well. This indicates that the intake of Au-NRs into the cells is different; therefore, cellular damage is easier to induce with higher concentration of Au-NRs. In Figure 3.9D, the damage to

cell (ii) is expanding, while cell (i) has been completely destroyed through the loss of its membrane integrity. The disappearance of the photoluminescence from the Au-NRs in cell (i) indicates that resonant coupling (which is Au-NR shape dependent) of the laser with the Au-NRs has been affected. That is, imaging of Au-NRs using 2-photon microscopy relies on the local field absorption, which is enhanced at the LSPR. When the Au-NRs melt and change their shape, the LSPR shift away from the optimal coupling condition and thus reduces the photoluminescence. In Figure 3.9E, cell (ii) has suffered significant damage and is exhibiting extensive blebbing and loss of its membrane integrity. Notably, damage is only observed in regions containing high concentration of Au-NRs, which indicate that the Au-NRs are necessary for facilitating the cellular ablation process.

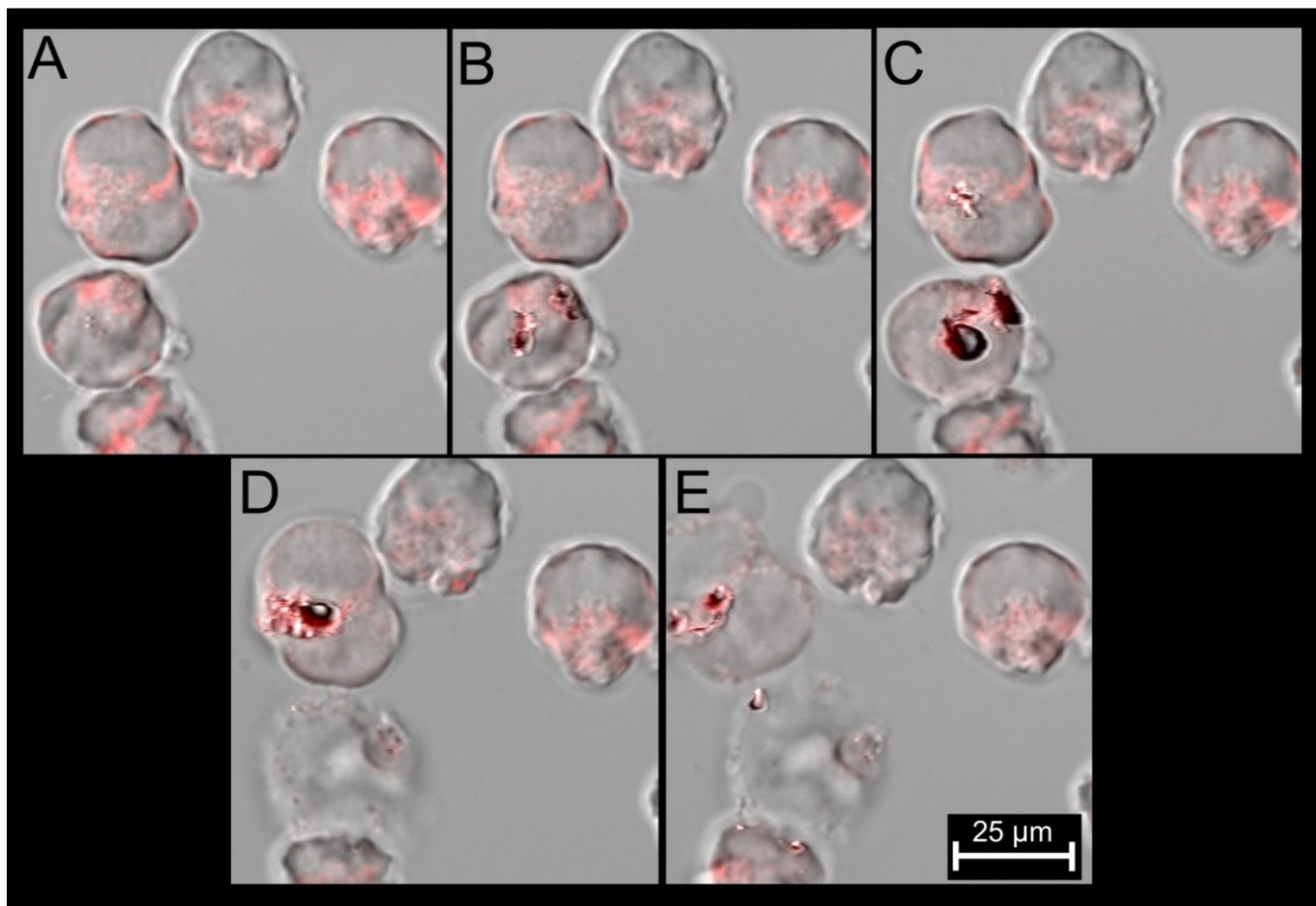


Figure 3.9: A-E. Time lapse of 2-photon imaging of fs laser pulse irradiation of retinoblastoma cells that contain Au-NRs. At the focal spot, the laser pulse train average power, energy, and intensity were: 50 mW, 50 $\mu\text{J}/\text{pulse}$, and $1.45 \text{ TW}/\text{cm}^2$, respectively.

To confirm the previous observation that the Au-NR's photoluminescence disappearance is due to melting of the Au-NRs which results in cell rupturing, the effects of fs laser pulses on the Au-NRs were studied by imaging the Au-NRs with field-emission scanning electron microscopy (FESEM). Figure 3.10 shows the anti-EpCAM conjugated Au-NRs where the Au-NRs have a rod-like shape with average dimensions of $11 \text{ nm} \times 43 \text{ nm}$. Interestingly, as shown in Figure 3.11 after being exposed to fs laser pulses, the Au-NRs clearly melt and change their shape into spheres. These findings further support the fact that the exposure of the Au-NRs to the fs laser

pulses results in rapid heating and melting of the Au-NRs, which causes the rupturing of the retinoblastoma cells.

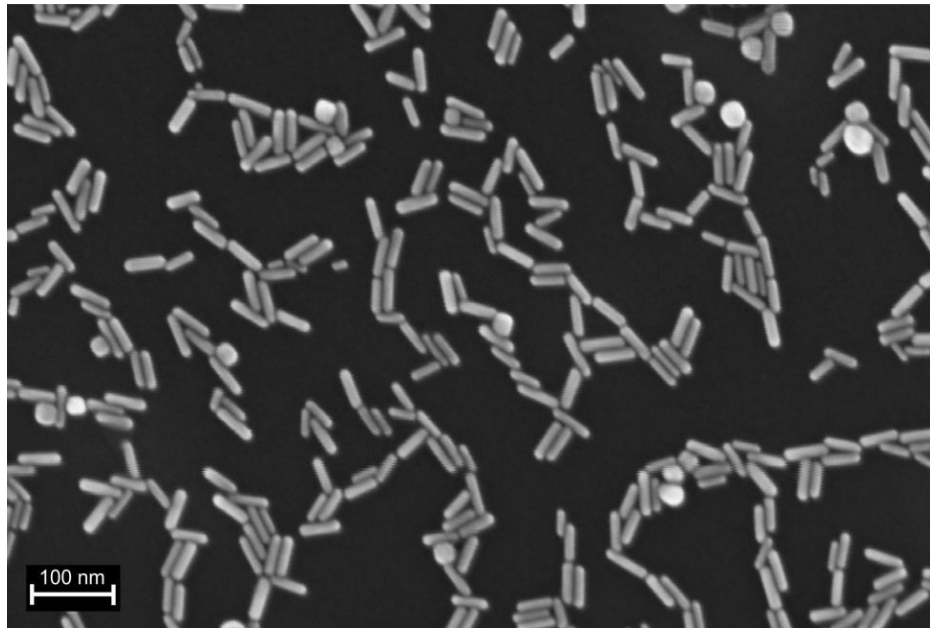


Figure 3.10: FESEM image of Au-NRs before laser irradiation.

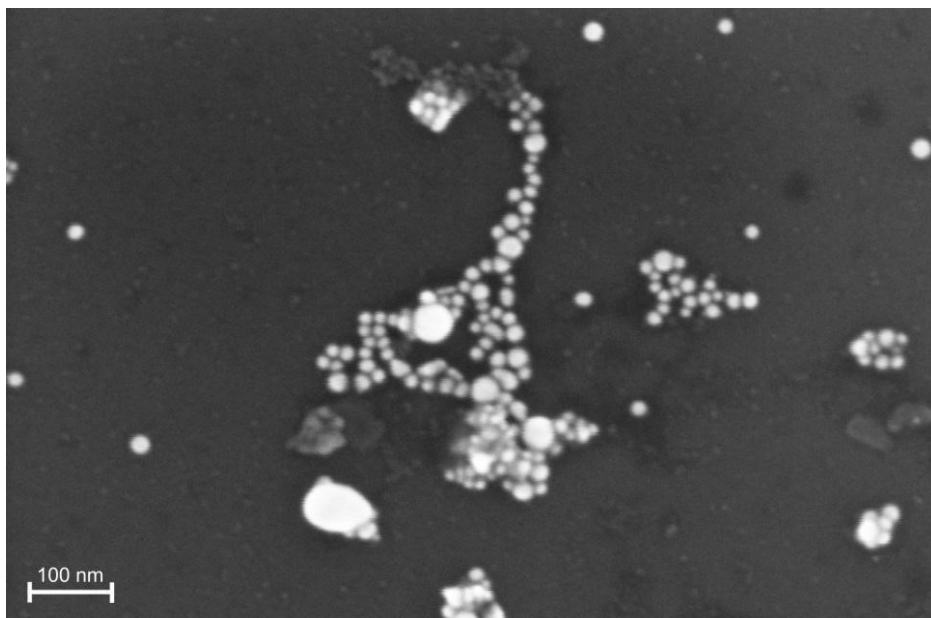


Figure 3.11: FESEM image of Au-NRs after laser irradiation. At the focal spot, the laser pulse train average power, energy, and intensity were: 50 mW, 50 $\mu\text{J}/\text{pulse}$, and 1.45 TW/cm^2 , respectively.

3.3.3 Viability Results

While the previous results, which rely purely on visual assessments, indicate cell rupturing when Au-NR containing retinoblastoma cells are exposed to fs laser pulses, it is important to confirm that the cells are indeed damaged via biological viability evaluation. Viability tests were performed using both Calcein-AM /propidium iodide (PI) fluorescence microscopy viability assay, and MTS proliferation assay. A representative example of Calcein-AM/propidium iodide (PI) fluorescence images of retinoblastoma cells that were treated by laser alone compared to laser treated Au-NR containing retinoblastoma cells is depicted in Figure 3.12. In Figure 3.12A, cells which do not contain Au-NRs were exposed to fs laser pulses and fluoresced green, indicating that the cells are viable. Thus, confirming that exposure to fs laser pulses alone does not affect the cell viability. In contrast, as shown in Figure 3.12B, Au-NRs targeted cells fluoresce red after being exposed to laser pulses, which indicate that these cells are dead.

As seen in Figure 3.13, a summary of the MTS analysis shows the results for: (i) retinoblastoma cells treated with Au-NRs and irradiated with fs laser pulses, (ii) retinoblastoma cells irradiated with fs laser pulses only, (iii) untreated retinoblastoma cells (control), and (iv) retinoblastoma cells treated with Au-NRs without fs laser irradiation. It was found that in cases (ii) and (iv), close to 100% of the cells (no significant differences were found compared to untreated cells) are viable, confirming that laser irradiation alone does not affect the cells and that treating the cells with Au-NRs does not interfere with the cellular metabolism.

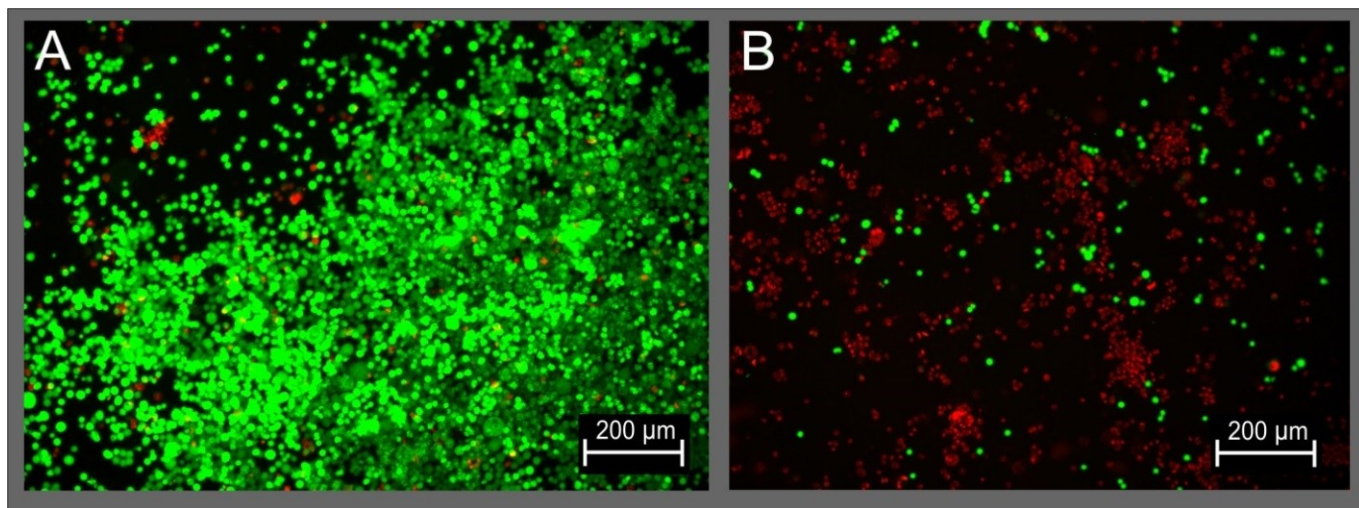


Figure 3.12: Fluorescence microscopy images. **A.** Retinoblastoma cells that do not contain Au-NRs exposed to laser pulses. The cells that appear green contain Calcein AM which indicate that the cells are viable. **B.** Retinoblastoma cells that contain Au-NRs and exposed to fs laser pulses. Most of the cells appear red in this case, which indicate that these cells are dead and contain propidium iodide (PI). Laser beam diameter of 400 μm spot size. At the focal spot, the laser pulse train average power, energy, and intensity were: 50 mW, 50 $\mu\text{J}/\text{pulse}$, and 1.45 TW/cm^2 , respectively.

In case (i) a single treatment of fs laser pulse irradiation of retinoblastoma cells containing Au-NRs resulted in cellular viability drop, to $\sim 10\%$ of untreated controls. Repeating the above-mentioned experiments using fluorescence viability analysis yielded similar results (presented in Figure 3.14). For cases (ii) and (iv), 85%-90% of the cells are viable, reaffirming that laser irradiation alone does not affect the cells and that treating the cells with Au-NRs doesn't affect the cellular viability. In case (i), however, the cellular viability drops significantly to $\sim 25\%$ after one treatment only. These results confirm that the combination of Au-NRs with fs laser pulses is extremely effective for treatment of retinoblastoma. Both MTS proliferation assay and

fluorescence microscopy methods were in agreement and show that laser treatment of retinoblastoma containing Au-NRs result in 75%-90% of cell death, after a single treatment. Notably, the treatment time is extremely short; therefore, this methodology can be applied multiple times to achieve complete eradication of the cancer cells.

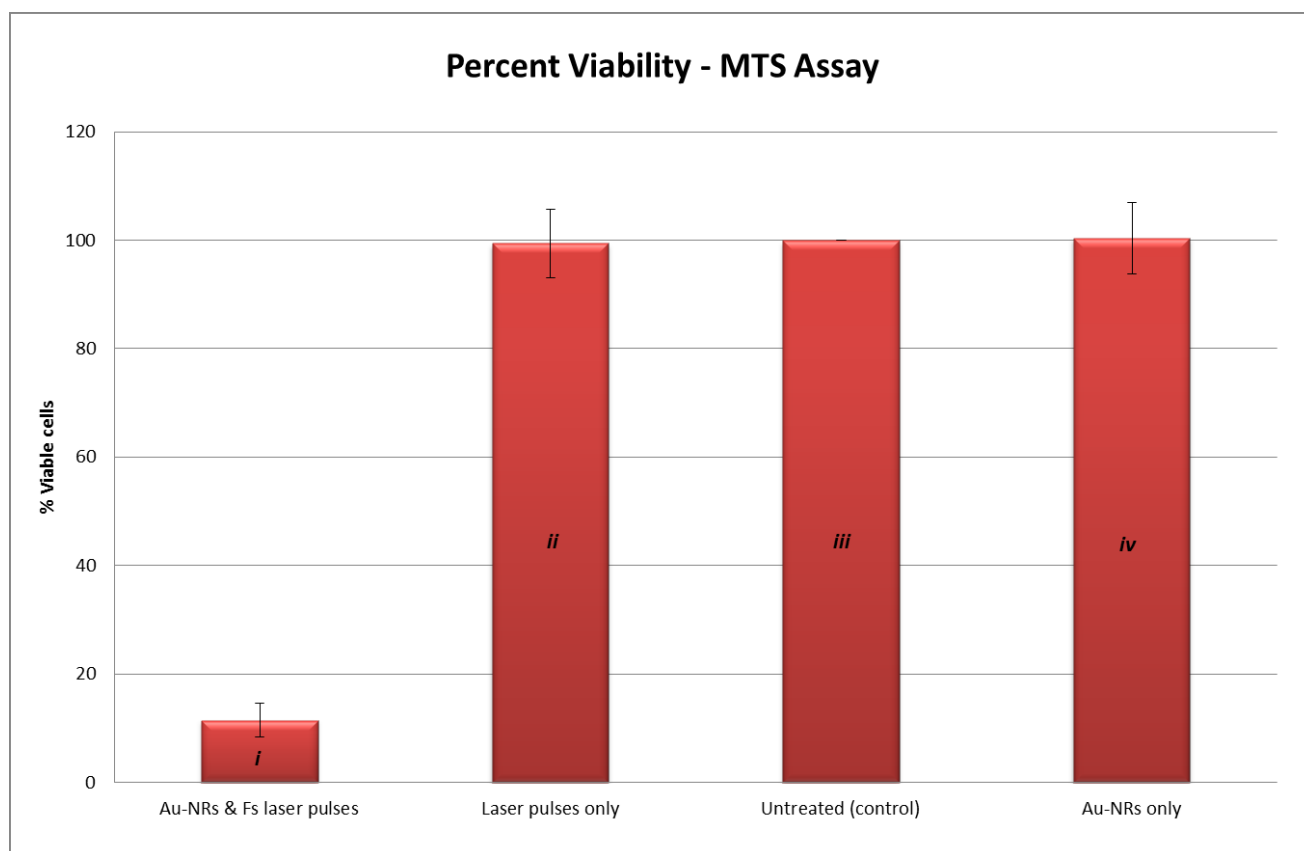


Figure 3.13: MTS metabolism assay of retinoblastoma cells. No significant difference between laser pulse, Au-NRs only, and control were found based on two tailed student t-test. Significant difference ($p < 0.01$) was found between Au-NRs + Fs laser and control group, based on two tailed student t-test ($n=4$). Error bars represent standard deviation of the normalized values within the group.

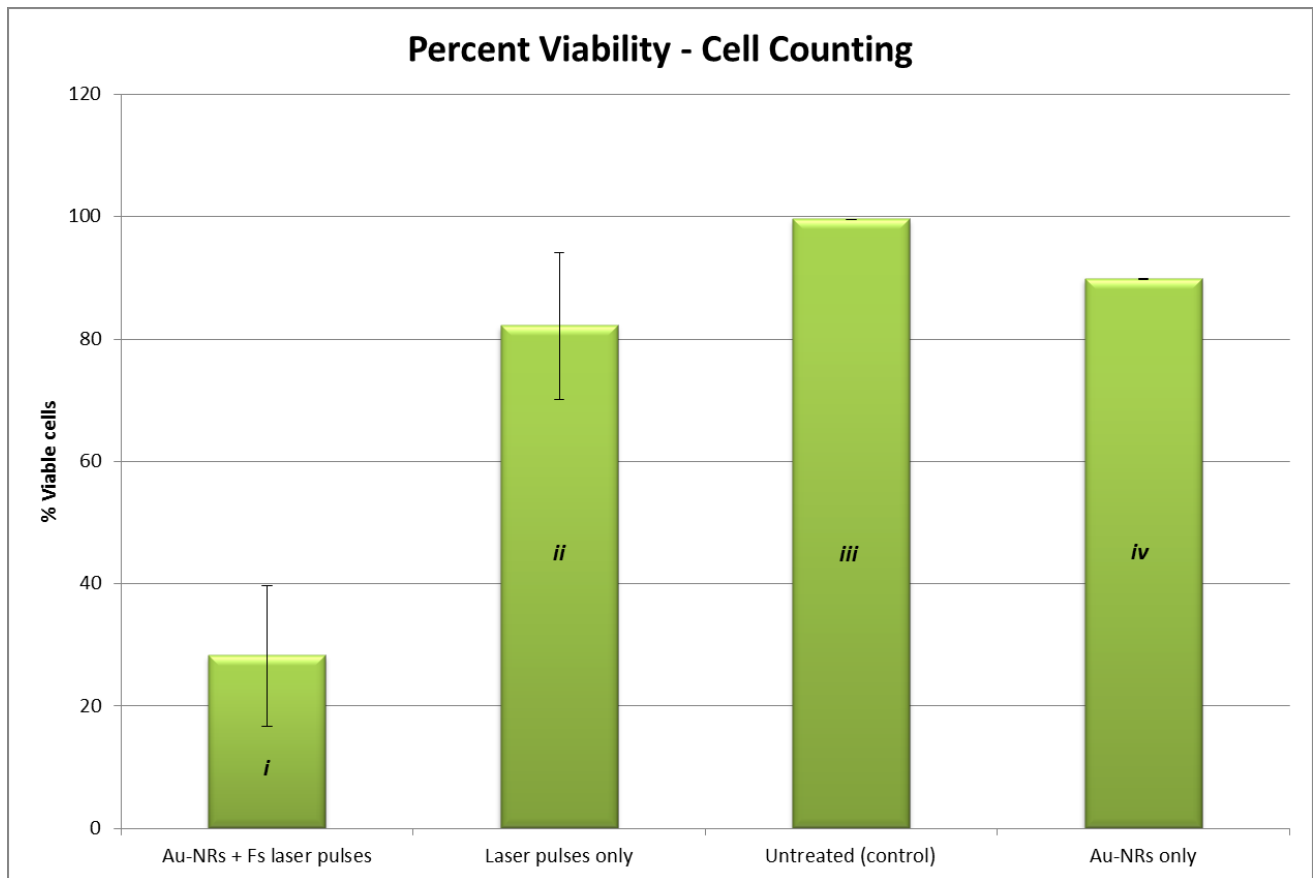


Figure 3.14: Cellular counting of fluorescence viability assay of retinoblastoma cells. No significant difference between laser pulse, Au-NRs only, and control were found based on two tailed student t-test. Significant difference ($p < 0.05$) was found between Au-NRs + Fs laser and control group, based on two tailed student t-test ($n=4$). Error bars represent standard deviation of the normalized values within the group.

3.4 Discussion and Conclusion

A series of tests to determine the optimal laser irradiation power, spot size and number of pulses required to ablate the highest number of retinoblastoma cells containing Au-NRs, while not affecting cells that do not contain Au-NRs, resulted in laser peak power of 1.45 TW/cm^2 . The laser pulse duration emitted from the laser amplifier source was measured as 35fs. However, due to the $4\times$ microscope objective lens the pulse duration was stretched to 55fs (see Appendix B).

Notably, this laser intensity level ($1.45\text{TW}/\text{cm}^2$) is below the irradiance level required to induce a critical free electron density to induce optical breakdown ($6.5\text{TW}/\text{cm}^2$) [7]. In order to evaluate the number of fs laser pulses required for melting of Au-NRs, the Au-NRs were suspended in deionized water and irradiated with a varying number (5, 10, 15, 25, 30, 35) of fs laser pulses. Figure 3.15 displays field emission scanning electron microscope (FESEM) images of Au-NRs under various fs pulse irradiation. For 5 laser pulses (sample shown in Figure 3.15a), 70% of the Au-NRs were melted. When the Au-NRs were irradiated with 10, 15 and 25 pulses (samples shown in Figure 3.15b, c and d), almost 100% of the Au-NRs are melted.

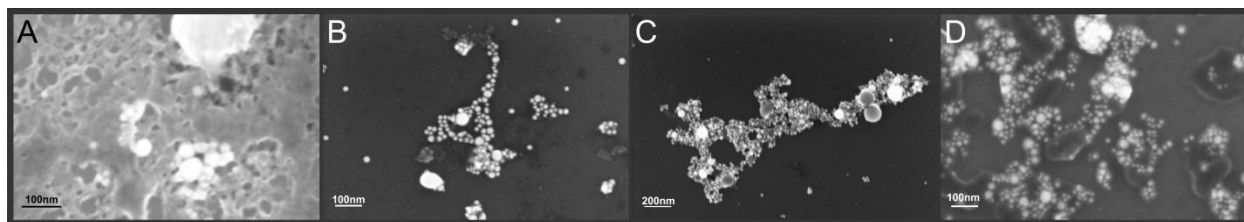


Figure 3.15: FESEM samples of melted Au-NRs due to fs laser pulse irradiation. When the Au-NRs were irradiated with **A.** 5 pulses **B.** 10 pulses **C.** 15 pulses and **D.** 25 pulses. Laser beam diameter of $400\mu\text{m}$ spot size. At the focal spot, the laser pulse train average power, energy, and intensity were: 50 mW, 50 $\mu\text{J}/\text{pulse}$, and $1.45\text{TW}/\text{cm}^2$, respectively.

As depicted in Figure 3.16A when Au-NRs are irradiated with transverse polarization its temperature can rise by only a few degrees, to $\sim 275\text{K}$. However, as seen in figures 3.16B and 3.16C, the Au-NRs that are illuminated with $1.45\text{TW}/\text{cm}^2$ at diagonal or longitudinal polarization can reach temperatures of 11,000K and 19,000K, respectively, which are higher than the melting temperature of bulk gold.

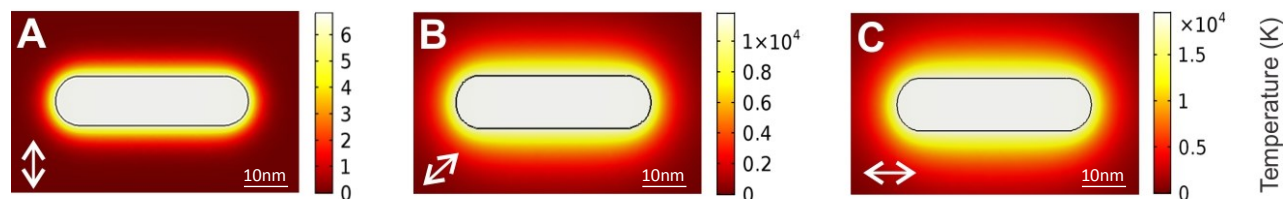


Figure 3.16: Temperature distribution calculations on Au-NR with a size of 11nm×43nm, irradiated with fs laser pulse of $\lambda_{\text{center}}=800\text{nm}$ and $1.45\text{TW}/\text{cm}^2$ for three incident fs laser pulse polarizations. **A.** Longitudinal polarization. **B.** Diagonal polarization. **C.** Transverse polarization. The arrow points at the direction of the polarization of the incident electric field E_0 .

As seen from Figure 3.14, the spatial distribution of the Au-NRs temperature in the water/medium around the Au-NRs drops very quickly to room temperature in a distance of only $\sim 10\text{nm}$ away from the Au-NRs. These results indicate that the thermal effects on the environment are confined to the Au-NRs and will not induce unwanted effects on neighboring cells. Notably, irradiation of retinoblastoma cells containing Au-NRs with 5 laser pulses resulted in only 40% cell death compared to 90% cell death when irradiated with 20 laser pulses. These results indicate that a minimum number of laser pulses is required in order to induce efficient cell death.

Nanoparticle-based therapies are challenging to implement in in-vivo applications, due to circulatory immune clearance. To overcome this barrier, the use of biocompatible coatings can reduce the clearance of the particles from the body by the immune system and prolong circulatory times, thereby enhancing therapeutic capacity [125,126]. Polyethylene glycol (PEG) is the most widely-used stealth coating and facilitates longer particle circulation [125,126]. In particular, PEGylated Au-NRs, which were used in our experiments, have been reported to evade immune system response and prolong circulatory times [125,126].

In conclusion, children who suffer from retinoblastoma can benefit greatly from the clinical application of a new modality of cancer specific retinoblastoma treatment. This study demonstrated that it would be possible to use Au-NRs and femtosecond pulse lasers to target retinoblastoma cells. It was noted that the eye has minimal absorption or scattering at a wavelength $\lambda=800\text{nm}$, which is required to induce heating and ablation of the cells filled with Au-NRs. Retinoblastoma targeting Au-NRs can be injected into the eye, and the femtosecond laser pulses can be delivered externally onto the innermost layer of the eye, the retina. This will result in selective destruction of cancer cells alone while sparing healthy cells. Furthermore, the clinical translation of these proof-of-concept results could result in a treatment that would not only save children's lives, but would also allow for the preservation of their vision.

Chapter 4

Femtosecond Laser-Induced Cell-Cell Surgical Attachment^{4,5}

⁴ Portions of this chapter have been published in: Katchinskiy et al. Femtosecond laser-induced cell-cell surgical attachment. *Lasers Surg Med* 2014 April 01;46(4):335-341.

⁵ Portions of this chapter have been published in: Katchinskiy et al. Characterization of femtosecond-laser pulse induced cell membrane nanosurgical attachment. *Biomed Opt Express* 2016 June 22;7(7):2749-2758.

4.1 Introduction

Tissue is formed by the natural ability of cells to adhere to each other. Cellular self-adhesion is a selective process, whereby cells only attach to specific cell types [127]. Interruption of the structural integrity of a tissue occurs during injury, and cells detach from each other. The natural healing process involves secretion of inflammation factors and triggers a sequence of biochemical reactions resulting in the creation of scar tissue which in turn may prevent recovery of the full functional capacity of the tissue in terms of direct and smooth cell connectivity. In delicate surgical interventions, such as nerve coaptation, blood vessel anastomosis, tendon repairs, as well as cosmetic surgeries, scarring must be minimized. Scarring in nerve coaptation can prevent the secretion of nerve growth factors and interrupt the transmission and propagation of electrical signals along the nerve axons [128]. Suturing of blood vessels can cause scar tissue formation and can lead to formation of weak vessels that are prone to clot formation [129,130]. Scarring of tendons may limit the passive and active range of motion of the joint [131].

Selective attachment of cells has recently become an important application for the pharmaceutical and biomedical industries. Tissue and cell culture engineering are necessary for the synthesis of new medications [132]. Carbohydrates and proteins have recently been synthesized from organisms, such as bacteria and yeast [133], making the production of protein-based medications feasible [132].

Many important cell types cannot be cultured in suspension, as they require physical attachment to other cells as well as scaffolding. The most commonly used cell cultures are cells that are grown in suspension which are more susceptible to transformations, that may in turn, create disequilibrium and relative instability in cell cycle and growth. Some of these biochemically abnormal metabolic pathways were previously described in malignant transformation of cells

[132,134]. Despite the innovation in these industrial processes, there are concerns raised in using transformed cell lines for synthesis of medications. Cell transformation is reported to result in abnormal metabolic processes leading to abnormally structured proteins that in turn increase the biological risk in using them for medical purposes [135]. An application requiring cells for synthesis of organic compounds will benefit from utilizing natural cell lines as a platform for organic substance extraction.

The ability to precisely manipulate the cellular membrane without interfering with the internal structures of the cell has important implications for cellular biology research, tissue engineering, and the creation of cell-based therapeutics. The cellular membrane is made of a phospholipid bilayer, which surrounds the cytoplasm of living cells, thereby holding the contents of the cell and physically separating the intracellular components from the extracellular environment [81]. As discussed in section 2.20 of Chapter 2, the cellular membrane has important roles acting as the “gateway” into and out of the cell [81], regulating what material can enter and exit the cells, maintaining a membrane potential, determining the shape of the cells by anchoring the cellular cytoskeleton [81], and it is also responsible for attachment of the cell to neighboring cells and to the extracellular matrix [81]. Finally, the cell membrane binds cellular structures such as the plasma membrane proteins, lipids, carbohydrates, and complex structures such as cilia [81].

The ability to manipulate these membrane structures is extremely important for cancer research. For example, the expression level of plasma proteins is significantly altered in various cancer types [136]. Increasing/decreasing plasma protein levels without modifying the internal parts of the cell would allow researchers to understand how these proteins affect the behavior of these cells, and potentially open up new doorways to the production of patient-specific cancer therapies.

A tool that can precisely manipulate the cellular membrane without destroying the integrity of the internal structure of the cell is key for studying the cellular membrane. In order to perform studies in a controlled environment, one would need to modify the cellular membrane without the introduction of external material into the cell, that is, without porating the cell during the procedure.

In recent years, femtosecond laser pulses have emerged as an enabling tool for non-invasive manipulation of living biological systems and for modifying molecules, by introducing and removing cellular material within the cellular environment. When near-infrared femtosecond laser pulses interact with tissue, multiphoton absorption of the photons takes place in the time scale corresponding to the pulse duration [7,53]. The electron density can grow exponentially leading to avalanche ionization process [7,53]. Tissue manipulation using femtosecond laser pulses takes place due to chemical process (i.e. material ionization) of the material due to the high concentration of free-electron distribution at the focal spot, and not due a thermal breakdown of the material [7,53]. Hence, this makes femtosecond laser pulses an excellent tool to precisely manipulate tissue without causing thermal damage [7,53]. Some of these applications include cell ablation [137], cell isolation [4], cell nanosurgery [4], reversible optical perforation/cell transfection [5,6,138,139], and cell-cell fusion [140].

In cell-cell fusion, the cellular membranes are merged, resulting in transfer of the cellular cytoplasm, thereby creating a single cellular entity encompassed by a common membrane. Cell-cell fusion occurs after relatively long exposure time to the laser pulse with a relatively low yield [98,140-142]. Other methods of cell-cell fusion have been discussed in chapter 2, section 2.21 cellular fusion and hemifusion. A key application of femtosecond laser interaction with live cells is the ability to perform surgery on the surface of the cell membrane to facilitate cell-cell

attachment without destroying the integrity of the cellular internal molecular layer. This requires a precise alteration of the external layer only and maintaining the isolation of the cells from the surrounding medium during the attachment. Therefore, it is necessary to perform precise ablation of the phospholipid bilayer, minimize cavitation bubble formation, as well as heat deposition, and allowing for the formation of new molecular bonds.

Purpose of this study

This chapter explores the application of femtosecond laser pulses as an alternative tool for cell-cell surgical attachment. This technique is based on the use of ultrashort near-infrared laser pulses that precisely alters the phospholipid cell membranes of two adjacent cells and induces reformation of molecular bonds between their membranes. Employing this revolutionary technology allows for surgical attachment of cell membranes, while preserving the cellular integrity. The model system chosen to demonstrate cell-cell attachment was Y79 retinoblastoma cell line. This cell line was used for the reasons stated in section 3.2.1 of chapter 3, as the cells grow in suspension and are possible to control individually.

Additionally, in the following chapter, further evidence to support the hemifusion hypothesis is provided via TEM images of the contact region between two attached retinoblastoma cells. For this purpose, a technique of tracking individual cells during cell processing for TEM imaging was developed. The cells were attached using femtosecond laser pulses, in an effort to demonstrate that the cell membrane phospholipid layers hemifused.

4.2 Experimental Methodology

4.2.1 Cell Suspension

Y79 retinoblastoma cells which grow in suspension were used to demonstrate laser induced cell-cell attachment. The cells were cultured in Dulbecco's modified Eagle medium supplemented

with 10% fetal bovine serum. For experimental manipulations, approximately 5 million cells were washed three times in 10 ml Dulbecco's Phosphate-Buffered Saline (DPBS) solution (Sigma). Half of the cells (in 5 ml DPBS) were set aside and half of the cells were stained with 2.5 ml of 3 μ M Calcein AM diluted in DPBS. Cells were allowed to incubate for 30 minutes. After incubation was complete, the cells were washed three times with 10 ml of DPBS solution in order to remove the remaining Calcein AM in the solution. The cells were then re-suspended in 5 ml DPBS. Finally, the two 5ml tubes of stained and unstained cells were mixed together. For viability testing, the Y79 retinoblastoma cells were stained with propidium iodide (PI) solution. Five ml of Y79 cells were washed three times with 10 ml DPBS solution. A final wash was completed with 3 ml of DPBS. The cells were mixed with 2 ml of 3 μ M PI.

4.2.2 Setup Characteristics

The cell-cell surgical attachment was achieved by using sub-10 femtosecond laser pulses, with 800 nm central wavelength that was delivered from a Ti:Sapphire laser oscillator at a repetition rate of 80 MHz. The ultrashort pulses were coupled to an upright Nikon Eclipse 80i optical microscope and directed towards the cells. In order to image the cells and to focus the laser beam, a 60 \times (NA =1) water immersion microscope objective was used. A high NA microscope objective was required to achieve high-resolution imaging and to produce an effective laser beam spot size of ≤ 800 nm, and depth of focus of 2 μ m. At the focal spot, the optimum laser pulse train average power, energy, and intensity were found to be: 200 mW, 2.5 nJ per pulse, and 1.71×10^{12} Wcm⁻², respectively. Optimal irradiation duration was found to be 15 ms (1.2 million pulses). The cell-cell surgical attachment procedure was imaged and recorded in real-time using a color charge-coupled device (CCD) camera. The images were taken from the video recordings after the completion of the experiment.

4.2.3 Experimental Procedure

Y79 retinoblastoma cells were placed inside a glass dish mounted on a motorized x-y-z nano-translation stage for precise movement control of the cell culture. The microscope was first set to a fluorescence imaging mode in order to identify a group of fluorescent and non-fluorescent cells. Once the cells were identified, the microscope was switched to bright field imaging mode. The fluorescent and non-fluorescent cells were brought into contact using an optical tweezer which is made collinear with the femtosecond laser pulse train. Once the desired contact region between the cell membranes was identified, it is precisely targeted by the femtosecond laser pulse train for a duration of 15 ms. In order to verify that the cells did not go through a cell-fusion process, (i.e. the cytoplasm of both cells did not mix), the microscope was set to the fluorescence imaging mode and it was verified that the fluorescent dye did not migrate from the dyed cell to the non-dyed cell. The mechanical integrity of the attached joint was then assessed using an optical tweezer. This was achieved by trapping a single cell to the optical tweezer's focal spot, and moving the trapped cell(s) in various paths. In order to verify that physical attachment was obtained, three criteria were assessed: (1) movement of all cells as a single unit, (2) movement of all cells due to trapping of any cell in the group, and (3) no detachment due to twisting, and drag forces. We confirmed the physical cellular attachment by following the translation of the trapped cell as an integral unit together with the other cells without detaching from each other. In order to verify that the attached cells did not move due to their proximity to the optical trap, multiple cells were attached in a row. This method enabled us to ensure that the cells that were located far enough from the optical trapping spot, where the attraction forces to the laser tweezers are too weak to pull an individual cell, are still moving due to cellular attachment forces.

4.2.4 TEM Preparation

4.2.4.1 Reagents:

- 1) Fixative: 2% Paraformaldehyde (Sigma) and 2.5% Glutaraldehyde (Electron Microscopy Sciences) in Phosphate Buffer (PB) for routine TEM
- 2) PB: 0.1 M phosphate buffer pH 7.3
- 3) 1% OsO₄ /0.1 M phosphate buffer
- 4) 1% carbohydrazide (Sigma) in ddH₂O
- 5) ddH₂O
- 6) Graded series of ethanol 30% 50% 70% 95% and 100%

4.2.4.2 Fixation:

The culture medium was carefully removed from the culture dish, and fixative solution was added at 37°C. The cells were left at 37°C for 30 min in the fixative and then left at room temperature for an additional 40 min. The cells were rinsed with 0.1 M PB 3 times for 5 min at room temperature. Post-fixation was done in 1% OsO₄/0.1M PB for 15 min, and then rinsed with PB 5 times for 5 min. The cells were incubated in 1% carbohydrazide solution (in H₂O) at room temperature for 10 minutes, then rinsed with ddH₂O 5 times for 5 min. The cells were incubated again in 1% OsO₄/0.1 M PB for 1 hr, then rinsed with ddH₂O 3 times for 5 min.

4.2.4.3 Dehydration:

The cells were dehydrated with 30%, 50%, 70% EtOH for 10 min each and block stained with 1% Uranyl acetate in 70% EtOH for 30 min at room temperature. Finally, the cells were dehydrated with 95% EtOH for 5 min, and 3 times in 100% EtOH for 5 min.

4.2.4.4 Resin infiltration:

The sample was infiltrated with Spurr's: 100% EtOH with a ratio of 1:1 for 1 hr, then infiltrated with Spurr's: 100% EtOH with a ratio of 3:1 for 1 hr. Finally, the sample was infiltrated with 100% Spurr's for 1 hr. The infiltrated cells were polymerized at 65°-70°C.

4.2.4.5 Sectioning:

The location of the cells was found based on the recorded location on the grid. The perimeter around the required cells was cut and sectioned to 70 nm thick slices (z-slices), and mounted on TEM grid for imaging. The z-slices were taken parallel to the original plane of observation.

4.3 Results

The capabilities of the femtosecond laser-induced cell-cell surgical attachment were demonstrated through two, three, and five cells attachments. Figure 4.1 presents an attachment of two cells. In figure 4.1(A), a fluorescent cell (i) and a non-fluorescent cell (ii) are identified. The two cells are brought into contact using an optical tweezer and a femtosecond pulse is delivered to the contact point between the cell membranes, as depicted in figure 4.1(B). The dark spot shown in this figure is the cavitation bubble which was temporarily formed due to breakdown of the outer phospholipid layer of the cell membrane and the DPBS solution. This spot allows for the visualization of the laser attachment location. In figure 4.1(C), the physical attachment of the cells is shown after the dissipation of the cavitation bubble. Clearly, the cell membranes are intact, and appear to be in physical contact. To ensure that the cytoplasm of the cells did not transfer due to cell fusion, a fluorescent image was taken and provided in figure 4.1(D). The round structure and boundaries of the fluorescent cell are well defined, and match the bright field image of figure 4.1(C). As such, it can be concluded that the cytoplasm of the fluorescent and the non-fluorescent cells did not transfer during the attachment procedure. Furthermore, physical

attachment was verified by movement of the two cells in a circular motion using the optical tweezer. It was observed that both cells followed a corresponding path, twisted, and rotated as a single entity, without showing any sign of detachment. Therefore, it was determined that the cells are physically attached. Figure 4.1(E) captures the two cells oriented approximately 45° relative to their original orientation.

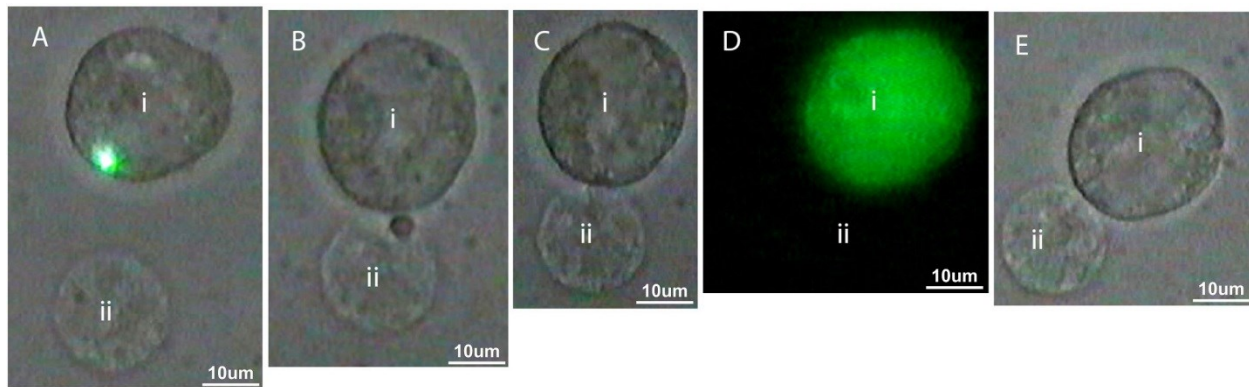


Figure 4.1: **A.** A fluorescent cell (i) and a non-fluorescent cell (ii) are identified. The fluorescent cell is identified through its fluorescence due to multi-photon absorption of the laser pulse as shown by the bright green light emission spot. **B.** Cells are brought into contact using an optical tweezer, and femtosecond laser pulse is delivered to the contact location. The dark spot at the boundary between the two cells is due to the formation of a cavitation bubble. **C.** cells (i and ii) observed post-attachment. **D.** Fluorescence imaging of the two cells. Only cell (i) is fluorescing. **E.** Verification of cell membrane physical attachment where the cells are oriented $\sim 45^\circ$ relative to original orientation.

Figure 4.2 depicts an example of femtosecond laser-induced attachment of three cells arranged in a linear fashion. Similarly, the cytoplasm of the fluorescent and the non-fluorescent cells did not transfer during the attachment procedure and the cells are physically attached.

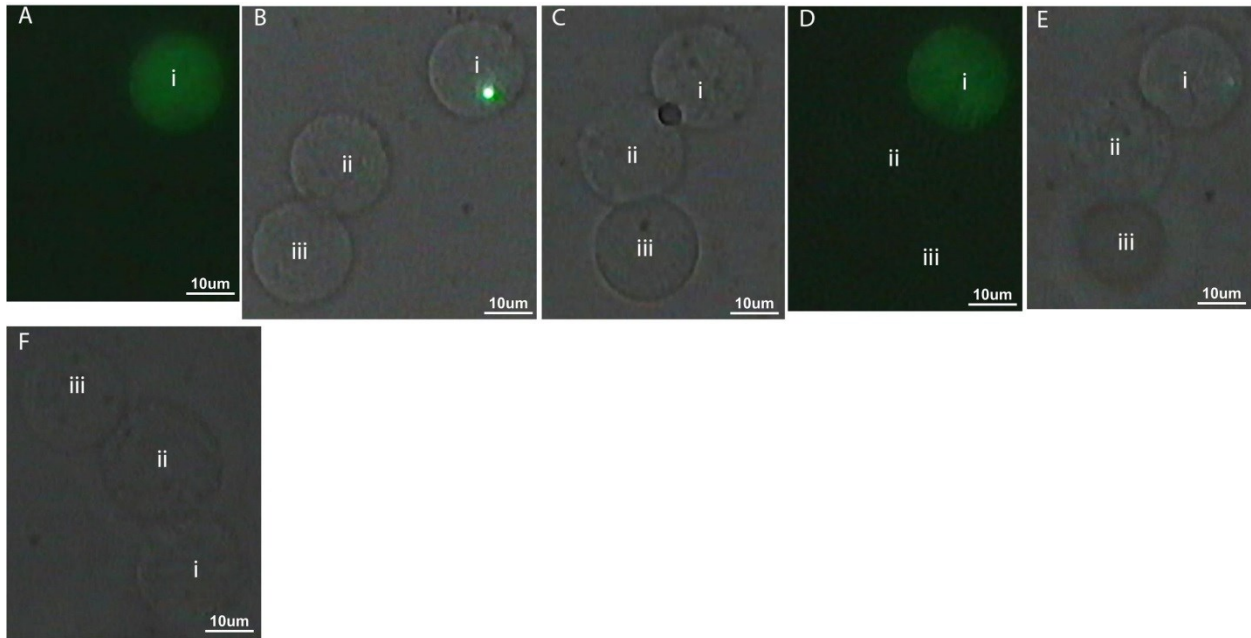


Figure 4.2: **A.** A fluorescent cell (i) is identified. **B.** The fluorescent and two non-fluorescent cells (ii and iii) are identified under bright field view. **C.** Femtosecond laser pulse is delivered to the contact location. The dark spot at the boundary between the two cells is due to the formation of a cavitation bubble. **D.** Under fluorescence imaging, it is identified that the cytoplasm of the dyed cell did not transfer to the attached cell. **E.** under bright field imaging, cells are identified as physically attached. The cells are intact, and in close proximity to each other. **F.** Physical attachment was verified: the cells were pulled in a circular path. The cells are captured while being oriented at 180° relative to their original position.

The potential to apply this technique to any number of cells is demonstrated by the attachment of five cells, as shown in figure 4.3. Furthermore, the versatility of femtosecond laser induced cell-cell surgical attachment is confirmed by its ability to attach a single cell at multiple locations. Attachment of single cell at multiple locations is a fundamental requirement for the creation of engineered tissue, as it allows for the formation of 2D and 3D structures. In this arrangement, a fluorescent cell (i) is identified under fluorescence imaging, and under bright field imaging, the cell is identified to be pre-attached to a non-fluorescent cell (ii). Additionally, two non-

fluorescent cells (iii and iv) are identified below cell (i), and a non-fluorescent cell (v) is identified to the left of cell (ii). Using the same experimental parameters as previously discussed, the fluorescent cell (i) was attached to cell (iii), cell (iii) was attached to cell (iv), and cell (ii) was attached to cell (v).

To examine the torsional and tensile strengths of these attachments, the cells were arranged in an L-shape pattern in order to provide two anchoring points for the optical tweezer. The resting angle of the L-shape pattern was measured to be 92° (Figure 4.3(F)). During circular twisting of the cells, they experienced drag force, caused by the surrounding medium. As depicted in figure 4.3(H), the five cells bent, forming an L-shape arrangement at a steeper angle of 76° , and rotated as a group. This suggests that the tensile and torsional strengths of the formed attachment can withstand large forces, while preserving the ability of the cell membranes to flex.

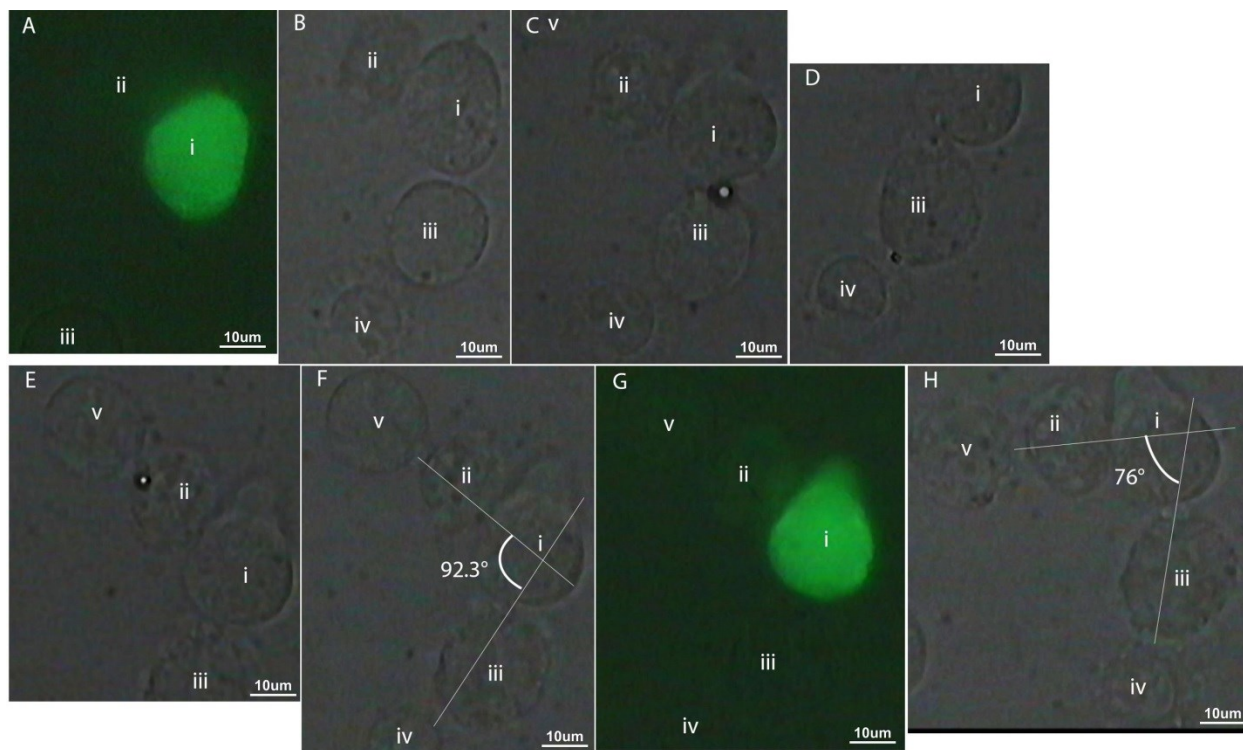


Figure 4.3: **A.** A fluorescent cell (i) is identified. **B.** Fluorescent cell (i) is pre-attached to a non-fluorescent cell (ii). Two non-fluorescent cells (iii and iv) are located below cell (i). **C.** Fluorescent cell (i) is attached to the non-fluorescent cell (iii). The bright spot at the boundary between the two cells is the reflected light emitted from the femtosecond laser pulse. **D.** The non-fluorescent cell (iii) is attached to the non-fluorescent cell (iv). **E.** The non-fluorescent cell (ii) is attached to the non-fluorescent cell (v). **F.** Under bright field imaging, cells are identified as physically attached. The cells are intact, and in close proximity to each other. **G.** Under fluorescence imaging, it is identified that the cytoplasm of the dyed cell did not transfer to the attached cell. **H.** Physical attachment was verified: the cells were pulled in a circular path. The cells are captured while being rotated relative to their original position.

4.4 Discussion

The integrity of any tissue is a mandatory feature in ensuring its functional biological capacity [127]. Scar tissue formation may negatively impact the natural qualities of tissues. Delicate

surgical interventions aspire to minimizing secondary tissue injury due to the procedure itself. Some tissues, such as neural cells are highly sensitive to injury as their regenerative abilities are more limited [128]. Scar tissue in other biological systems such as the cardiovascular system may result in secondary medical damage through clot formation and further ischemic insult to the entire organ and organism [129]. Current technologies are using transformed cell lines in producing organic substances needed for different pharmaceutical purposes [132]. The transformed cell cultures exhibit a higher percentage of abnormal proteins due to incomplete and altered metabolic processes raising the suspicion that the synthesized proteins are not necessarily safe to a living biological system [135]. Malignant growths display similar aberrant metabolic alterations [134].

Preserving the integrity of cells post injury and utilizing less harmful techniques are mandatory in order to prevent the above mentioned secondary damages. Femtosecond laser-induced surgical attachment of cells enables cell adherence without rupturing the cellular membranes. It is showed that the cells attach to each other without any exchange in cytoplasmic material. It is our assumption that cells adhered only at the surface level of the cell membranes. This strong attachment is probably molecular in nature, and we propose a model to explain the observed experimental results.

4.4.1 Cell-Cell Attachment Model

As discussed in section 2.20 of Chapter 2, the membrane's phospholipid bilayer is naturally organized in a way that the nonpolar (hydrophobic) tails of the molecules are projecting to the interior, and the polar (hydrophilic) ends of the molecules, project outward. Due to this assembly, the hydrophilic layer of the membrane is permeable to certain ions and molecules. It is postulated that exposure to femtosecond laser pulses impacts rearrangement of the phospholipid

bilayer (figure 4.4(A)). For near-infrared femtosecond laser pulse excitation, multiphoton absorption of the photons occurs on the time scale corresponding to the duration of the pulse. This exposure time is much shorter than the time scale of electron-ion (or neutral atom) energy transfer and the thermal diffusion time. Thus, the electronic excitation is efficiently decoupled from the thermal relaxation process where energetic electrons are created locally before they can transfer their energy to the surrounding. Above certain laser pulse intensity threshold, the electron density grows exponentially since electrons ionized at the leading edge of the femtosecond laser, initiating a self-seeding avalanche ionization process.

Both multiphoton ionization and avalanche ionization produce a high density of electrons and ions which destabilize and possibly lead to ultrafast reversible destabilization of the phospholipid molecules, as depicted in figure 4.4(B). The ionization process occurs across the location of the peak intensity of the laser focal spot, which is much smaller than the laser diffraction limited full width half maximum (FWHM) spot. The laser's FWHM spot size is larger than the membrane thickness and the phospholipid layers are destabilized across the entire laser spot. Since the membrane's exterior surface is permeable to both photo-induced ions and electrons, these can cross over to the central nonpolar region and break the bonds of the fatty acid tails, as illustrated in figure 4.4(C). Nonetheless, the destabilization process is reversible everywhere. At the end of the photoexcitation process, the ionized molecules seek equilibrium state, and form new bonds with nearby ions. Notably, when positioning the laser spot on the contact point between the cells, only the phospholipid molecules which are located at the cell membrane contact point cross-link with phospholipid molecules of the adjacent cell membrane; due to their close proximity. This cross-linking process results in a single phospholipid bilayer, which is shared by both cells (figure 4.4(D)). However, destabilized phospholipids that are not in contact with the other cell

are too far apart to cross-link. Thus, the unstable phospholipids link back (revert back) to form their original structure.

The proposed mechanism for cell-cell attachment is not different from what is already known in cell biology as hemifusion [101], which was discussed in section 2.21 of Chapter 2. In this chapter, hemifusion process was induced via a femtosecond laser pulse rather than a chemical process. On Retinoblastoma cells, membrane ablation (i.e. material removal) occurs at a threshold intensity of $2.6 \times 10^{12} \text{ Wcm}^{-2}$, whereas cell-cell attachment occurs at much lower intensity of $1.7 \times 10^{12} \text{ Wcm}^{-2}$. As such, no ‘material removal or ablation’ takes place at an intensity of $1.7 \times 10^{12} \text{ Wcm}^{-2}$. To access this ‘ultrafast reversible destabilization regime’, precise control of the laser intensity and aiming accuracy of $1.7(\pm 0.08) \times 10^{12} \text{ Wcm}^{-2}$, and $\pm 0.5 \mu\text{m}$ within the cell contact point are required to achieve optimum cell-cell attachment. It was observed that when moving the laser spot away from the cell-cell contact point onto random locations on either cell membrane, no morphological change (ablation, portion, etc.) was observed. This is understood because the intensity is not high enough to cause any damage to the cell membrane. This model supports our findings of non-transferred cytoplasm during and after exposure to the femtosecond laser pulses.

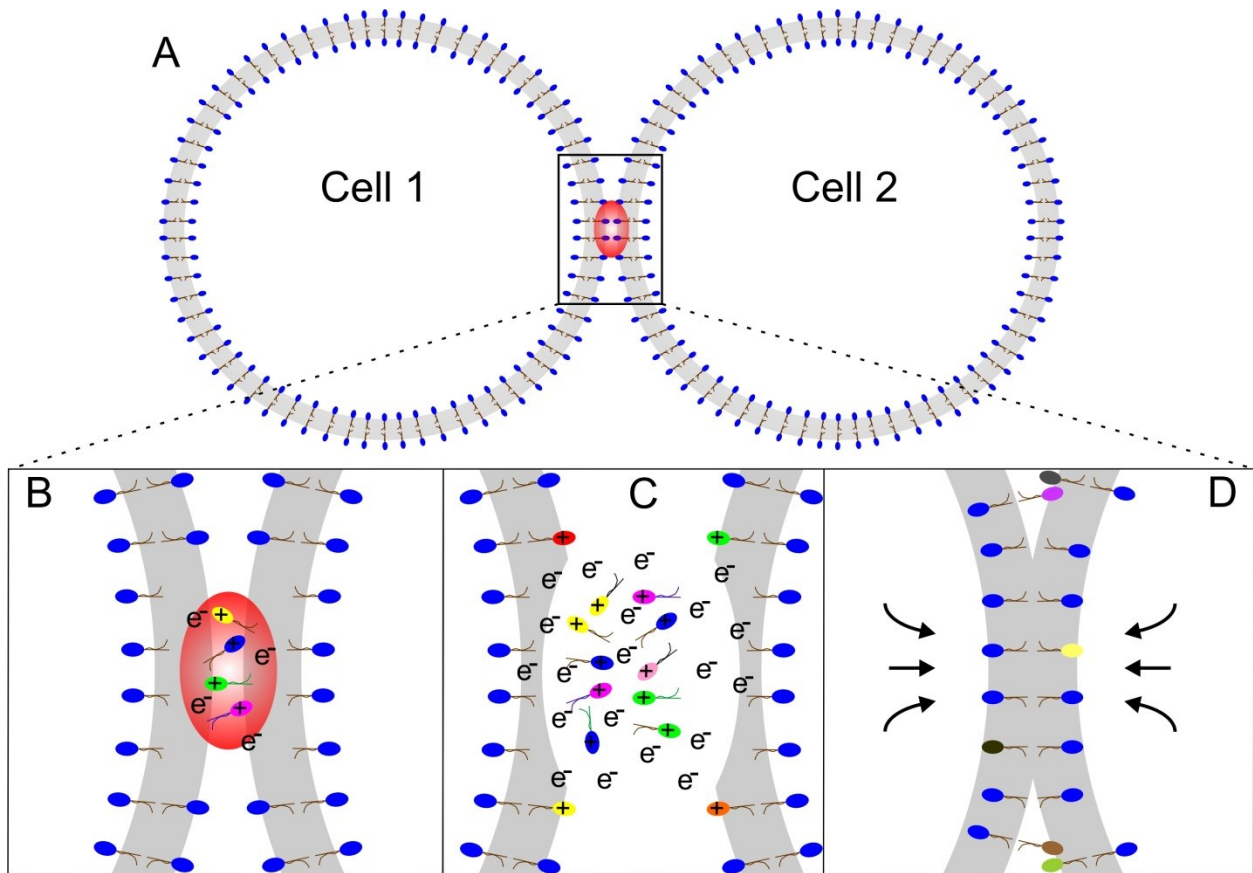


Figure 4.4: **A.** A femtosecond laser pulse is delivered to the target point between the cell membranes. **B.**

The high laser pulse intensity at the focal point causes a reversible breakdown or a precise ablation of the outer phospholipid layer. **C.** Energetic ions and electrons cross the center nonpolar region and break additional bonds between the fatty acid tails. **D.** The relaxation process results in the formation of new stable bonds and formation of singular cell membrane only at the connection point.

4.4.2 Cell-Cell Attachment Efficiency

During experiments, several pairs or groups of cells were attached in order to demonstrate the capabilities of this technology. It was observed that in 90% of the attachments, one to two 15ms intervals of laser beam treatments were necessary to achieve attachment. Nonetheless, excessive laser pulse illuminations can create reversible pores in the cells' membranes. It was found that 95% of the cell attachment procedures performed were successful. The experiments were performed approximately 4 hours at a time. During this time period the cells remained firmly attached without showing signs of deterioration in attachment strength. The average time taken to complete cell-cell attachment is 30ms, limited only by the slow movement of the optical tweezer. However, such a process can be further improved by automation of the laser tweezers or by the use of multiple optical traps in parallel.

4.5 Conclusion

In this chapter it was demonstrated that attachment of single cells using femtosecond laser pulses is possible with efficiency of 95%, while preserving the cells' viability. Laser-induced ionization process resulted in an ultrafast reversible destabilization of the phospholipid layer. The cellular cytoplasm remained in isolation from the surrounding medium during and after the attachment procedure. It was determined that the required laser intensity and accuracy for optimum cell-cell attachment are $1.7(\pm 0.08) \times 10^{12} \text{ Wcm}^{-2}$, and $0.5\mu\text{m}$ within the contact point. A strong physical attachment between the cells was obtained possibly due to the bonding of ionized phospholipid molecules and the formation of a single, joint, cell membrane at the connection point. A future evaluation of the attachment force may be feasible with precisely calibrated dual-beam optical tweezer, and with a knowledge of the drag and frictional forces, and the membrane electrostatic charges. It is suggested that this process allows cell-cell attachment, while avoiding disruption of

cell membranes, and without the induction of cell-cell fusion. Femtosecond laser-induced cell-cell surgical attachment can potentially provide an efficient and safe technique for the creation of engineered tissue and cell cultures. This innovative procedure can be further implemented in surgical interventions that require artificially made tissue.

4.6 Characterization of Hemifusion

At the discussion, section 4.5, the application of femtosecond laser pulses to precisely manipulate the external phospholipid molecules of a cellular membrane in order to perform cell-cell surgical attachment was discussed. It was hypothesized that when a femtosecond laser pulse is delivered to the contact point between the cell membranes, the high laser pulse intensity results in ultrafast reversible destabilization of the phospholipid molecules. The phospholipid molecules quickly reattach to form a single shared membrane between the cells.

4.6.1 Characterization Results

TEM images of cellular membranes in a group of retinoblastoma cells that were left to naturally attach are depicted in figure 4.5. Under low magnification (figures 4.5A, 4.5B), the outline of each cell is clearly visible. Under high magnification, as shown in figures 4.5C and 4.5D, the membranes are easily distinguishable and separated by a consistent 10-20 nm gap. These findings affirm that for retinoblastoma cells, at a location where the cells are left to naturally attach, the cell membranes are situated 10-20 nm apart throughout the entire length of attachment. This gap consists of the extracellular matrix which contains a cluster of molecules secreted by the cells, which provide chemical and structural support for the cells [143].

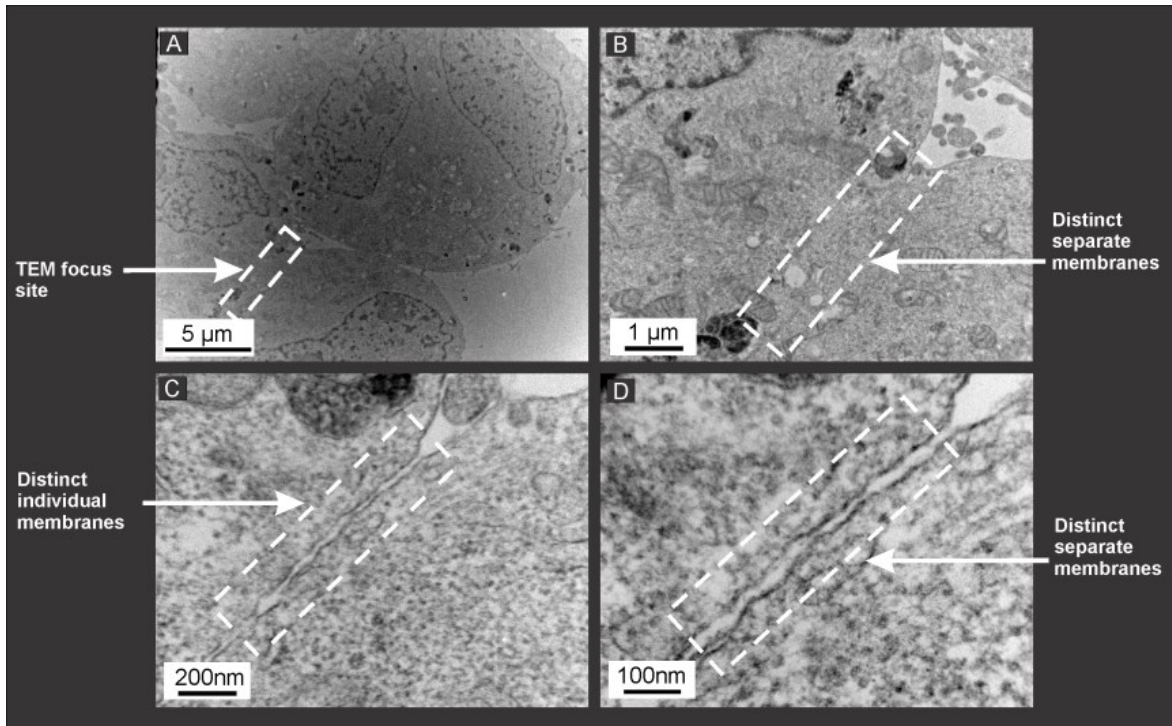


Figure 4.5: TEM images of cellular membranes of a group of retinoblastoma cells that were left to naturally attach, in order of increasing magnification from **A-D**. A small gap of 10 to 20 nm separates between the two phospholipid cell membranes throughout the entire attachment region.

In order to demonstrate the differences in the structure of naturally attached cell membranes and the femtosecond laser-hemifused membranes, three retinoblastoma cells were brought into close proximity to each other using an optical tweezer. One cell was selected for targeting where one end of its membrane was femtosecond laser pulse hemifused to one cell and the other end was allowed to naturally attach to a different cell. These three cells are depicted in figure 4.6 under light microscopy, after the femtosecond laser pulse hemifusion procedure was completed. As shown in figure 4.6, cells (i) and (ii) were femtosecond laser pulse hemifused to each other, and cells (ii) and (iii) were naturally attached to each other. Note that the out of focus cell (iv) is not attached to any of the cells and is situated underneath. By performing natural attachment and femtosecond laser pulse hemifusion on the same cell, it was possible to contrast the differences

between the structure of naturally attached cell membranes and the femtosecond laser pulse hemifused membranes on the same cell. A key advantage of using the same cell for both natural attachment and femtosecond laser pulse hemifusion is the elimination of any structural and behavioral variations between cells. Additionally, both sites of attachments can be imaged in the same TEM slice, which guarantees the same imaging, staining and handling conditions; thus, eliminating any discrepancies that may arise from using different TEM slices or imaging conditions.

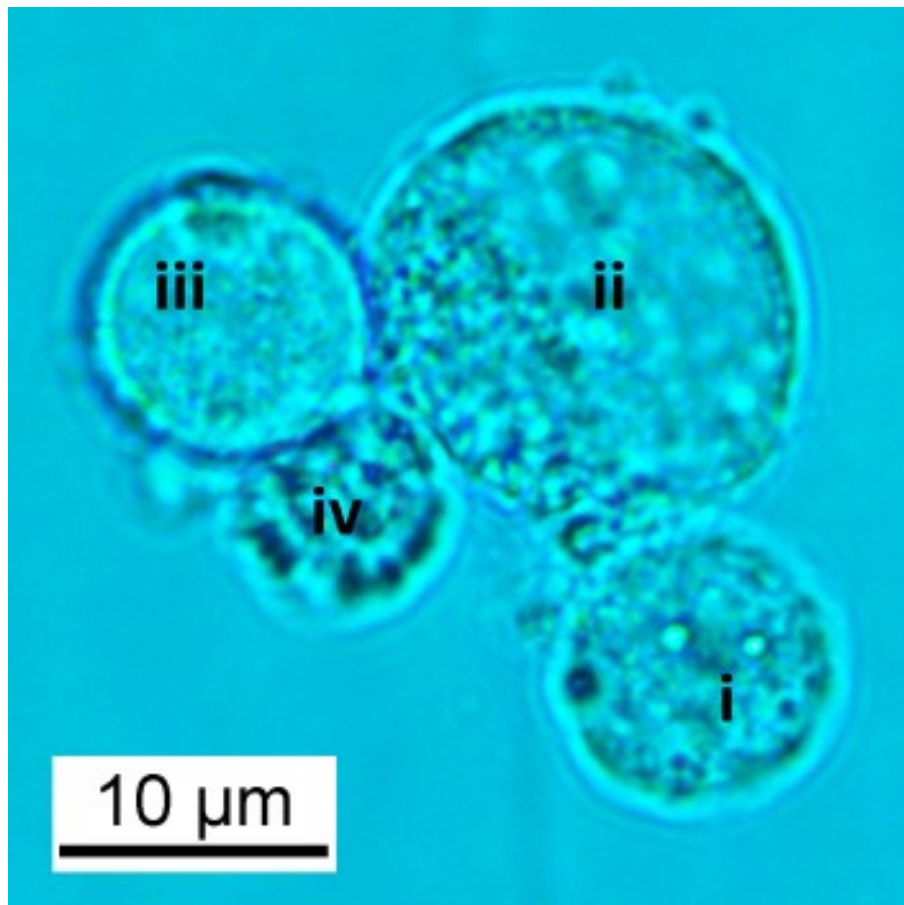


Figure 4.6: Bright field microscope image of four retinoblastoma cells after performing the laser-induced hemifusion procedure on cell (i) and cell (ii). Cell (ii) is allowed to attach naturally to cell (iii). The out of focus cell (iv) is located underneath the rest of cells and is not attached to any of the cells.

Figure 4.7 depicts the TEM images of the cells presented in figure 4.6. Note that only three cells are seen in figure 4.7, since cell (iv) (in figure 4.6) is located underneath the three manipulated cells and, thus, is not in the 70 nm thick TEM slice plane. A low magnification TEM image of the cells is shown in figure 4.7A, where the two separate membranes are apparent at the site of natural attachment. The membrane structure at the natural attachment region is acutely different compared to the membrane structure of the femtosecond laser pulse hemifused region. Shown in figures 4.7B and 4.7C are higher magnification TEM images of two different areas of the naturally attached membrane regions, with membranes highlighted with a transparent blue line to assist the reader with locating the cell membranes. Clearly, these images reveal that the naturally attached membranes are separated by a 10-20 nm gap throughout the entire length of the contact region, indicating that each cell's membrane remained intact and separate with its own phospholipid bilayer, as expected. However, high magnification images of the femtosecond laser pulse hemifusion site reveal that the two membranes converge to one single phospholipid bilayer. The entire region of the femtosecond laser pulse hemifusion was examined under high magnification, and the top, middle, and bottom sections are shown in figures 4.7D, 4.7E, and 4.7F, respectively. In figures 4.7D and 4.7F, the top and bottom edges of the laser induced hemifusion region are shown where the two cell membranes coalesce into a single cell membrane interface. At the central region of the hemifused membrane, hemifusion took place along most of the interface, as shown in figure 4.7E. In some regions, hemifusion did not take place (as seen in figure 4.7E), where gaps remain in between the two cells. This non-uniformity in hemifusion stems from the natural non-uniformity of the cellular membrane. The cell membranes are uneven surfaces that contain proteins and saccharides which prevent the cells from coming into close contact. Thus, it is possible that these sections of the cell membranes are

too far apart to fuse during the application of the femtosecond laser pulses. Proteins, saccharides, or water molecules might also interfere with the fusion process by accumulating in certain sections, thereby separating between the two membranes and not allowing the process of hemifusion to take place. Additionally, the laser intensity across the region of attachment is non-uniform due to random events such as diffraction, reflection, and varying multiphoton absorption processes. Therefore, some phospholipid molecules might not be ionized, and remain in their original bound formation. At regions where the cells were in close proximity to each other, on the other hand, the phospholipid membranes hemifuse to form a single membrane with a joint phospholipid bilayer.

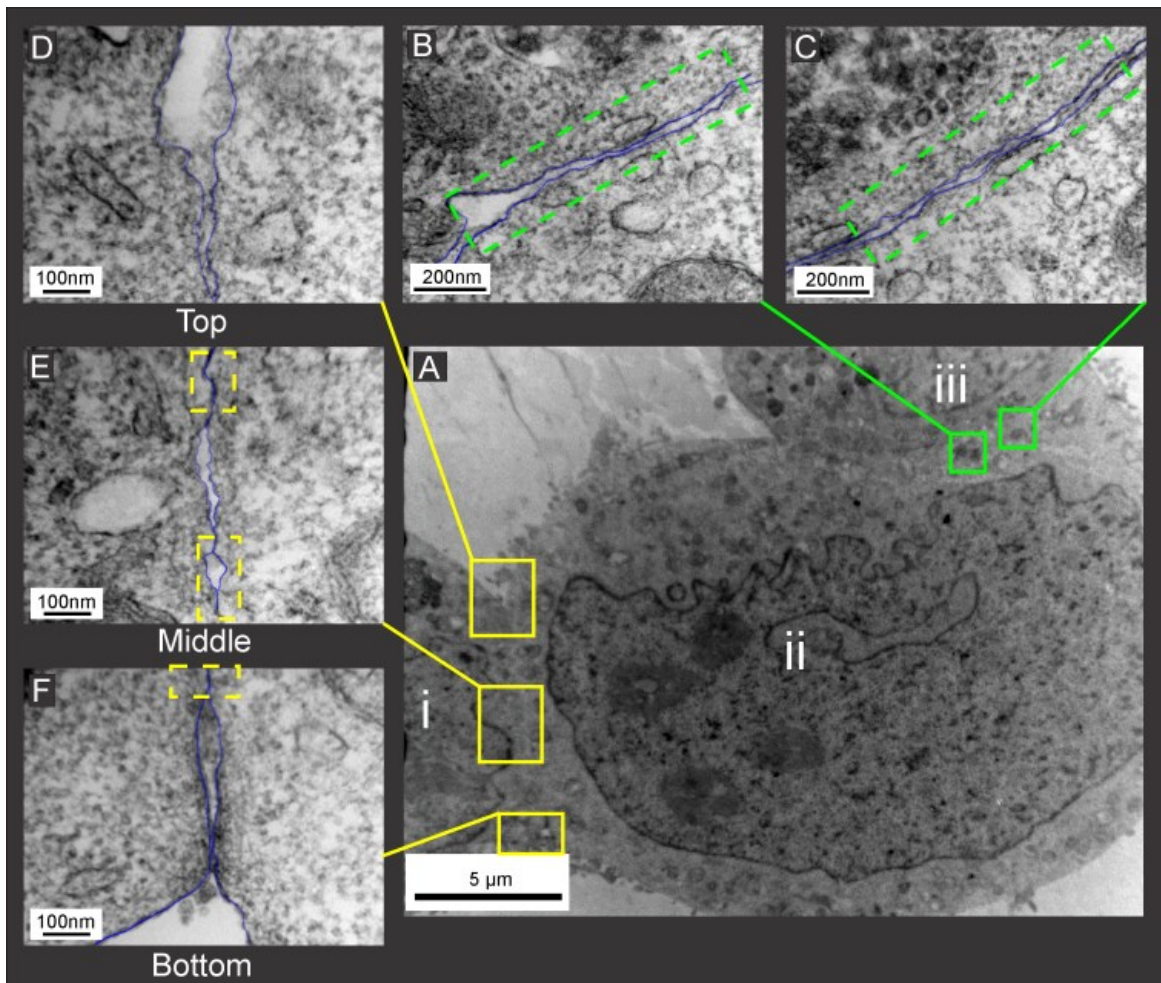


Figure 4.7: A. TEM z-slice of the three cells depicted in figure 3. Here, the middle cell (ii) is naturally attached to one cell (iii) and laser hemifused to the other cell (i). **B, C.** The region of naturally attached cells is depicted. The individual membranes are clearly identifiable, with a gap of 10-20 nm between the membranes. The green dashed line indicates the location of the naturally attached membranes. **D,E,F.** The region of femtosecond laser pulse induced hemifusion is shown, where the individual cell membranes cannot be distinguished. The yellow dashed line indicates the location of membrane hemifusion.

While it is demonstrated that hemifusion takes place during attachment of cell membranes using femtosecond laser pulses, it is also important to confirm that this process takes place throughout the entire penetration depth of the femtosecond laser pulses. In order to obtain strong adhesion

between the cells, it is ideal to maintain hemifusion across a large surface area of the membrane. Therefore, other TEM z-slices located along the entire penetration depth of the femtosecond laser pulses were examined. Figure 4.8 depicts an exemplary z-slice of the same group of cells. Similar to figure 4.7A, the naturally attached membranes and the laser-induced hemifused membranes are clearly identifiable in figure 4.8A. High magnification TEM images of the edge of the femtosecond laser pulse induced hemifusion region are provided in figures 4.8B-D. Again, at the area where the cells were in close proximity to each other, the phospholipid membranes hemifused to form a single membrane with one shared phospholipid bilayer. The hemifusion process takes place at the entire contact surface along 2 μ m depth, supporting the findings reported in section 4.4, that the attachment formed between the two cells is strong and is resistant to twisting and pulling [1].

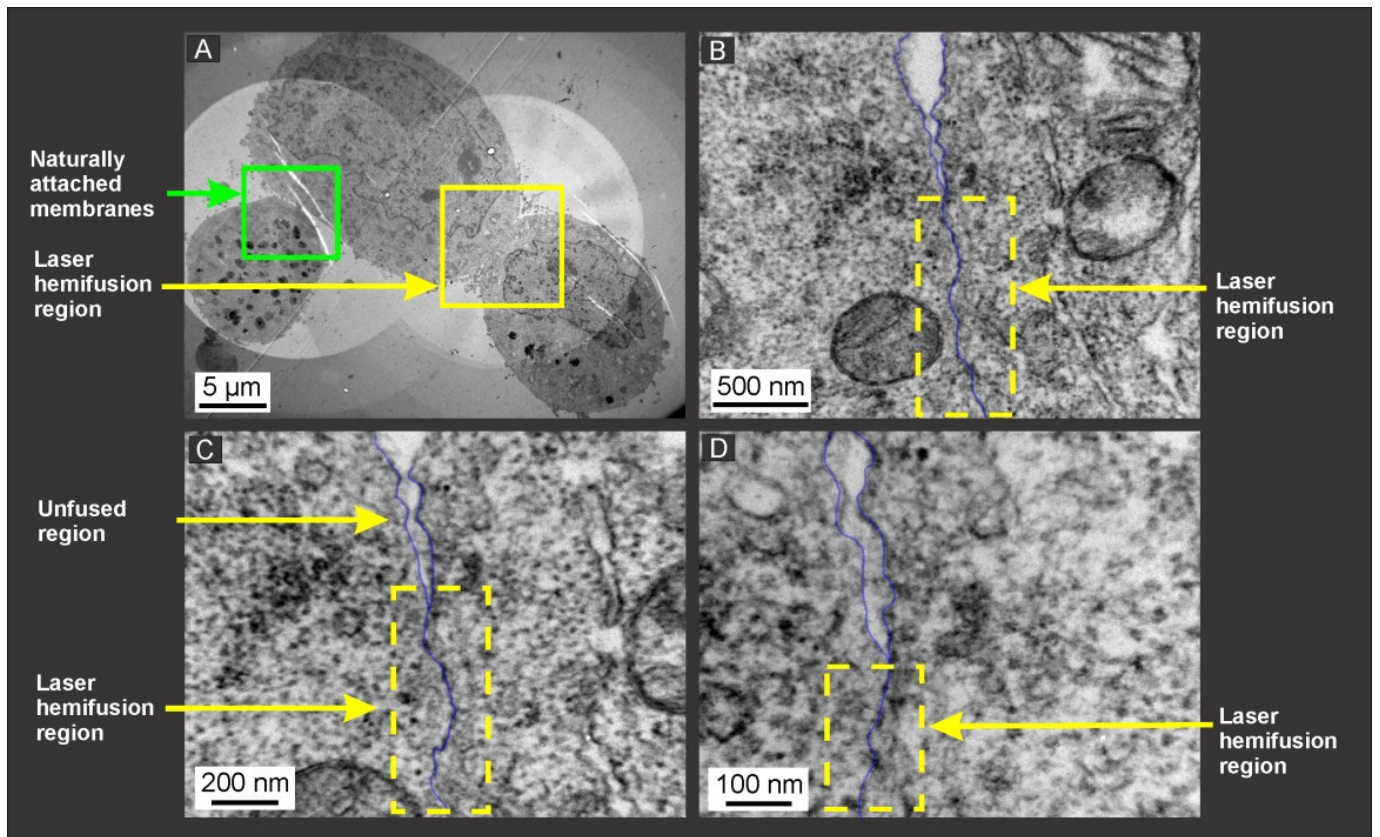


Figure 4.8: **A.** TEM z-slice of three retinoblastoma cells under low magnification. Here, the middle cell is naturally attached to one cell (left) and laser hemifused to the other cell (right). **B,C,D.** In order of increasing magnification from B-D, the laser-hemifused membranes are depicted. The two membranes merge to form a single phospholipid layer shared by both cells.

4.6.2 Characterization Discussion

The cellular membrane is made of a phospholipid bilayer, which surrounds the cytoplasm of living cells. It also serves as a scaffold that houses cellular structures such as channels, proteins, and saccharides. The cellular membrane acts as the “gateway” to the cell and is extremely important for the proper functionality and behavior of the cell. Biologists and engineers could greatly benefit from a device that could precisely modify the cellular membrane without affecting the viability of the cell, in order to study the effects of such modifications on the behavior and survival of the cell. It is well-known that imaging the molecular structure of the cell membrane is challenging; meanwhile, functional and structural changes of the cellular membrane are good indicators of precise alterations done to the molecular structure of the cell membrane. In section 4.6, an emphasis is given on verifying the hypothesis that femtosecond laser-induced cell-cell surgical attachment of cell membranes occurs through the process of hemifusion. This verification indicates that using femtosecond laser pulses, one could modify the structure of the cellular membrane without affecting the cell’s viability. The results provided show that cells adhere at the surface level of the cell membranes, where this attachment is molecular in its nature. It was previously reported [1,4-6] that at the laser intensity used to perform the femtosecond laser pulse induced membrane hemifusion, the viability of the cells is preserved.

In order to obtain TEM images of a hemifusion location it is critical to preserve the delicate cell structure during the harsh sample preparation procedure. A gridded dish was used in this experiment in order to locate the cells which the attachment procedure was performed on. The attachment is performed on one pair of cells in a dish that contains a few thousand cells. The key is to make the cells adhere strongly to the plate after the attachment is completed, and to perform the cell preparation without detaching the cells from the dish.

For femtosecond laser pulses, the exposure time is much shorter than the thermal diffusion time. Therefore, the thermal relaxation process is decoupled from the electronic excitation where energetic electrons are created locally before they can transfer their energy to the surrounding [60,73]. This physical phenomenon also explains that the process of attachment takes place due to reversible destabilization of the phospholipid molecules, and not due to thermal melting of the cell membranes.

4.6.3 Characterization Conclusion

In this section further evidence demonstrated that the mechanism behind cell-cell surgical attachment is femtosecond laser-induced hemifusion of the cellular membranes. Here, a visual insight is provided as to how does a laser-induced attached membrane appears after treatment. The images provided demonstrate that the structure of laser-induced attached membranes look substantially different than naturally attached membranes, and seem to agree with the hypothesized hemifused model. However, further evidence could shed more light on the laser-induced attachment process in the future. The laser pulse induced hemifusion takes place along the entire penetration depth of the laser pulses, thus resulting in strong physical cell attachment across a large surface area. Laser-induced avalanche ionization process leads to an ultrafast reversible destabilization of the phospholipid bilayers. During relaxation of the phospholipid molecules, the molecules seek equilibrium state and bind to the nearest free phospholipid molecule, thereby forming a joint membrane at the contact region. The procedure of laser-induced hemifusion is essentially a form of molecular surgery performed on the surface of a living cell. It is envisaged that other forms of femtosecond laser-induced molecular surgery could potentially serve as a tool for researchers to study and manipulate cellular membrane structures. This innovative procedure can further the knowledge on the key roles of the cellular membrane

and allow scientists to develop new cell-membrane targeting drugs and treatment for, currently, incurable diseases.

Chapter 5

Novel Method for Neuronal Nanosurgical Connection⁶

⁶ Portions of this chapter have been published in: Katchinskiy et al. Novel method for neuronal nanosurgical connection. Sci Rep 2016 February 05;6:20529.

5.1 Introduction

Neurons are cells within the nervous system that process and transfer information through electrical impulses and chemical signals [144,145]. This type of communication between neurons occurs in a specific interphase called a synapse [145]. The Central Nervous System (CNS) which includes the brain and the spinal cord, as well as the Peripheral Nervous System (PNS) operate in a similar pattern utilizing a neuronal synaptic network as a means of intercellular communication. It is imperative to have intact neuronal circuits in order to maintain normal organ and organism function. The typical neuronal structure, seen in figure 6.1, includes cell body (soma), dendrites, and an axon. Dendrites are structures arising from the cell body branching multiple times. An axon is a cellular extension arising from the cell body which can traverse a long distance in human beings and in other species. The axon may branch multiple times and connect to multiple cells prior to termination. There is an average of 300 trillion synapses in the adult brain [146].

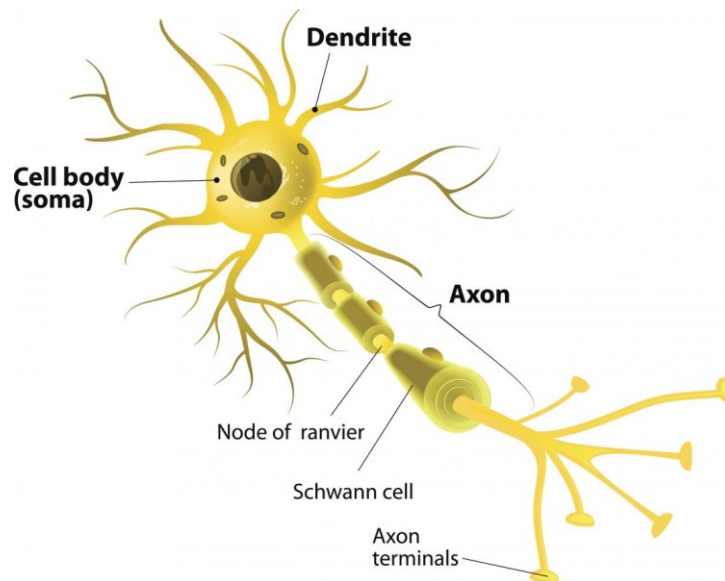


Figure 5.1: Illustration of neuron and its structures (soma, dendrite, and axon). Image is taken from <https://www.medicalnewstoday.com/articles/320289.php>

Neural communication is usually transferred through one neuron's axon to a dendrite or cell body of another neuron. However, there are other connection options based on different neuronal cell structures: for example, axon to axon, dendrite to dendrite, etc [147]. The cell membrane of the soma and the axon is electrically conducting through activation of voltage-gated ion channels [147]. These calcium, sodium, potassium, and chloride ion channels generate the electrical signals propagated in the axons.

Neurons are highly specialized cells that can no longer divide. Neurogenesis is very limited in adulthood; hence, nerve injury has a major impact on the ability to maintain normal function. There are a few recognized patterns to peripheral nerve damage post injury: Wallerian degeneration, segmental demyelination and axonal degeneration [148-153]. Wallerian degeneration develops after transection of the nerve and injury to the axon and its myelin sheath, where distal to the transection both the axon and the myelin will degenerate. A conduction block is observed one week after the injury. Regrowth is possible depending upon preservation of the basement membrane of the cells that are producing myelin (Schwann cells) and approximation of the nerve ends [148,149]. This type of damage may cause atrophy of the muscle innervated by the damaged neuron. Segmental demyelination is the result of damage restricted to the myelin sheath. As the axon is preserved, no end point muscle degeneration is expected or observed [149,150]. Axonal degeneration is caused by damage to the neural cell body resulting in distal death of the axon. Muscle atrophy will develop unless re-innervation occurs from adjacent nerves, however recovery may be only partial [151-153]. Experimental work on nerve injury repair has been carried out in the last decade and a few approaches have been investigated. These techniques included: bridging a gap by utilizing growth permissive matrix placed across the site of injury to allow axonal growth [154], creating new network via stem cell therapy [154],

providing neurotropic support in order to stimulate sprouting of spared axons or enable regeneration of injured axons [154,155]. Alternative techniques attempted to overcome myelin associated growth inhibitors [154,155], and scar-associated growth inhibitors [154,155]. Molecular protection of cells was used to avoid from the cascade of biochemical events that lead to cell death post injury [155]. These investigational treatments were encouraging but had partial success in animal models.

It is of paramount importance to develop a precise means of selectively connecting specific axons to neuron cell body. Such a leap in scientific method will open up doors to unparalleled research frontiers in neurology, cell biology, biochemistry, and electrophysiology. Connecting neurons, before or right after injury, enables the preservation of the viability of the neural network, thereby allowing complex pathophysiological processes, such as neurogenesis, Wallerian degeneration, segmental demyelination, and axonal degeneration to be further understood. Understanding the complex pathophysiological processes and the time frame available in order to prevent conductivity block and axonal death makes it necessary to develop techniques that enable the connection of nerve ends as soon as possible post injury, and maintain the viability of a healthy neural network. We describe a novel laser application to physically reattach severed neurons right after injury. This method may potentially allow further prevention of a conductivity block. Moreover, it may trigger studies questioning the hypothesis whether physical attachment and approximation of the nerve ends will stimulate recovery.

To date, a method to connect neuron ends does not exist. Assessment of axonal growth and regeneration is currently performed via either immunolabeling, where specific proteins that are involved in known regeneration pathways are labeled and monitored or via anterograde and retrograde tracing to visually trace neural connections from their termination/source to their

source/termination. These imaging methods are utilized to trace the neuronal projections from one location to various targets in the nervous system, and it allows researchers to study the natural process of axonal regeneration. However, the above mentioned techniques are limited to studying only the natural healing processes of neurons. Thus, control on selection and isolation of neurons, in order to study regeneration of specific neurons, is not available. Knowledge gained from such studies will allow researchers to develop new therapies for, currently, irreversible neuronal injuries and diseases.

A prime candidate method for connecting specific neurons that fulfills such key applications is femtosecond laser pulse technology, as removal or ionization of material is confined to less than a diffraction limited spot size, with no damage to surrounding material. Femtosecond laser pulses have also been used as a tool to study neuron regeneration by severing neurons and axons [156]. This method allows creating of precise injury that enables the studies on axonal injury and regeneration at the single cell level [156]. In Chapter 4, a technology that can be used to attach cells was discussed [1]. However, physical connection of single neurons has not been performed thus far.

In this chapter, a method for neuron connection using femtosecond laser pulses is presented. By physically connecting single axons and neurons right after injury, it will allow researchers to develop new methods of studying the effects of neuron connection on neuronal regeneration, progression of Wallerian degeneration, and the existence of cellular communication, to further our understandings of these phenomena. This effective neuronal connection method should allow the user to select single cells for isolation, connection, and cutting. The technique is shown to be applicable to multiple cell types and their media.

5.2 Experimental Methodology

5.2.1 Cell Cultures

P19 mouse teratocarcinoma cells [157] were cultured in Dulbecco's Modified Eagle's Medium (DMEM) supplemented with 7.5% bovine serum and 2.5% fetal calf serum. For neuronal differentiation, P19 cells were cultured in petri dishes (to allow formation of embryoid bodies) at a density of 10^5 cells/ml in the presence of $1 \mu\text{M}$ all-trans-retinoic acid (RA) (Sigma R2625) (Day 0) [158]. On Day 2, the medium was replaced with fresh DMEM supplemented with serum and $1 \mu\text{M}$ RA. On Day 4, the embryoid bodies were trypsinized and broken down into single cells. These single cells were plated on coverslips and cultured in DMEM plus 10% fetal calf serum. On Day 6, the cells were treated with $5 \mu\text{g/ml}$ Ara-C (Sigma C1768) in order to remove any remaining proliferating cells. The cells completed neuronal differentiation by Day 8, at which stage long neurite projections could be observed. Neuro2A (mouse neuroblastoma cells) were cultured in DMEM supplemented with 10% fetal calf serum, penicillin (100 U/ml) and streptomycin ($100 \mu\text{g/ml}$). At confluence, cells were trypsinized and plated on coverslips.

5.2.2 Experimental Procedure

On separate experiments, P19 and Neuro2A cells were placed inside a glass dish with DMEM solution and mounted on a motorized x-y-z nano-translation stage for precise movement control of the cell culture. Trypsin solution was added to each dish in order to release the neurons from the bottom of the plate. After 10 minutes, the dish was shaken by hand in order to suspend the neurons in the solution. Neurons with identifiable axons and that are not attached to large groups have been identified and selected for connection. The selected neurons were brought into contact using an optical tweezer, such that an axon of one neuron touches the soma of the other neuron. The optical tweezer was made collinear with the femtosecond laser pulse train. Once the desired

contact region between the axon and cell soma was identified, it was precisely targeted by the femtosecond laser pulse train for a duration of 15ms. The mechanical integrity of the connected neurons was then assessed using an optical tweezer. This was performed by trapping one of the neurons to the optical tweezer's focal spot, and moving the trapped cell(s) in various paths. In order to verify that proper attachment was obtained, three criteria were assessed: (1) no detachment due to twisting, and drag forces (2) movement of all cells due to trapping of any cell in the group, and (3) movement of all cells as a single unit. We confirmed the physical cellular attachment by following the translation of the trapped cell as an integral unit together with the other cells without detaching from each other. In order to verify that the connected neurons did not move only due to their proximity to the optical trap, groups of four neurons were attached. Using this technique we were able to ensure that the neurons are located far enough from the optical trapping spot, where the attraction forces to the laser tweezers are too weak to pull an individual cell.

5.3 Results

A novel neuron connection method was developed using ultrashort femtosecond laser pulses (illustrated in Figure 5.2a). Precise tuning of the laser parameters allowed us to induce a process called hemifusion at the contact point of two phospholipid membranes (illustration of the contact point is seen in Figure 5.2b). To achieve neuron connection, the laser intensity and aiming accuracy required are $1.7(\pm 0.08) \times 10^{12}$ W/cm², and $\pm 0.5 \mu\text{m}$, respectively, within the membranes hemifusion location. Exposure to near infrared femtosecond laser pulses induces molecular rearrangement of the phospholipid bilayers via multiphoton and avalanche ionization processes. The high electron and ion density at the laser beam focal point leads to an ultrafast reversible destabilization of the phospholipid molecules. Since the membrane's exterior surface is

permeable to both photo-induced ions and electrons, these can cross over to the central nonpolar region of the phospholipid bilayer and break the bonds of the fatty acid tails, as illustrated in Figure 5.2c. At the end of this destabilization process, the ionized phospholipid molecules seek equilibrium state, and form new bonds with nearby ions, as seen in Figure 5.2d. Only the phospholipid molecules that are located at the cell membrane contact point cross-link with phospholipid molecules of the adjacent cell membrane. The cross-linking process leads to the formation of a single, shared, phospholipid bilayer (i.e. hemifused membrane), which is the underlying mechanism that takes place in this neuron connection method and provides a strong attachment.

To demonstrate the neuron connection method, it is shown that this technique can be used on any number and types of neurons by its implementation on two neuron types: P19, and Neuro2A. Neurons were grown in culture, and suspended in DMEM solution right before connection (see section 5.2 for methods). Selected neurons for connection were identified, isolated and brought into contact using an optical tweezer such that the protruding axon of one neuron touched another neuron's soma. In order to ensure that the neurons do not naturally stick to each other, the cells were left touching for a period of time, and then pulled apart by the optical tweezer. The neurons did not show any signs of natural connectivity. The neurons were brought into contact once more, and then femtosecond laser pulses were delivered to the axon and cell soma connection point in order to induce an attachment. To validate that a connection was achieved, one of the neurons was moved inside the suspension dish using optical tweezer, and it was found that all neurons followed a corresponding path, twisted, and rotated as a single entity, without showing any sign of detachment. Figure 5.3a depicts the attachment of two Neuro2A cells, where the axon of cell (i) is attached to the soma of (ii).

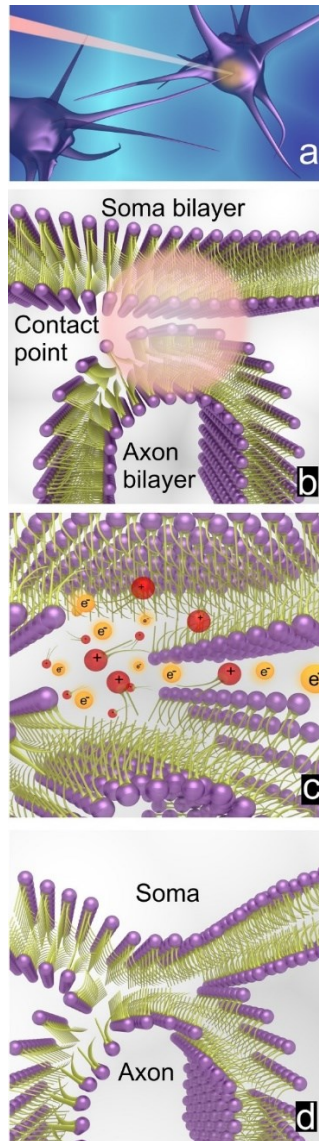


Figure 5.2: **A.** An illustration of how a femtosecond laser pulse is delivered to the target point between an axon and a neuronal soma. **B.** An illustration of the phospholipid bilayers of the neuron soma and axon. Note that the attachment region, where the phospholipid layers are attaching, is designated with a circular spot. This does not represent the laser focal spot. **C.** The laser pulse high intensity causes a reversible destabilization of both phospholipid layers. A depiction of the femtosecond laser pulse induced axon-soma attachment. Here, the generated free ions (shown in red) and free electrons (shown in orange) cross the center nonpolar region and break bonds between the fatty acid hydrophobic tails. **D.** The relaxation process results in the formation of new stable bonds and formation

Connection of single neuron to multiple neurons is a fundamental requirement for assembling a chain of neurons, and to maintain neuronal connectivity and continuity. As shown in Figure 5.3b, two axons from Neuro2A (i) were attached to Neuro2A (ii) and (iii). The cells are shown, in Figure 5.3c, after being moved and oriented approximately 30° relative to their original orientation.

Figures 5.3d-f depict a femtosecond laser induced connection of P19 axon to P19 soma (preparation can be found in section 5.3). Here, connection of groups of targeted neurons is demonstrated. Two groups of four P19 cells were identified, as shown in figure 5.3d. The axon of neuron (i) came in contact and was connected with (ii), using femtosecond laser pulses. In figure 5.3e the cells are shown right after attachment, and in figure 5.3f the cells are shown after being pulled and rotated using the optical tweezer.

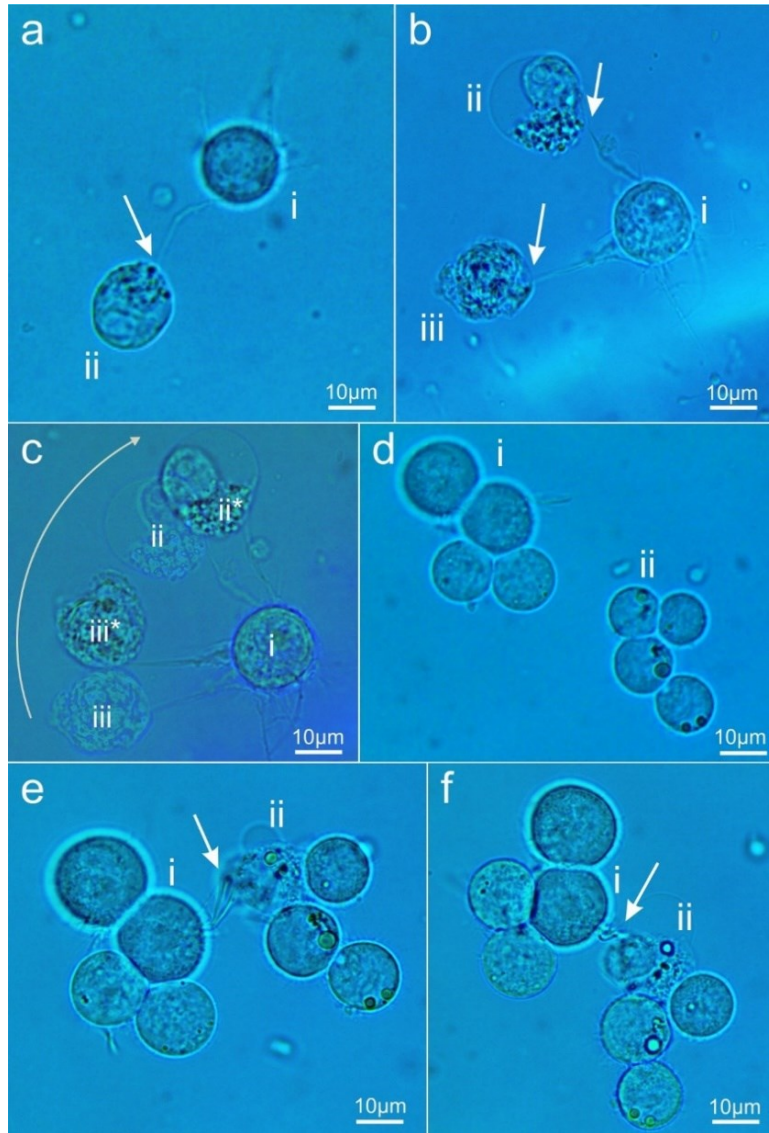


Figure 5.3: The arrows point to the location of neuron connection using femtosecond laser pulses. **A.** A single Neuro2A's (i) axon is connected to the soma of Neuro2A (ii). **B.** Two axons of Neuron2A (i) are connected using to the soma of Neuro2A cells (ii) and (iii). **C.** Overlap image of the original Neuro2A cells (i), (ii), and (iii) compared to Neuro2A cells (i), (ii*), and (iii*) after being rotated and moved by an optical tweezers to examine the integrity of the axons' connectivity. **D.** Two groups of four P19 neurons are identified. **E.** The axon of P19 (i) is brought into contact with the soma of P19 (ii), and are connected as shown by the arrow tip. Note that there is another unconnected axon nearby which was left detached **F.** The two groups of P19 cells are rotated and moved by optical tweezers to examine the integrity of the axons' connectivity.

5.4 Conclusion

Several groups of neurons were attached in order to demonstrate the proposed neuron connection method. One to two 15ms pulse trains (i.e. 1.2×10^6 pulses) were necessary to achieve attachment, with 90% success rate. Throughout the observations and rigorous manipulations, the cells remained viable and firmly attached without showing signs of deterioration in attachment strength, validating long term viability and attachment prospects. Moreover, previously reported cell-cell attachment method [1], and long-term viability experiments [159,160] also confirm that the laser parameters used for this method fall within a safe range for preserving cell viability and attachment. It is envisaged that femtosecond laser-induced neuronal nanosurgical connection method can potentially open up new frontiers in the studies of the effects of connecting neurons, right before or after injury. The preservation of the viability of the neural network will allow researchers to study new complex pathophysiological processes, such as neurogenesis, Wallerian degeneration, segmental demyelination, and axonal degeneration. This will allow further development of new therapies for neuronal injuries and disease.

Chapter 6

Conclusion and Future Prospects

6.1 Conclusion

In this thesis, the application of femtosecond laser pulses in the medical and biomedical research area was explored. Three main applications were researched and accomplished are: 1. Treatment of Retinoblastoma using cancer targeting gold nanorods. 2. Selective attachment of cells. 3. Selective attachment of neurons.

The study in chapter 3 demonstrated that it would be possible to use Au-NRs and femtosecond pulse lasers to target retinoblastoma cells. Since the eye has minimal absorption or scattering at a wavelength $\lambda=800\text{nm}$, it is a suitable tissue for such treatment methodology. Retinoblastoma targeting Au-NRs can be injected into the eye, and the femtosecond laser pulses can be delivered externally onto the innermost layer of the eye, the retina. This will result in selective destruction of cancer cells alone while sparing healthy cells. Furthermore, the clinical translation of these proof-of-concept results could be developed into a treatment that would not only save children's lives, but would also allow for the preservation of their vision. Furthermore, this thesis explores specific targeting and toxicity of the Au-NRs, treatment with femtosecond laser pulses and the effect of laser alone on the cells. An analysis on the optimal laser parameters required to elicit effective treatment was studied, in addition to analysis of the mechanism that causes cell death.

The study in chapter 4 demonstrated that attachment of single cells using femtosecond laser pulses is possible, while preserving the cells' viability. It was shown that the cellular cytoplasm remained in isolation from the surrounding medium during and after the attachment procedure. A strong physical attachment between the cells was obtained. Femtosecond laser-induced cell-cell surgical attachment can potentially provide an efficient and safe technique for the creation of engineered tissue and cell cultures. A possible long term vision, is to apply this technique in surgical interventions that require artificially made tissue. Additionally, it was demonstrated that

the mechanism behind cell-cell surgical attachment is femtosecond laser-induced hemifusion of the cellular membranes. Here, a visual insight into the structure of the cell membranes was obtained. TEM images demonstrated that the structure of laser-induced attached membranes look substantially different than naturally attached membranes, and seem to agree with the hypothesized hemifused model. It also shows that the laser pulse induced hemifusion takes place along the entire penetration depth of the laser pulses, thus resulting in strong physical cell attachment across a large surface area. The mechanism of laser-induced hemifusion is essentially a form of molecular surgery performed on the surface of a living cell. It is envisaged that other forms of femtosecond laser-induced molecular surgery could potentially serve as a tool for researchers to study and manipulate cellular membrane structures. This innovative technology can further the knowledge on the key roles of the cellular membrane and allow scientists to develop new cell-membrane targeting drugs and treatment for, currently, incurable diseases.

Finally, the study in chapter 5 demonstrated attachment of several groups of neurons in order to demonstrate the proposed neuron connection method. Throughout the observations and rigorous manipulations, the cells remained viable and firmly attached without showing signs of deterioration in attachment strength, validating long term viability and attachment prospects. It is envisaged that femtosecond laser-induced neuronal nanosurgical connection method can potentially provide a scientific leap that will open up new frontiers in the studies of the effects of connecting neurons, right before or after injury. The preservation of the viability of the neural network will allow researchers to study new complex pathophysiological processes, such as neurogenesis, Wallerian degeneration, segmental demyelination, and axonal degeneration. This will allow further development of new therapies for neuronal injuries and disease.

6.2 Future Prospects

Applied femtosecond laser pulses and gold nanorods towards cancer treatment is proven to be a promising technology. To conclude the thesis, it is valuable to identify future studies that would be the natural progression towards development of a ‘real-life’ cancer therapy, used by clinicians. The most natural progression of the work presented in this thesis is to continue the work with either an animal model or a tissue extracted from a human. Thus, to ensure the success of this next step in the research, a unique collaboration was established with the UofA department of Otolaryngology - Head & Neck Surgery, Dr. Erin Wright and Dr. Ilan Blau, and the Edmonton Cross Cancer Institute; who have dedicated time and in-kind resources towards this common goal. This collaboration was established in order to study the potential of femtosecond laser pulses and cancer targeting gold nanorods towards cancer therapy of papillary thyroid carcinoma. With this technique, papillary thyroid carcinoma treatment will become simple and painless; this will preserve the patient's quality of life during the application of therapy. This approach minimizes damage to healthy tissue and thus reducing pain and other side effects. The collaborative work aims to establish a stepping-stone for a new cancer treatment modality, which will potentially revolutionize the treatment approach of thyroid cancer.

Thyroid neoplasms represent almost 95% of all endocrine tumors and account for approximately 2.5% of all malignancies [161,162]. Thyroid cancer affects over half a million people in the U.S. and the incidence of thyroid cancer has increased worldwide at a rate higher than any other cancer. The increase in incidence is almost completely attributable to papillary thyroid cancer occurrences, more specifically, micro adenoma (tumor mass of less than 1 cm in diameter) [161,162]. Thyroid cancer is projected to be the fourth most common cancer by 2030 [161,162].

Most thyroid carcinomas are well-differentiated tumors of follicular cell origin; these lesions are histologically defined as papillary carcinoma (79%), follicular carcinoma (13%), and Hürthle cell carcinoma (3%). Medullary thyroid carcinoma (MTC), which arises from Para-follicular C cells, accounts for about 4% of thyroid carcinomas [161,162].

The most common presentation of a thyroid cancer is the development of a thyroid mass or nodule [161,162]. Between 20-70% of adults develop thyroid nodules in their lifetime, with older adults having a higher prevalence than younger. Based on patients' risk factors, and sonographic findings a decision whether to further investigate a thyroid nodule is taken. Histology results can only be obtained either by resecting one lobe or by resecting the whole gland. The decision regarding the surgical strategy for a suspicious thyroid nodule is mainly dependent on cytology, which is achieved by Fine Needle Aspiration (FNA) [161,162].

The Bethesda cytology scale for thyroid nodules has been developed as a tool for the clinician to assist with the question whether to operate. A 5-6 Bethesda grade thyroid nodule will eventually be a papillary carcinoma with a probability above of 70-97%, respectively [161,162].

Complications and side effects of thyroid surgery include bleeding, infections, hoarseness due to recurrent laryngeal nerve injury and as a consequence vocal cord palsy, hypoparathyroidism due to parathyroid glands injury, and possible dependency on hormone replacement therapy. A significant scar will appear in the central neck [161,162]. Thus, a novel technique for treating of thyroid cancer, which requires no surgery, will eliminate most possible complications resulting from surgical removal of thyroid glands.

Objectives:

To evaluate the reaction of thyroid cancer cells containing gold nanorods to irradiation with femtosecond laser pulses:

1. Quantification of destruction of cancerous thyroid tissue
2. Evaluation of the destruction mechanism
3. Evaluation of the selectivity of this treatment method, where cancer cells are treated, while healthy cells are spared.

Hypothesis:

The thyroid cancer cells containing gold nanoparticles will be destroyed when irradiated by femtosecond laser pulses, while healthy thyroid cells will remain intact.

The destruction mechanism of thyroid cancer cells will be through the process of necrosis.

Justification:

We are developing a novel technique which may prevent the need for surgical removal of the thyroid gland. This will prevent unnecessary surgery for false positive FNA diagnosed patients. In addition, it may prevent, currently necessary surgical removal of positively diagnosed patients.

Patient's recruitment:

Patients with FNA positive papillary thyroid carcinoma, Bethesda 5-6, will be recruited at the University of Alberta Hospital and the Royal Alexandra Hospital.

Inclusion criteria

1. Adults, referred to thyroid surgery due to suspected papillary thyroid carcinoma.
2. FNA positive to papillary thyroid carcinoma, Bethesda 5-6.
3. Ultrasound scan is performed and confirms that the thyroid nodule is located at the periphery of the gland.

Exclusion

1. No other known head and neck malignancies currently or in the past.
2. No irradiation exposure in the past.

Specimen Preparation, Cell Culture and Preparation

The resected thyroid gland or lobe will be inspected by the surgeon or his assistant. If the cancerous node is easily palpated, and located in the periphery of the gland, then, a small sample (1 mm³) will be taken of its free edge (located on the part of the tumor that do not have contact with surrounding thyroid tissue). Another sample (similar in size), will be taken from the normal appearing thyroid tissue of the already resected specimen. The tissue will be brought to the Cross Cancer Institute, where it will be processed. The tissue will be incubated in culture media:

Dulbecco's modified Eagle medium supplemented with 100 U/ml penicillin and 100 µg/ml streptomycin, and 10% fetal bovine serum. The specimens will be transferred with no identifying details.

Results

So far, the group has obtained ethics approvals from the Alberta ethics committee to extract samples from patients suffering from papillary thyroid carcinoma, within the inclusion criteria. Additionally, samples from 4 patients were successfully obtained, and experiments using anti-EGFR decorated gold nanorods and femtosecond laser pulses were performed on these tissue samples. The experiments included 4 types of treatments (i) Papillary thyroid carcinoma cells treated with Au-NRs and irradiated with fs laser pulses, (ii) Papillary thyroid carcinoma cells irradiated with fs laser pulses only, (iii) untreated Papillary thyroid carcinoma cells (control), and (iv) Papillary thyroid carcinoma cells treated with Au-NRs without fs laser irradiation. To date, some exciting results have been obtained from the experiments performed. We have recruited a pathologist to assist with reviewing the samples. The last two samples obtained were reviewed blindly to all identifying information. Many of the slides showed essentially normal thyroid parenchyma with numerous thyroid follicles. A few slides showed viable papillary carcinoma. However, other slides showed varying degrees of fibrosis and calcifications (treated slides – showing no papillary carcinoma cells are left). A few slides showed atypical cells that may represent residual tumor but may also represent reactive changes. All observations matched the treatment protocol carried out on these samples. The current analysis technique used on the samples is H&E staining histology. The main hypothesis is that the cell death takes place through the process of necrosis. This work is still in its infancy and is currently undergoing further investigation. However, the current results are promising.

References

- [1] N. Katchinskiy *et al*, "Femtosecond laser-induced cell-cell surgical attachment," *Lasers Surg. Med.*, vol. 46, (4), pp. 335-341, April 01, 2014.
- [2] N. Katchinskiy, R. Godbout and A. Y. Elezzabi, "Characterization of femtosecond-laser pulse induced cell membrane nanosurgical attachment," *Biomed. Opt. Express*, vol. 7, (7), pp. 2749-2758, June 22, 2016.
- [3] N. Katchinskiy *et al*, "Novel Method for Neuronal Nanosurgical Connection," *Sci. Rep.*, vol. 6, pp. 20529, February 05, 2016.
- [4] V. Kohli, A. Y. Elezzabi and J. P. Acker, "Cell nanosurgery using ultrashort (femtosecond) laser pulses: applications to membrane surgery and cell isolation," *Lasers Surg. Med.*, vol. 37, (3), pp. 227-230, September 01, 2005.
- [5] V. Kohli, J. P. Acker and A. Y. Elezzabi, "Reversible permeabilization using high-intensity femtosecond laser pulses: applications to biopreservation," *Biotechnol. Bioeng.*, vol. 92, (7), pp. 889-899, December 30, 2005.
- [6] V. Kohli and A. Y. Elezzabi, "Prospects and developments in cell and embryo laser nanosurgery," *Wiley Interdiscip. Rev. Nanomed Nanobiotechnol*, vol. 1, (1), pp. 11-25, February 01, 2009.
- [7] A. Vogel *et al*, "Mechanisms of femtosecond laser nanosurgery of cells and tissues," *Applied Physics B*, vol. 81, (8), pp. 1015-1047, 2005.
- [8] H. Xie, F. M. Kong and K. Li, "The Electric Field Enhancement and Resonance in Optical Antenna Composed of AU Nanoparticles," *Journal of Electromagnetic Waves and Applications*, vol. 23, (4), pp. 534-547, 2009.
- [9] L. Novotny, "Effective Wavelength Scaling for Optical Antennas," *Phys. Rev. Lett.*, vol. 98, (26), pp. 266802, 2007.
- [10] H. A. Atwater and A. Polman, "Plasmonics for improved photovoltaic devices," *Nature Materials*, vol. 9, (3), pp. 205, 2010.
- [11] D. S. Sebba, D. A. Watson and J. P. Nolan, "High Throughput Single Nanoparticle Spectroscopy," *ACS Nano*, vol. 3, (6), pp. 1477-1484, 2009.
- [12] M. T. Wenzel *et al*, "Gold nanoparticle tips for optical field confinement in infrared scattering near-field optical microscopy," *Optics Express*, vol. 16, (16), pp. 12302, 2008.

- [13] J. Niu, T. Zhu and Z. Liu, "One-step seed-mediated growth of 30–150 nm quasispherical gold nanoparticles with 2-mercaptosuccinic acid as a new reducing agent," *Nanotechnology*, vol. 18, (32), pp. 325607, 2007.
- [14] X. Huang and M. A. El-Sayed, "Gold nanoparticles: Optical properties and implementations in cancer diagnosis and photothermal therapy," *Journal of Advanced Research*, vol. 1, (1), pp. 13-28, 2010.
- [15] M. A. Mackey *et al*, "The most effective gold nanorod size for plasmonic photothermal therapy: theory and in vitro experiments," *J Phys Chem B*, vol. 118, (5), pp. 1319-1326, February 06, 2014.
- [16] S. Link, M. B. Mohamed and M. El-Sayed, "Simulation of the Optical Absorption Spectra of Gold Nanorods as a Function of Their Aspect Ratio and the Effect of the Medium Dielectric Constant," *J Phys Chem B*, vol. 103, (16), pp. 3073-3077, 1999.
- [17] G. Mie, "Contributions to the optics of diffuse media, especially colloid metal solutions," *Ann Phys*, vol. 25, pp. 377-445, 1908.
- [18] R. Gans, "Form of ultramicroscopic particles of silver," *Ann. Phys.*, vol. 47, (10), pp. 270-284, 1915.
- [19] P. K. Jain *et al*, "Calculated absorption and scattering properties of gold nanoparticles of different size, shape, and composition: applications in biological imaging and biomedicine," *J Phys Chem B*, vol. 110, (14), pp. 7238-7248, 2006.
- [20] S. Mohammadi Bilankohi, "Optical Scattering and Absorption Characteristics of Silver and Silica/Silver Core/shell Nanoparticles," *Orient J Chem*, vol. 31, (4), 2015.
- [21] S. Mohammadi Bilankohi, "The Simulation of the Optical Characteristics of Platinum and Platinum/Silica Nanoparticles," *Orient J Chem*, vol. 31, (1), 2015.
- [22] J. Aizpurua *et al*, "Optical properties of coupled metallic nanorods for field-enhanced spectroscopy," *Phys. Rev. B*, vol. 71, (23), pp. 235420, 2005.
- [23] G. W. Bryant, García de Abajo, F Javier and J. Aizpurua, "Mapping the Plasmon Resonances of Metallic Nanoantennas," *Nano Lett.*, vol. 8, (2), pp. 631-636, 2008.
- [24] K. Tanabe, "Field Enhancement around Metal Nanoparticles and Nanoshells: A Systematic Investigation," *J. Phys. Chem. C*, vol. 112, (40), pp. 15721-15728, 2008.
- [25] M. A. El-Sayed, "Shape and size dependence of radiative, non-radiative and photothermal properties of gold nanocrystals," *Int Rev Phys Chem*, vol. 19, (3), pp. 409-53, 2000.
- [26] M. A. El-Sayed, "Some interesting properties of metals confined in time and nanometer space of different shapes," *Acc. Chem. Res.*, vol. 34, (4), pp. 257-264, April 01, 2001.

- [27] S. Link and M. El-Sayed, "Spectral Properties and Relaxation Dynamics of Surface Plasmon Electronic Oscillations in Gold and Silver Nanodots and Nanorods," *J Phys Chem B*, vol. 103, (40), pp. 8410-8426, 1999.
- [28] S. Link *et al*, "Laser Photothermal Melting and Fragmentation of Gold Nanorods: Energy and Laser Pulse-Width Dependence," *J Phys Chem A*, vol. 103, (9), pp. 1165-1170, 1999.
- [29] S. Link *et al*, "Medium effect on the electron cooling dynamics in gold nanorods and truncated tetrahedra," *Adv Mater*, vol. 15, (5), pp. 393-6, 2003.
- [30] O. Ekici *et al*, "Thermal Analysis of Gold Nanorods Heated with Femtosecond Laser Pulses," *J. Phys. D. Appl. Phys.*, vol. 41, (18), pp. 185501, 2008.
- [31] S. Link *et al*, "Laser-Induced Shape Changes of Colloidal Gold Nanorods Using Femtosecond and Nanosecond Laser Pulses," *J. Phys. Chem. B*, vol. 104, (26), pp. 6152-6163, 2000.
- [32] Y. Li *et al*, "Femtosecond laser pulse driven melting in gold nanorod aqueous colloidal suspension: identification of a transition from stretched to exponential kinetics," *Scientific Reports*, vol. 5, pp. 8146, 2015.
- [33] A. Plech *et al*, "Laser-induced heating and melting of gold nanoparticles studied by time-resolved x-ray scattering," *Phys. Rev. B*, vol. 70, (19), pp. 195423, 2004.
- [34] N. S. Abadeer and C. J. Murphy, "Recent Progress in Cancer Thermal Therapy Using Gold Nanoparticles," *J. Phys. Chem. C*, vol. 120, (9), pp. 4691-4716, 2016.
- [35] E. Boulais *et al*, "Plasmonics for pulsed-laser cell nanosurgery: Fundamentals and applications," *Journal of Photochemistry and Photobiology C: Photochemistry Reviews*, vol. 17, pp. 26-49, 2013.
- [36] I. Akhatov *et al*, "Collapse and rebound of a laser-induced cavitation bubble," *Physics of Fluids*, vol. 13, (10), pp. 2805-2819, 2001.
- [37] D. Lapotko, "Plasmonic nanobubbles as tunable cellular probes for cancer theranostics," *Cancers (Basel)*, vol. 3, (1), pp. 802-840, 2011. . DOI: 10.3390/cancers3010802.
- [38] a. A. Prosperetti, "Bubble Dynamics and Cavitation," *Annual Review of Fluid Mechanics*, vol. 9, (1), pp. 145-185, 1977.
- [39] V. K. Pustovalov, A. S. Smetannikov and V. P. Zharov, "Photothermal and accompanied phenomena of selective nanophotothermolysis with gold nanoparticles and laser pulses," *Laser Phys. Lett.*, vol. 5, (11), pp. 775, 2008.
- [40] A. Ulman, "Formation and Structure of Self-Assembled Monolayers," *Chem. Rev.*, vol. 96, (4), pp. 1533-1554, 1996.

- [41] J. C. Love *et al*, "Self-assembled monolayers of thiolates on metals as a form of nanotechnology," *Chem. Rev.*, vol. 105, (4), pp. 1103-1169, April 01, 2005.
- [42] L. H. Dubois and R. G. Nuzzo, "Synthesis, structure, and properties of model organic surfaces," *Annu. Rev. Phys. Chem.*, vol. 43, pp. 437-463, 1992.
- [43] L. M. Demers *et al*, "Direct patterning of modified oligonucleotides on metals and insulators by dip-pen nanolithography," *Science*, vol. 296, (5574), pp. 1836-1838, June 07, 2002.
- [44] D. P. O'Neal *et al*, "Photo-thermal tumor ablation in mice using near infrared-absorbing nanoparticles," *Cancer Lett.*, vol. 209, (2), pp. 171-176, June 25, 2004.
- [45] T. Niidome *et al*, "PEG-modified gold nanorods with a stealth character for in vivo applications," *J. Control. Release*, vol. 114, (3), pp. 343-347, September 12, 2006.
- [46] V K Pustovalov and, V A Babenko, "Optical properties of gold nanoparticles at laser radiation wavelengths for laser applications in nanotechnology and medicine," *Laser Physics Letters*, vol. 1, (10), pp. 516, 2004.
- [47] E. B. Dickerson *et al*, "Gold nanorod assisted near-infrared plasmonic photothermal therapy (PPTT) of squamous cell carcinoma in mice," *Cancer Lett.*, vol. 269, (1), pp. 57-66, September 28, 2008.
- [48] X. Huang *et al*, "Cancer cell imaging and photothermal therapy in the near-infrared region by using gold nanorods," *J. Am. Chem. Soc.*, vol. 128, (6), pp. 2115-2120, February 15, 2006.
- [49] C. M. Pitsillides *et al*, "Selective cell targeting with light-absorbing microparticles and nanoparticles," *Biophys. J.*, vol. 84, (6), pp. 4023-4032, June 01, 2003.
- [50] E. Y. Hleb *et al*, "LANTCET: elimination of solid tumor cells with photothermal bubbles generated around clusters of gold nanoparticles," *Nanomedicine (Lond)*, vol. 3, (5), pp. 647-667, October 01, 2008.
- [51] L. Minai *et al*, "Optical nanomanipulations of malignant cells: controlled cell damage and fusion," *Small*, vol. 8, (11), pp. 1732-1739, June 11, 2012.
- [52] J. Noack and A. Vogel, "Laser-induced plasma formation in water at nanosecond to femtosecond time scales: calculation of thresholds, absorption coefficients, and energy density," *IEEE Journal of Quantum Electronics*, vol. 35, (8), pp. 1156-1167, 1999. . DOI: 10.1109/3.777215.
- [53] M. Niemz, *Laser-Tissue Interactions - Fundamentals and Applications*. (3rd ed.) 2007.
- [54] J. Boulnois, "Photophysical processes in recent medical laser developments: A review," *Laser Med Sci*, vol. 1, (1), pp. 47-66, 1986.

- [55] H. Susi, J. S. Ard and R. J. Carroll, "The infrared spectrum and water binding of collagen as a function of relative humidity," *Biopolymers*, vol. 10, (9), pp. 1597-1604, 1971.
- [56] van Veen, R L P *et al*, "Determination of visible near-IR absorption coefficients of mammalian fat using time- and spatially resolved diffuse reflectance and transmission spectroscopy," *J Biomed Opt*, vol. 10, (5), pp. 054004, 2005.
- [57] S. L. Jacques, "Optical properties of biological tissues: a review," *Physics in Medicine and Biology*, vol. 58, (11), pp. R37, 2013.
- [58] L. V. Keldysh, "Ionization in the field of a strong electromagnetic wave," *Soviet Physics JETP*, vol. 20, (5), pp. 1307-14, 1965.
- [59] J. W. Boyle *et al*, "Production of hydrated electrons by flash photolysis of liquid water with light in the first continuum," *J. Phys. Chem.*, vol. 73, (9), pp. 2886-2890, 1969.
- [60] C. B. Schaffer, A. Brodeur and E. Mazur, "Laser-induced breakdown and damage in bulk transparent materials induced by tightly focused femtosecond laser pulses," *Meas. Sci. Technol.*, vol. 12, (11), pp. 1784, 2001.
- [61] A. Heisterkamp *et al*, "Pulse energy dependence of subcellular dissection by femtosecond laser pulses," *Opt Express*, vol. 13, (10), pp. 3690-3696, 2005.
- [62] S. H. Chung *et al*, "The role of the AFD neuron in *C. elegans* thermotaxis analyzed using femtosecond laser ablation," *BMC Neurosci*, vol. 7, pp. 30, 2006.
- [63] U. K. Tirlapur and K. König, "Femtosecond near-infrared laser pulses as a versatile non-invasive tool for intra-tissue nanoprocessing in plants without compromising viability," *Plant J*, vol. 31, (3), pp. 365-374, 2002.
- [64] T. Juhasz *et al*, "Dynamics of shock waves and cavitation bubbles generated by picosecond laser pulses in corneal tissue and water," *Lasers Surg Med*, vol. 15, (1), pp. 91-98, 1994.
- [65] A. Vogel *et al*, "Mechanisms of intraocular photodisruption with picosecond and nanosecond laser pulses," *Lasers Surg Med*, vol. 15, (1), pp. 32-43, 1994.
- [66] B. M. Kim *et al*, "Influence of pulse duration on ultrashort laser pulse ablation of biological tissues," *J Biomed Opt*, vol. 6, (3), pp. 332-338, 2001.
- [67] J. Neev *et al*, "Ultrashort pulse lasers for hard tissue ablation," *IEEE Journal of Selected Topics in Quantum Electronics*, vol. 2, (4), pp. 790-800, 1996.
- [68] M. Hashida *et al*, "Non-thermal ablation of expanded polytetrafluoroethylene with an intense femtosecond-pulse laser," *Optics Express*, vol. 17, (15), pp. 13116, 2009.

- [69] C. Kalupka, J. Finger and M. Reininghaus, "Time-resolved investigations of the non-thermal ablation process of graphite induced by femtosecond laser pulses," *Journal of Applied Physics*, vol. 119, (15), pp. 153105, 2016.
- [70] F. H. Loesel *et al*, "Non-thermal ablation of neural tissue with femtosecond laser pulses," *Appl Phys B*, vol. 66, (1), pp. 121-128, 1998.
- [71] H. Maeda *et al*, "Vascular permeability enhancement in solid tumor: various factors, mechanisms involved and its implications," *Int. Immunopharmacol.*, vol. 3, (3), pp. 319-328, 2003.
- [72] D. P. Wan, J. Wang and P. Mathew, "Energy Deposition and Non-Thermal Ablation in Femtosecond Laser Grooving of Silicon," *Machining Science and Technology*, vol. 15, (3), pp. 263-283, 2011.
- [73] D. W. Bäuerle, *Laser Processing and Chemistry*. (4th ed.) 2011.
- [74] C. Schaffer *et al*, "Dynamics of femtosecond laser-induced breakdown in water from femtoseconds to microseconds," *Opt Express*, vol. 10, (3), pp. 196-203, 2002.
- [75] V. Venugopalan *et al*, "Role of laser-induced plasma formation in pulsed cellular microsurgery and micromanipulation," *Phys. Rev. Lett.*, vol. 88, (7), pp. 078103, 2002.
- [76] W. T. Silfvast, *Laser Fundamentals*. (2nd ed.) 2012
- [77] R. Boyd, *Nonlinear Optics*. Academic Press, 2008.
- [78] C. L. Arnold *et al*, "Computational model for nonlinear plasma formation in high NA micromachining of transparent materials and biological cells," *Optics Express*, vol. 15, (16), pp. 10303, 2007.
- [79] D. N. Vitek *et al*, "Temporally focused femtosecond laser pulses for low numerical aperture micromachining through optically transparent materials," *Opt. Express, OE*, vol. 18, (17), pp. 18086-18094, 2010.
- [80] Jerome Lapointe and Raman Kashyap, "A simple technique to overcome self-focusing, filamentation, supercontinuum generation, aberrations, depth dependence and waveguide interface roughness using fs laser processing," *Scientific Reports (Nature Publisher Group)*, vol. 7, pp. 1-13, 2017.
- [81] G. M. Cooper, *The Cell*. (2nd ed.) 2000.
- [82] D. Ribatti, "An historical note on the cell theory," *Exp. Cell Res.*, vol. 364, (1), pp. 1-4, 2018.

- [83] T. Schwann, *Mikroskopische Untersuchungen Uber Die Ubereinstimmung in Der Struktur Und Dem Wachsten Der Thiere Und Pflanzen*. Berlin: Saunderschen Buchhandlung, 1839.
- [84] B. M. Ogle, J. L. Platt and M. Cascalho, "Biological implications of cell fusion," *Nature Reviews Molecular Cell Biology*, vol. 6, (7), pp. 567-575, 2005.
- [85] H. Harris and J. F. Watkins, "Hybrid Cells Derived from Mouse and Man : Artificial Heterokaryons of Mammalian Cells from Different Species," *Nature*, vol. 205, (4972), pp. 640, 1965.
- [86] X. Wang *et al*, "Cell fusion is the principal source of bone-marrow-derived hepatocytes," *Nature*, vol. 422, (6934), pp. 897-901, 2003.
- [87] G. Barski, S. Sorieul and F. Cornefert, "Production dans des cultures in vitro de deux souches cellulaires en association de cellules de caratere hybride," *C. R. Hebd. Seances Acad. Des Sci.*, vol. 251, pp. 1825–1827, 1960.
- [88] S. Martens and H. T. McMahon, "Mechanisms of membrane fusion: disparate players and common principles," *Nature Reviews Molecular Cell Biology*, vol. 9, (7), pp. 543, 2008.
- [89] G. Vassilopoulos, P. Wang and D. W. Russell, "Transplanted bone marrow regenerates liver by cell fusion," *Nature*, vol. 422, (6934), pp. 901-904, 2003.
- [90] A. J. Gibson *et al*, "Dermal fibroblasts convert to a myogenic lineage in mdx mouse muscle," *J. Cell. Sci.*, vol. 108 (Pt 1), pp. 207-214, 1995.
- [91] J. Rosenblatt *et al*, "Vaccination with dendritic cell/tumor fusion cells results in cellular and humoral antitumor immune responses in patients with multiple myeloma," *Blood*, vol. 117, (2), pp. 393-402, 2011.
- [92] B. Vasir *et al*, "Fusion of dendritic cells with multiple myeloma cells results in maturation and enhanced antigen presentation," *Br. J. Haematol.*, vol. 129, (5), pp. 687-700, 2005.
- [93] L. Minai *et al*, "Optical nanomanipulations of malignant cells: controlled cell damage and fusion," *Small*, vol. 8, (11), pp. 1732-1739, 2012.
- [94] A. Bahadori *et al*, "Controlled cellular fusion using optically trapped plasmonic nano-heaters," in 2016/09/16.
- [95] R. Dimova *et al*, "Vesicles in electric fields: Some novel aspects of membrane behavior," *Soft Matter*, vol. 5, (17), pp. 3201-3212, 2009.
- [96] M. Wernig *et al*, "In vitro reprogramming of fibroblasts into a pluripotent ES-cell-like state," *Nature*, vol. 448, (7151), pp. 318-324, 2007.

- [97] Akira C Saito *et al*, "Introducing Micrometer-Sized Artificial Objects into Live Cells: A Method for Cell–Giant Unilamellar Vesicle Electrofusion," *PLoS One*, vol. 9, (9), pp. e106853, 2014.
- [98] J. Gong *et al*, "Femtosecond laser-induced cell fusion," *Appl. Phys. Lett.*, vol. 92, (9), pp. 093901, 2008.
- [99] S. Chen *et al*, "Laser-induced fusion of human embryonic stem cells with optical tweezers," *Appl. Phys. Lett.*, vol. 103, (3), pp. 033701, 2013.
- [100] A. Bahadori, L. B. Oddershede and P. M. Bendix, "Hot-nanoparticle-mediated fusion of selected cells," *Nano Res.*, vol. 10, (6), pp. 2034-2045, 2017.
- [101] L. V. Chernomordik and M. M. Kozlov, "Membrane Hemifusion: Crossing a Chasm in Two Leaps," *Cell*, vol. 123, (3), pp. 375-382, 2005.
- [102] D. Kweon, B. Kong and Y. Shin, "Hemifusion in Synaptic Vesicle Cycle," *Front. Mol. Neurosci.*, vol. 10, 2017.
- [103] Yinling Li *et al*, "Membrane Structures of the Hemifusion-Inducing Fusion Peptide Mutant G1S and the Fusion-Blocking Mutant G1V of Influenza Virus Hemagglutinin Suggest a Mechanism for Pore Opening in Membrane Fusion," *Journal of Virology*, vol. 79, (18), pp. 12065-12076, 2005.
- [104] D. W. Lee *et al*, "Real-time intermembrane force measurements and imaging of lipid domain morphology during hemifusion," *Nature Communications*, vol. 6, pp. 7238, 2015.
- [105] D. Purves, G. J. Augustine and D. Fitzpatrick, *Neuroscience. 2nd Edition. the Retina.* (2nd ed.) Sunderland (MA): Sinauer Associates, 2001.
- [106] M. J. Ali, S. G. Honavar and V. A. Reddy, "Distant metastatic retinoblastoma without central nervous system involvement," *Indian J. Ophthalmol.*, vol. 61, (7), pp. 357-359, July 01, 2013.
- [107] V. Khetan, A. Gupta and L. Gopal, "Retinoblastoma: Recent trends A mini review based on published literature," *Oman J. Ophthalmol.*, vol. 4, (3), pp. 108-115, September 01, 2011.
- [108] A. N. Pandey, "Retinoblastoma: An overview," *Saudi Journal of Ophthalmology*, vol. 28, (4), pp. 310-315, 2014.
- [109] V. S. Donnerberg and A. D. Donnerberg, "Multiple drug resistance in cancer revisited: the cancer stem cell hypothesis," *J. Clin. Pharmacol.*, vol. 45, (8), pp. 872-877, August 01, 2005.
- [110] M. Alamgeer *et al*, "Cancer stem cells in lung cancer: Evidence and controversies," *Respirology*, vol. 18, (5), pp. 757-764, July 01, 2013.

- [111] M. Al-Hajj *et al*, "Prospective identification of tumorigenic breast cancer cells," *Proc. Natl. Acad. Sci. U. S. A.*, vol. 100, (7), pp. 3983-3988, April 01, 2003.
- [112] F. Moltzahn and G. N. Thalmann, "Cancer stem cells in prostate cancer," *Translational Andrology and Urology*, vol. 2, (3), pp. 242-253, 2013.
- [113] O. H. Yilmaz *et al*, "Pten dependence distinguishes haematopoietic stem cells from leukaemia-initiating cells," *Nature*, vol. 441, (7092), pp. 475-482, May 25, 2006.
- [114] B. J. P. Huntly and D. G. Gilliland, "Leukaemia stem cells and the evolution of cancer-stem-cell research," *Nat Rev Cancer*, vol. 5, (4), pp. 311-321, 2005.
- [115] A. L. Vescovi, R. Galli and B. A. Reynolds, "Brain tumour stem cells," *Nat Rev Cancer*, vol. 6, (6), pp. 425-436, 2006.
- [116] E. Schmelzer *et al*, "Human hepatic stem cells from fetal and postnatal donors," *J. Exp. Med.*, vol. 204, (8), pp. 1973-1987, August 06, 2007.
- [117] M. Tanaka *et al*, "Mouse hepatoblasts at distinct developmental stages are characterized by expression of EpCAM and DLK1: drastic change of EpCAM expression during liver development," *Mech. Dev.*, vol. 126, (8-9), pp. 665-676, September 01, 2009.
- [118] S. Krishnakumar *et al*, "EpCAM expression in retinoblastoma: a novel molecular target for therapy," *Invest. Ophthalmol. Vis. Sci.*, vol. 45, (12), pp. 4247-4250, December 01, 2004.
- [119] M. Mitra *et al*, "EpCAM is a putative stem marker in retinoblastoma and an effective target for T-cell-mediated immunotherapy," *Mol. Vis.*, vol. 18, pp. 290-308, 2012.
- [120] L. Minai *et al*, "Experimental Proof for the Role of Nonlinear Photoionization in Plasmonic Phototherapy," *Nano Lett.*, vol. 16, (7), pp. 4601-4607, 2016.
- [121] L. Minai, D. Yeheskely-Hayon and D. Yelin, "High levels of reactive oxygen species in gold nanoparticle-targeted cancer cells following femtosecond pulse irradiation," vol. 3, pp. 2146, 2013.
- [122] E. Boulais, R. Lachaine and M. Meunier, "Plasma mediated off-resonance plasmonic enhanced ultrafast laser-induced nanocavitation," *Nano Lett.*, vol. 12, (9), pp. 4763-4769, September 12, 2012.
- [123] T. W. Reid *et al*, "Characteristics of an Established Cell Line of Retinoblastoma," *J Natl Cancer Inst*, vol. 53, (2), pp. 347-360, 1974.
- [124] F. Schulz *et al*, *Nanoscale*. 20148(13).

- [125] S. I. Jenkins *et al*, "'Stealth' nanoparticles evade neural immune cells but also evade major brain cell populations: Implications for PEG-based neurotherapeutics," *J. Control. Release*, vol. 224, pp. 136-145, February 28, 2016.
- [126] J. V. Jokerst *et al*, "Nanoparticle PEGylation for imaging and therapy," *Nanomedicine (Lond)*, vol. 6, (4), pp. 715-728, June 01, 2011.
- [127] M. Takeichi, "Cadherins: a molecular family important in selective cell-cell adhesion," *Annu. Rev. Biochem.*, vol. 59, pp. 237-252, 1990.
- [128] B. J. Pfister *et al*, "Biomedical engineering strategies for peripheral nerve repair: surgical applications, state of the art, and future challenges," *Crit Rev Biomed Eng*, vol. 39, (2), pp. 81-124, 2011.
- [129] Wolf-de Jonge, I C D Y M, J. F. Beek and R. Balm, "25 years of laser assisted vascular anastomosis (LAVA): what have we learned?" *Eur J Vasc Endovasc Surg*, vol. 27, (5), pp. 466-476, 2004.
- [130] L. H. Yap, J. Constantinides and C. E. Butler, "Venous thrombosis in coupled versus sutured microvascular anastomoses," *Ann Plast Surg*, vol. 57, (6), pp. 666-669, 2006.
- [131] P. E. Sokolove and D. K. Barnes, "Extensor and flexor tendon injuries in the hand, wrist, and foot," in *Roberts and Hedges' Clinical Procedures in Emergency Medicine and Acute Care*, Seventh Edition ed. 2019.
- [132] L. Chu and D. K. Robinson, "Industrial choices for protein production by large-scale cell culture," *Curr. Opin. Biotechnol.*, vol. 12, (2), pp. 180-187, 2001.
- [133] N. Petrovsky and P. D. Cooper, "Carbohydrate-based immune adjuvants," *Expert Rev Vaccines*, vol. 10, (4), pp. 523-537, 2011.
- [134] B. Alberts *et al*, "Isolating Cells and Growing Them in Culture," 2002.
- [135] A. Varki *et al*, "Glycosylation changes in cancer," in *Essentials of Glycobiology*, 3rd ed., A. Varki *et al*, Ed. 2015.
- [136] R. Leth-Larsen, R. R. Lund and H. J. Ditzel, "Plasma membrane proteomics and its application in clinical cancer biomarker discovery," *Mol. Cell Proteomics*, vol. 9, (7), pp. 1369-1382, 2010.
- [137] U. K. Tirlapur *et al*, "Femtosecond near-infrared laser pulses elicit generation of reactive oxygen species in mammalian cells leading to apoptosis-like death," *Exp. Cell Res.*, vol. 263, (1), pp. 88-97, 2001.
- [138] D. J. Stevenson *et al*, "Single cell optical transfection," *J R Soc Interface*, vol. 7, (47), pp. 863-871, 2010.

- [139] M. Waleed *et al*, "Single-cell optoporation and transfection using femtosecond laser and optical tweezers," *Biomed Opt Express*, vol. 4, (9), pp. 1533-1547, 2013.
- [140] H. He *et al*, "All-optical human cell fusion by a fiber femtosecond laser," *Appl. Phys. Lett.*, vol. 93, (16), pp. 163901, 2008.
- [141] R. W. Steubing *et al*, "Laser induced cell fusion in combination with optical tweezers: the laser cell fusion trap," *Cytometry*, vol. 12, (6), pp. 505-510, 1991.
- [142] R. Wiegand *et al*, "Laser-induced fusion of mammalian cells and plant protoplasts," *J. Cell. Sci.*, vol. 88 (Pt 2), pp. 145-149, 1987.
- [143] G. Michel *et al*, "The cell wall polysaccharide metabolism of the brown alga *Ectocarpus siliculosus*. Insights into the evolution of extracellular matrix polysaccharides in Eukaryotes," *New Phytol.*, vol. 188, (1), pp. 82-97, 2010.
- [144] M. V. L. Bennett and R. S. Zukin, "Electrical Coupling and Neuronal Synchronization in the Mammalian Brain," *Neuron*, vol. 41, (4), pp. 495-511, 2004.
- [145] S. G. Hormuzdi *et al*, "Electrical synapses: a dynamic signaling system that shapes the activity of neuronal networks," *Biochim. Biophys. Acta*, vol. 1662, (1-2), pp. 113-137, 2004.
- [146] R. S. Nowakowski, "Stable neuron numbers from cradle to grave," *Proc. Natl. Acad. Sci. U. S. A.*, vol. 103, (33), pp. 12219-12220, 2006
- [147] J. R. Sanes and M. Yamagata, "Many paths to synaptic specificity," *Annu. Rev. Cell Dev. Biol.*, vol. 25, pp. 161-195, 2009.
- [148] M. P. Coleman and M. R. Freeman, "Wallerian degeneration, wld(s), and nmnat," *Annu. Rev. Neurosci.*, vol. 33, pp. 245-267, 2010.
- [149] L. R. Robinson, "Traumatic injury to peripheral nerves," *Muscle Nerve*, vol. 23, (6), pp. 863-873, 2000.
- [150] P. D. Donofrio and J. W. Albers, "AAEM minimonograph #34: polyneuropathy: classification by nerve conduction studies and electromyography," *Muscle Nerve*, vol. 13, (10), pp. 889-903, 1990.
- [151] J. D. England and A. K. Asbury, "Peripheral neuropathy," *The Lancet*, vol. 363, (9427), pp. 2151-2161, 2004.
- [152] J. T. Wang and B. A. Barres, "Axon Degeneration: Where the Wlds Things Are," *Curr Biol*, vol. 22, (7), pp. R223, 2012.
- [153] J. T. Wang, Z. A. Medress and B. A. Barres, "Axon degeneration: molecular mechanisms of a self-destruction pathway," *J. Cell Biol.*, vol. 196, (1), pp. 7-18, 2012.

- [154] E. S. Rosenzweig and J. W. McDonald, "Rodent models for treatment of spinal cord injury: research trends and progress toward useful repair," *Curr. Opin. Neurol.*, vol. 17, (2), pp. 121-131, 2004.
- [155] B. H. Dobkin and L. A. Havton, "Basic advances and new avenues in therapy of spinal cord injury," *Annu. Rev. Med.*, vol. 55, pp. 255-282, 2004.
- [156] Y. Kim *et al*, "Neuro-optical microfluidic platform to study injury and regeneration of single axons," *Lab Chip*, vol. 9, (17), pp. 2576-2581, 2009.
- [157] M. W. McBurney and B. J. Rogers, "Isolation of male embryonal carcinoma cells and their chromosome replication patterns," *Dev. Biol.*, vol. 89, (2), pp. 503-508, 1982.
- [158] E. M. Jones-Villeneuve *et al*, "Retinoic acid-induced neural differentiation of embryonal carcinoma cells," *Mol. Cell. Biol.*, vol. 3, (12), pp. 2271-2279, 1983.
- [159] V. Kohli and A. Y. Elezzabi, "Laser surgery of zebrafish (*Danio rerio*) embryos using femtosecond laser pulses: optimal parameters for exogenous material delivery, and the laser's effect on short- and long-term development," *BMC Biotechnology*, vol. 8, (1), pp. 7, 2008.
- [160] V. Kohli *et al*, "An alternative method for delivering exogenous material into developing zebrafish embryos," *Biotechnol. Bioeng.*, vol. 98, (6), pp. 1230-1241, 2007.
- [161] R. Gonzalez-Gonzalez *et al*, "Papillary thyroid carcinoma: differential diagnosis and prognostic values of its different variants: review of the literature," *ISRN Oncology*, vol. 2011, pp. 915925, 2011.
- [162] N. Al-Brahim and S. L. Asa, "Papillary thyroid carcinoma: an overview," *Arch. Pathol. Lab. Med.*, vol. 130, (7), pp. 1057-1062, 2006.
- [163] E. P. Furlani, I. H. Karampelas and Q. Xie, "Analysis of pulsed laser plasmon-assisted photothermal heating and bubble generation at the nanoscale," *Lab on a Chip*, vol. 12, (19), pp. 3707-3719, 2012.
- [164] P. B. Johnson and R. W. Christy, "Optical Constants of the Noble Metals," *Phys. Rev. B*, vol. 6, (12), pp. 4370-4379, 1972.
- [165] L. Guo *et al*, "Heat Transfer Across Metal-Dielectric Interfaces During Ultrafast-Laser Heating," *J. Heat Transfer*, vol. 134, (4), pp. 5, 2012.
- [166] S. Hashimoto, D. Werner and T. Uwada, "Studies on the interaction of pulsed lasers with plasmonic gold nanoparticles toward light manipulation, heat management, and nanofabrication," *Journal of Photochemistry and Photobiology C: Photochemistry Reviews*, vol. 13, (1), pp. 28-54, 2012.

[167] L. Xu *et al*, "Programmable chirp compensation for 6-fs pulse generation with a prism-pair-formed pulse shaper," *IEEE Journal of Quantum Electronics*, vol. 36, (8), pp. 893-899, 2000.

[168] W. R. Zipfel, R. M. Williams and W. W. Webb, "Nonlinear magic: multiphoton microscopy in the biosciences," *Nat. Biotechnol.*, vol. 21, (11), pp. 1369-1377, 2003.

Appendix A⁷

⁷Portions of this chapter have been published in: Katchinskiy *et al.* Anti-EpCAM Gold Nanorods and Femtosecond Laser Pulses for Targeted Lysis of Retinoblastoma. *Advanced Therapeutics*, 1(1): 1-10, **2018**.
The following calculations were performed by Dr. Ali Hatf, Nipissing Computational Physics Laboratory

A.1 Calculation of Electric Field Enhancement Around Au-NR

To simulate the photothermal response of Au-NR to femtosecond laser irradiation, finite element method (FEM) using commercial software (COMSOL Multiphysics 5.2) was performed. The modeled system consists of 11 nm × 43 nm Au-NR immersed in water. 55 fs laser pulse at a wavelength of $\lambda = 800$ nm with Gaussian spatial profile is coupled to Au-NR. The interaction of the Au-NR with the femtosecond laser pulse is analyzed at three electric field polarization states (transverse, longitudinal, and diagonal). The time-dependent distribution of the electromagnetic field and the thermal response of the Au-NR are modeled by a system of partial differential equations (PDE) as shown below.

Electromagnetic Field Distribution: For a time-harmonic electric field oscillating at a frequency ω , the electric field distribution $\vec{E}(r,t)$ is computed using the Helmholtz equation [163]:

$$\nabla \times (\mu_r^{-1} \nabla \times \vec{E}) - k_0^2 (\epsilon_r - j \frac{\sigma}{\omega \epsilon_0}) \vec{E} = 0 \quad (\text{A.1})$$

where k_0 is the wavenumber of the incident laser pulse radiation, σ , ϵ_r and μ_r are the electrical conductivity, relative permittivity and permeability of the material, respectively. The parameters are listed in table A.1.

Table A.1: Material electromagnetic parameters

Parameter	Symbol	Value
Au relative permittivity	$\epsilon_{r,Au}(\lambda)$	Interpolated from Johnson & Christy [164]
Au electrical conductivity	$\sigma_{Au}(\lambda)$	Interpolated from Johnson & Christy [164] S m ⁻¹
Au relative permeability	$\mu_{r,Au}$	1
Water relative permittivity	$\epsilon_{r,w}$	1.764
Water electrical conductivity	σ_w	0 S m ⁻¹
Water relative permeability	$\mu_{r,w}$	1

A.2 Calculation of Temperature around Au-NR

Thermal evolution: The time-domain intensity of the femtosecond pulse lasers is given by:

$$I(t) = \frac{F_L}{\sqrt{2\pi\tau_\sigma}} \exp\left(-\frac{[t - t_0]^2}{2\tau_\sigma^2}\right) \quad (\text{A.2})$$

where, $\tau_\sigma = \tau_l/2\sqrt{2\ln 2}$ is the pulse width, where τ_l is the laser pulse width defined as the full width at half maximum of the Gaussian temporal profile, t_0 is the position of the center of the peak, and F_L is the incident laser energy density (fluence). To study femtosecond laser pulse and Au-NR interaction mechanisms, we consider the case where τ_l is much less than the characteristic time constants of the transient non-equilibrium photothermal effects (i.e. electron–lattice interactions and phonon–phonon interactions at the surface of the particle). Since the heat conduction of the lattice is slower compared to that of the electrons, a two-temperature model (TTM) can be used such that the electrons and lattice are at different temperatures (T_e and T_l). Since the laser fluence is well below the optical breakdown of water, direct absorption by the

water molecules is neglected; as such a single temperature heat diffusion equation applies to the heat transport model. However, because of the phonon mismatch factor, discontinuity between the water and the Au-NR temperatures appears at the interface; therefore, we solve the following set of time-dependent temperature equations for water and the electrons and the lattice for Au-NR [165,166]:

$$C_e(r) \frac{\partial T_e(r, t)}{\partial t} = \nabla \cdot (k_e \nabla T_e(r, t)) - G[T_e(r, t) - T_l(r, t)] + S(t) \quad (\text{A.3a})$$

$$C_l(r) \frac{\partial T_l(r, t)}{\partial t} = \nabla \cdot (k_l \nabla T_l(r, t)) + G[T_e(r, t) - T_l(r, t)] - F(r, T_l, T_w) \quad (\text{A.3b})$$

$$\rho_w(r) c_w(r) \frac{\partial T_w(r, t)}{\partial t} = \nabla \cdot (k_w \nabla T_w(r, t)) + F(r, T_l, T_w) \quad (\text{A.3c})$$

where, T_e , T_l and T_w are the time-dependent temperatures of the electrons, lattice and surrounding medium (water), respectively. C is the volumetric specific heat (C_e (electronic) and C_l (lattice)) and C_w is the water specific heat capacity and k is the thermal conductivity. The second term on the right-hand side in (A.3a) and (A.3b) describes the energy exchange from the electrons to the lattice via electron-phonon coupling via a coefficient of thermal conductance, G . The thermal conductance (G) relates the temperature drop at an interface to the heat flux crossing the interface and constitutes the coupling parameter between a particle and surrounding medium energy equations. The term $S(t)$ in Eqn. A.3a describes the absorbed laser energy. Notably, the F term in Eqns. A.3b and A.3c describes the heat transfer across the interface between the AuNR and surrounding which is defined as [161]:

$$F(r, T_l, T_w) = \frac{h A_{NR}}{V_{NR}} [T_l(r, t) - T_w(r, t)] \quad (\text{A.4})$$

where, h is the interfacial thermal conductance and is the fitting parameter for the cooling process of AuNR in aqueous solutions. The V_{NR} (nm^3) and A_{NR} (nm^2) are the AuNR volume and surface area, respectively. The parameters are listed in table A.2.

Table A.2: Material thermal and physical parameters

Parameter	Symbol	Value
Electron volumetric specific heats	C_e	$70 (\text{Jm}^{-3}\text{K}^{-2}) T_e$
Lattice volumetric specific heats	C_l	$3 \times 10^6 \text{ Jm}^{-3}\text{K}^{-1}$
Water specific heat capacity	c_w	$4182 \text{ J kg}^{-1} \text{ K}^{-1}$
Au thermal conductivity	k_{Au}	$300 \text{ W m}^{-1} \text{ K}^{-1}$
Electron thermal conductivity	k_e	k_{Au}
Lattice thermal conductivity	k_e	$0.001 k_{Au}$
Water thermal conductivity	k_w	$0.6 \text{ W m}^{-1} \text{ K}^{-1}$
Water density	ρ_w	1000 kg m^{-3}
Interfacial thermal conductance	h	$105 \times 10^6 \text{ Wm}^{-2}\text{K}^{-1}$
Thermal conductance	G	$4.6 \times 10^{16} \text{ W/m}^3\text{K}$
AuNR area	A_{NR}	1486 nm^2
AuNR volume	V_{NR}	3738 nm^3

Appendix B

B.1 Pulse Width Estimation Due to Dispersion

The laser pulses used for the studies in Chapter 3 are 35 femtoseconds at a center wavelength of ~ 800 nm with a pulse repetition rate of ~ 1 KHz. Assuming a 35 femtosecond laser pulse, the pulse broadening due to optical elements placed in the beam path can be estimated. The primary source of pulse broadening is the $4\times$ microscope objective, which is made of BK7 glass, and the total glass thickness in the objective tube is estimated to be around 1.25 mm. Based on the thickness of the glass, broadened pulse duration can be estimated. The group delay dispersion (GDD) of BK7 glass is estimated to be $465 \text{ fs}^2/\text{cm}$ [167]. Therefore, the total group velocity dispersion (GVD) of 1.25cm glass is 465 fs^2 .

Using equation (B.1), the broadened pulse duration can be estimated as [168]

$$\tau_{out} = \tau_{in} \left[1 + 7.68 \left(\frac{D}{\tau_{in}^2} \right) \right]^{1/2} \quad (\text{B.1})$$

where D , τ_{out} and τ_{in} represent the GVD coefficient, output pulse duration and the input pulse duration, respectively. With an input pulse duration of 35 femtoseconds and the GVD coefficient of 579 fs^2 , the pulse duration after the microscope objective is estimated to be 55 femtoseconds.

Appendix C

This thesis is an original work by Nir Katchinskiy, who conducted the research under the supervision of Professor A. Y. Elezzabi at the University of Alberta. The experimentations of applying femtosecond laser pulses, were taken place in professor Elezzabi's lab, by Nir Katchinskiy.

This work is multidisciplinary in its nature and combines topics from engineering, physics, biology and oncology; therefore, a collaborative work with Professor. Roseline Godbout from the department of oncology was established. Professor Roseline Godbout graciously provided Nir Katchinskiy full access to her lab at the Cross Cancer Institute. All cell samples were housed at the Cross Cancer Institute. Nir Katchinskiy obtained the cellular cultures, performed all cellular preparation work before performing the experiments.

Breast cancer and human colon carcinoma cancer cells were obtained from the laboratory of professor Frank Wuest. Professor Wuest also graciously provided guidance

Once experiments were completed, the cells were brought back to the Cross Cancer Institute, where Nir performed cellular preparation for imaging and analysis. Nir performed all cell imaging and analysis as well. 2-photon microscopy, fluorescence microscopy, HCS imaging, confocal imaging at the Cross Cancer imaging facility. TEM imaging were performed by Pinzhang Gao. SEM sample preparation was performed by Nir at the ECE nanofab facility, and SEM imaging was performed by Dr. Li Peng.